Dissertation
submitted to the
Combined Faculty of Mathematics, Engineering and Natural Sciences
of Heidelberg University, Germany
for the degree of
Doctor of Natural Sciences

Put forward by
Jing, Li 李婧
born in: Xinjiang
Oral examination: 2025/11/27

IDENTIFYING SUPERNOVA REMNANTS IN NEARBY STAR-FORMING GALAXIES AND INVESTIGATING THEIR PREFERRED METALLICITY ENVIRONMENTS

Referees: Dr. Kathryn Kreckel
Dr. Eva Grebel

Once I thought that completing a thesis only required knowledge —
but in the end, I realized it also demands immeasurable love and support.

To everyone who walked beside me, thank you —
for your presence, your kindness, and your belief in me.

ABSTRACT

Supernova remnants (SNRs) are key components in the energy and chemical feedback processes that shape galaxy evolution. However, their localized impact on the surrounding interstellar medium (ISM) remains uncertain. In this thesis, we present the largest extragalactic SNR catalog to date, identifying approximately 2,200 SNR candidates across 19 nearby star-forming galaxies. Our work is based on optical integral field spectroscopy from the PHANGS–MUSE survey, obtained with the MUSE instrument on the Very Large Telescope. Unlike traditional photometric surveys, our data provide spatially resolved spectroscopic diagnostics, allowing us to robustly distinguish SNRs from H II regions using multiple criteria, including [S II]/Hα and [O I]/Hα line ratios, velocity dispersion, and Baldwin–Phillips–Terlevich (BPT) diagrams.

To assess the role of SNRs in chemical enrichment and environmental dependence, we examine gas-phase oxygen abundances in H II regions at varying distances from SNRs. We find no statistically significant metallicity enhancement in their vicinity, suggesting that SNRs show no strong preference for metallicity environment.

Finally, we present exploratory analyses that combine PHANGS–MUSE SNR catalogs with ALMA, JWST, and HST data to investigate their relation to molecular clouds, their potential impact on dust and PAHs, and their small-scale structural and environmental properties.

ZUSAMMENFASSUNG

Supernova-Überreste (SNRs) sind zentrale Komponenten der Energie- und chemischen Rückkopplungsprozesse, die die Entwicklung von Galaxien prägen. Ihr lokaler Einfluss auf das umgebende interstellare Medium (ISM) ist jedoch nach wie vor unklar. In dieser Dissertation präsentieren wir den bislang größten extragalaktischen SNR-Katalog und identifizieren etwa 2.200 SNR-Kandidaten in 19 nahen, sternbildenden Galaxien. Unsere Arbeit basiert auf optischer Integral-Feld-Spektroskopie aus dem PHANGS–MUSE-Survey, aufgenommen mit dem MUSE-Instrument am Very Large Telescope. Im Gegensatz zu traditionellen photometrischen Surveys liefern unsere Daten räumlich aufgelöste spektroskopische Diagnostika und ermöglichen es uns, SNRs anhand mehrerer Kriterien zuverlässig von H II-Regionen zu unterscheiden, darunter die Linienverhältnisse [S II]/Hα und [O I]/Hα, die Geschwindigkeitsdispersion sowie Baldwin–Phillips–Terlevich-(BPT)-Diagramme.

Um die Rolle von SNRs bei der chemischen Anreicherung und ihre Abhängigkeit von Umweltparametern zu untersuchen, analysieren wir den Sauerstoffgehalt in der

Gasphase von H II-Regionen in unterschiedlichen Abständen zu SNRs. Wir finden in ihrer Umgebung keine statistisch signifikante Anreicherung an Metallen, was darauf hinweist, dass SNRs kein ausgeprägtes Präferenzmuster in Bezug auf metallizitätsreiche Umgebungen zeigen.

Abschließend präsentieren wir explorative Analysen, die PHANGS–MUSE-SNR-Kataloge mit ALMA-, JWST- und HST-Daten kombinieren, um ihre Beziehung zu Molekülwolken, ihren möglichen Einfluss auf Staub und PAHs sowie ihre kleinskaligen strukturellen und umweltbedingten Eigenschaften zu untersuchen.

PUBLICATIONS

First-author and co-authored papers.

1. *Li, Jing* et al., 2025, A&A, in preparation,
   Investigating the Sub-kpc Metallicity Environment of SNRs in Nearby High-mass Star-forming Galaxies
2. *Li, Jing* et al., 2024, A&A, 690, A161,
   Discovery of ~2200 new supernova remnants in 19 nearby star-forming galaxies with MUSE spectroscopy
3. Egorov, Oleg et al. (inc. *Li, Jing*), 2025, A&A , accepted,
   Polycyclic aromatic hydrocarbons destruction in star-forming regions across 42 nearby galaxies
4. Barnes, A. T. et al. (inc. *Li, Jing*), 2025, A&A, accepted,
   The PHANGS-MUSE/HST-Hα Nebulae Catalogue
5. Sarbadhicary, S. K. et al. (inc. *Li, Jing*), 2025, arXiV, SDSS-V LVM: Collisionless Shocks in the Supernova Rem- nant RCW86
6. Pathak, D. et al. (inc. *Li, Jing*), 2025, ApJ, 982, 140,
   Linking Stellar Populations to H II *Regions across Nearby Galaxies. II. Infrared Reprocessed and UV Direct Radiation Pressure in* H II *Regions*
7. Solimano, M. et al. (inc. *Li, Jing*), 2025, A&A, 693, A70,
   A hidden active galactic nucleus powering bright [O III] *nebulae in a protocluster at $z = 4.5$ revealed by JWST*
8. Drory, N. et al. (inc. *Li, Jing*), 2024, AJ, 168, 198,
   The SDSS-V Local Volume Mapper (LVM): Scientific Motivation and Project Overview
9. Kreckel, K. et al. (inc. *Li, Jing*), 2024, A&A, 689, A352,
   SDSS-V Local Volume Mapper (LVM): A glimpse into Orion
10. Williams, T. G. et al. (inc. *Li, Jing*), 2024, ApJS, 273, 13,
    PHANGS-JWST: Data-processing Pipeline and First Full Public Data Release
11. Mayker Chen, N. et al. (inc. *Li, Jing*), 2024, AJ, 168, 5,
    Hα Emission and H II *Regions at the Locations of Recent Supernovae in Nearby Galaxies*

12. Watkins, E. J. et al. (inc. *Li, Jing*), 2023, A&A, 676, A67,
Quantifying the energetics of molecular superbubbles in PHANGS galaxies

13. Barnes, A. T. et al. (inc. *Li, Jing*), 2023, ApJ, 944, L22,
PHANGS–JWST First Results: Multiwavelength View of Feedback-driven Bubbles (the Phantom Voids) across NGC 628

14. Lee, J. C. et al. (inc. *Li, Jing*), 2023, ApJ, 944, L17,
The PHANGS–JWST Treasury Survey: Star Formation, Feedback, and Dust Physics at High Angular Resolution in Nearby GalaxieS

CONTENTS

I LITERATURE 1

1 INTRODUCTION 3

1.1 Galaxies & Interstellar Medium 3
1.2 Supernova Physics 4
  1.2.1 Supernova Types 5
  1.2.2 Supernova Feedback 6
  1.2.3 Supernova Environment 7
1.3 Supernova Remnants Physics 7
  1.3.1 Supernova Remnants Evolution 8
  1.3.2 Supernova Remnants Observables 9
  1.3.3 Supernova Remnants Populations 10
1.4 Open Questions 11

II MAIN 15

2 DISCOVERY OF ~2200 NEW SUPERNOVA REMNANTS IN 19 NEARBY STAR-FORMING GALAXIES WITH MUSE SPECTROSCOPY 17

2.1 Introduction 18
2.2 Data 23
2.3 Methods 24
  2.3.1 Parent sample identification 24
  2.3.2 Parent sample classification 34
  2.3.3 Validation of methods: Comparison with supernova remnants in M83 43
2.4 Results 44
  2.4.1 Comparison with H II regions 44
  2.4.2 Comparison with the literature: Supernova remnants in other galaxies 46
2.5 Discussion 47
  2.5.1 Expected number of supernova remnants and inferred supernova frequencies 47
  2.5.2 Lessons learned when identifying supernova remnants with integral field units 49
  2.5.3 Classification of the candidate sample and blending with HII regions 50
  2.5.4 Characterizing the shocked regions 51
2.6 Conclusions 52

3 INVESTIGATING THE SUB-KPC METALLICITY ENVIRONMENT OF SNRS IN NEARBY HIGH-MASS STAR-FORMING GALAXIES 65
  3.1 Introduction 66
  3.2 Data and Methods 67
    3.2.1 SNR Catalog 68
    3.2.2 Measuring ISM Metallicity 68
    3.2.3 Galaxy Star Formation Rate Maps 70
  3.3 Results 70
  3.4 Discussion 74
  3.5 Conclusions 75
4 EXPLORATORY WORKS 77
  4.1 SNR Placement with Respect to Molecular Clouds/Molecular Gas 77
  4.2 Constraining Dust Properties at SNR Sites 79
  4.3 HST Imaging of Supernova Remnants 80
    4.3.1 SNR Progenitor Environments and Stellar Cluster Association 81
    4.3.2 Hα Size–Luminosity Relation from HST Imaging 81
    4.3.3 [S II] Line Ratios and Electron Density Estimates 82

III SUMMARY 87
5 SUMMARY 89
  5.1 Main results 89
    5.1.1 A census of ~2200 new SNR candidates 89
    5.1.2 Metallicity environments of SNRs 90
    5.1.3 Multi-wavelength exploratory studies 90
  5.2 Significance 90
  5.3 Limitations 91
  5.4 Future directions 91
    5.4.1 Expanded IFS surveys 91
    5.4.2 Multi-wavelength integration 91
    5.4.3 Linking to theory and simulations 92
  5.5 Conclusion 92

IV APPENDIX 93
A APPENDIX FOR CHAPTER 2 95
  A.1 Masked regions within each galaxy 95
  A.2 Atlas of supernova remnant locations in PHANGS-MUSE galaxies 95
  A.3 Fitted emission lines and masked sky lines while running the data analysis pipeline. 101
  A.4 Catalog of objects identified in M83 101
B APPENDIX FOR CHAPTER 3 105
  B.1 Metallicity in D16 Calibration 105

C APPENDIX FOR CHAPTER 4 109

BIBLIOGRAPHY 115

LIST OF FIGURES

Figure 1 Schematic illustration of the evolutionary phases of core-collapse supernovae. The solid line shows the radius (left axis) increasing with time since explosion (x-axis), while the dashed line shows the velocity (right axis) decreasing. Credit: Micelotta, Matsuura & Sarangi (2018) and references therein. 9

Figure 2 Zoomed-in image on four regions, showing (from left to right) log Hα flux ($10^{-20} \mathrm{cm}^{-2} \mathrm{erg s}^{-1}$), [S II]/Hα, [S II]/Hα residual, [O I]/Hα residual, and [S II] velocity dispersion maps and log [S II] flux. Objects identified by our method as SNRs and SNR candidates are marked with black solid ellipses. Objects identified in the Groves et al. 2023 nebular catalog as H II regions are enclosed by red solid lines, while regions unclassified in that catalog are outlined with blue solid lines. Region contours in the first column are from Groves et al. (2023). The second column shows region contours identified by `astrodendro` without any photoionization correction. The remaining columns show regions identified by `astrodendro` after using our final selection methods. It is apparent that many of the regions in the second column are spurious. 26

Figure 3 Log([S II]/Hα) as a function of logarithm Hα surface brightness for all pixels in each galaxy. The red solid line is the fitted correlation for each galaxy, with slope and intercept values given in the legend of each panel. The black solid line is representative of the DIG relation, as measured between 0.40 R_{max} (maximum radial coverage) and 0.60 R_{max} for each galaxy from Belfiore et al. (2022). The gray area indicates the 3σ range of this relation. SNRs typically lie above the fitted lines and show a looping structure toward the upper right. The horizontal black dashed line indicates the typical value of [S II]/Hα = 0.4 used to select SNRs. Many low Hα surface brightness pixels associated with the DIG have [S II]/Hα $\geqslant$ 0.4. 28

Figure 4 log([O I]/Hα) as a function of log Hα surface brightness for all pixels in all 19 galaxies. The red solid line is the fitted global correlation for all galaxies, with slope and intercept provided in the lower right corner of this plot. The black solid line is representative of the DIG relation, as measured between 0.40 R_{max} (maximum radial coverage) and 0.60 R_{max} for each galaxy from Belfiore et al. (2022). The gray area indicates the 3σ range of this relation. The black dashed line indicates the theoretical value of [O I]/Hα = 0.017 to select SNRs (Kopsacheili, Zezas & Leonidaki 2020). The horizontal blue dotted line indicates the empirical value of [O I]/Hα = 0.1 used select SNRs. For NGC 1672, the individual pixels lying above the majority come from an SNe that just happened several days before our observation. 29

Figure 5 BPT diagrams with demarcation line from Kewley et al. (2006) with an indication of BPT distances as defined as the distance to the red solid extreme starburst lines. The plus sign (+) indicates positive distance where shock-heating dominates, while the minus sign (–) indicates negative distance where photoionization dominates. The top left and top right plots show the distribution density of nebular regions in these 19 galaxies (Groves et al. 2023). In the bottom left and bottom right plots, SNRs and SNR candidates are indicated by red and blue dots, respectively. Nebular regions tend to occupy the photoionized region, while SNRs are concentrated in the shocked areas. 33

Figure 6 Zoomed-in map (3 kpc × 3 kpc) of the SNR population recovered in one of the galaxies in our sample, NGC 628, using our five selection criteria (described in Sect. 2.3). Panels from top left to bottom right show the log Hα emission, [O I]/Hα residual map, [S II]/Hα residual map, [S II]λ6716 velocity dispersion, BPT distance (OI-OIII) map, and the BPT distance (SII-OIII) map. Objects selected by each individual criterion are marked with black ellipses in the corresponding subplot and the locations of objects classified as SNR are marked with red boxes. Pixels with low S/N ($\leqslant$5), and those corresponding to stellar sources, and the central region of the galaxy, have been masked (see text for details). 37

Figure 7 Example of what one SNR (in NGC 628) looks like when using the five criteria. This SNR is selected in the [O I]/Hα residual map, [S II]/Hα residual map, [S II]λ6716 velocity dispersion, BPT distance (OI-OIII), and BPT distance (SII-OIII) maps. The selection is marked with a black ellipse. 38

Figure 8 Fraction of objects in the parent sample (left) and SNR sample (right) that are identified by specific pairwise combination of our five criteria ([O I]/Hα residual, [S II]/Hα residual, [S II]λ6716 velocity dispersion, BPT distance (OI-OIII), and BPT distance (SII-OIII). 38

Figure 9 Parent sample of 2233 objects identified across the 19 PHANGS-MUSE galaxies, compared to the Hα emission. The galaxy name is in the upper left corner. SNRs are indicated by red dots while SNR candidates are in blue. The background shows the Hα map. Regions excluded from our search are outlined in solid black. Most galaxies have the center masked (see Appendix A.1 for more details). We observe SNRs to be distributed across the full field of view, and good qualitative correspondence with Hα bright sites of star formation (see Appendix A.2 for the rest of the galaxies). 39

Figure 10 Spectra for four SNRs and an H II region in NGC 628. Top two: SNRs with high [S II]/Hα value > 0.8; middle two: SNRs with high-velocity dispersion > 80 km s^{-1}; bottom one: H II region. Characteristic lines, e.g., [O I], [S II], [N II], and Hα are labeled in the plot. All SNRs have broader emission lines than the H II region, though this is most apparent in the two SNRs (NGC0628_17 and NGC0628_48) as they were selected to have particularly broad lines. The sky emission at [O I]λ6300Å, λ6363Å has been masked. 40

Figure 11 Distribution of identified objects and H II regions density (in grayscale) in the [O I]/Hα versus [S II]/Hα plane. Panel (a): SNRs (red dots); Panel (b): SNR candidates (blue dots). For objects that overlap with a H II region, the symbol is an empty circle in light red or blue. Identified objects tend to occupy different spaces than H II regions in the [O I]/Hα versus [S II]/Hα plane. However, this tendency is more obvious for a SNR than a SNR candidate. 55

Figure 12 SNRs in M83. The locations are indicated of SNRs identified by Long et al. (2022) (black boxes) and those identified by applying methods used in this work (red circles for SNRs and blue circles for SNR candidates). All the objects we identify as SNRs are also identified as SNRs in Long et al. (2022). Overall, 77% of our parent sample were previously identified as SNRs in the literature. 56

Figure 13 [S II]/Hα (top) and [O I]/Hα (bottom) versus Hα luminosity for SNRs (red dots) compared with the H II regions density distribution (in grayscale). For SNRs that overlap with a H II region, the symbol is an empty circle (in light red). Thresholds of [O I]/Hα=0.1 and [S II]/Hα=0.4 (horizontal dash-dotted lines) are shown. SNRs overlapping with H II regions are selected by other criteria so they can still be identified as SNRs. Emission lines are not corrected for the photoionization. 57

Figure 14 Radial trends of SNRs and H II regions. r/r_{eff} is the ratio of SNR distance to the effective radius of the corresponding galaxy. Panel (a): [S II]/Hα changes with the distance to their corresponding galactic centers for SNRs (red dots) and H II regions (in grayscale). Panel (b): [N II]λ6583/Hα change with the distance to their corresponding galactic centers for SNRs (red dots) and H II regions (in grayscale). For SNRs that overlap with a H II region, the symbol is an empty circle in light red. The drop in the numbers at low r/r_{eff} is likely influenced by the mask in the centers of the galaxies. 58

Figure 15 Comparison of emission-line ratios and velocity dispersion for supernova remnants (SNRs) and H II regions. Panel (a): Line ratios of [S II] versus velocity dispersion of SNRs and H II regions. The top axis shows the FWHM. The Hα velocity dispersion changes with the [S II]λ6716/[S II]λ6730 ratio for SNRs (red dots) and H II regions (in grayscale). The ratios above 1.4 are not physical and are due to noise. The horizontal dash-dotted lines indicate different electron densities with the corresponding value next to it. Panel (b): Velocity dispersion of Hα changes with [S II]λ6716,6730/Hα ratio for SNRs (red dots) and H II regions (in grayscale). For SNRs that overlap with a H II region, the symbol is an empty circle in light red. These two criteria work effectively together in distinguishing between SNRs and H II regions. 59

Figure 16 Comparison of supernova remnant properties with MAPPINGS models. Left: Observed [O III]λ5006/Hβ versus [N II]λ6583/Hα for SNRs (red dots). Right: Observed [N II]λ6583/Hα versus [S II]/Hα for SNRs (red dots). For SNRs that overlap with a H II region, the symbol is an empty light red circle. Background grids are MAPPINGS models with different metallicities. Our identified SNRs mostly lie between models for LMC and twice solar metallicities. 60

Figure 17 Relation between [S II]/Hα ratio and [N II]/Hα ratio for SNRs identified in four nearby galaxies from the literature (Long et al. 2018, 2022; Long, Winkler & Blair 2019; Winkler et al. 2021) and 19 MUSE galaxies. SNRs are marked with red dots; SNRs that overlap with a H II region are marked as an empty circle in light red. 60

Figure 18 Relation between [S II]/Hα ratio and [N II]/Hα ratio for SNRs in 19 galaxies. SNRs in the same galaxy are marked in the same color and with the symbol. In the legend, from top to bottom, the stellar mass of the galaxy decreases, from $10^{11} M_\odot$ for NGC 1365 to $10^{9.41} M_\odot$ for NGC 5068. 61

Figure 19 Comparison between the estimated SNR number from the SFR and objects identified in this paper. The lower limit of the identified object is the number of SNRs and the upper limit is the number in the parent sample including SNR candidates. The lower limit of the estimated SNR number is given by the optically visible time of SNRs for 10,000 years and the upper limit corresponds to 20,000 years. The dashed black line is the one-to-one relation. The shaded area provides coverage from two times the recovery rate to 50% of the recovery rate of SNRs. 61

Figure 20 Number of SNe as a function of stellar mass (left) and SFR (right) considering the entire parent sample, colored by galaxy distance and considering galaxy integrated properties measured only within the MUSE field of view. These SN counts can also directly be converted to a SN frequency by assuming SNRs are visible in the optical for 10,000 years. Lines of constant SN rate per unit mass (SNu) are also shown. The star markers represent the number for the parent sample while the circles are the number of SNRs. The line between them shows the range of possible true SNR numbers. 62

Figure 21 Probability distribution functions of [S II]/Hα for SNRs and SNR candidates that are isolated or overlap with H II region. More SNR candidates (bottom) overlap with H II regions (blended) and have lower [S II]/Hα values than SNRs (top). 63

Figure 22 The relation between metallicity residual and distance of H II regions to the SNRs. The average seeing is approximately 67 pc across all galaxies, and H II regions within this distance have been excluded to avoid seeing-related blending effects. 69

Figure 23 Cumulative distribution of star formation rate (SFR) as a function of 12+log(O/H). The black line shows the distribution for all H II regions in the 19 galaxies, while the red line represents H II regions located near SNRs. Dashed lines indicate the respective median metallicities. 71

Figure 24 Cumulative distribution of SFR as a function of [O/H] for individual galaxies. Each gray line corresponds to one galaxy's H II region distribution. Orange squares mark the metallicity and SFR rank of the corresponding SNR environments. The dashed black line at $12+\log_{10}(O/H) = 8.6$ indicates a solar-like metallicity threshold. The red dot denotes the median SNR metallicity across the full sample. 72

Figure 25 SNR occurrence per unit of star formation rate, plotted as a function of metallicity, estimated by dividing the number of SNRs by the total SFR within each 0.1 dex metallicity bin. The black points represent bin medians. Vertical error bars represent Poisson uncertainties in SNR counts. The orange dot marks the solar abundance (Asplund, Amarsi & Grevesse 2021), while the blue and purple dots represent median metallicities of the LMC and SMC, respectively (Domínguez-Guzmán et al. 2022). 73

Figure 26 Cumulative distribution functions (CDFs) of molecular gas surface density ($\Sigma_{\rm mol}$) at the locations of supernova remnants (SNRs; red curves) compared to supernova subtypes from Mayker Chen et al. (2023) (orange dashed = Type II, black dotted = stripped-envelope). Top panel: CDFs weighted by physical area. Bottom panel: CDFs weighted by enclosed molecular gas mass. Vertical lines indicate the mean $\Sigma_{\rm mol}$ for each population. 78

Figure 27 Locations of SNRs (circles) overlaid on JWST/MIRI images (zoom-in views) in four mid-infrared bands: F770W, F1000W, F1130W, and F2100W for NGC 628. 79

Figure 28 Projected distances between SNRs and the nearest compact cluster (a) and stellar association (b) from Maschmann et al. (2024). Both distributions show that most SNRs lie well beyond a few parsecs, implying that only a minority of progenitors exploded in situ. 83

Figure 29 Hα surface brightness versus physical diameter for isolated SNRs detected in HST narrowband imaging. While models predict that younger, denser remnants should be compact and bright, and older remnants larger and fainter, our heterogeneous sample shows only scatter, likely due to environmental variation and observational biases. 84

Figure 30 [S II]$\lambda 6716/\lambda 6730$ ratio as a function of SNR diameter, with dashed lines corresponding to electron densities of 10, 100, and 1000 cm^{-3}. Most SNRs lie in the 50–300 cm^{-3} range, with outliers tracing unusually dense or diffuse environments. 85

Figure 31 Same as in Fig. 9. 97

Figure 32 Same as in Fig. 9. 98

Figure 33 Same as in Fig. 9. 99

Figure 34 Same as in Fig. 9. 100

Figure 35 Cumulative distribution of SFR as a function of D16 metallicity ([O/H]). The black line shows all H II regions in the 19 galaxies, while the red line corresponds to H II regions close to SNRs. Dashed lines mark the median metallicity of each population. 105

Figure 36 Cumulative distributions of SFR fraction as a function of [O/H] for individual galaxies using the D16 calibration. Each gray line represents one galaxy. Orange squares indicate the [O/H] values and relative SFR ranks of H II regions near SNRs. The red dot marks the median of the entire SNR-associated H II region sample. The dashed black line at $12 + \log_{10}(O/H) = 8.6$ dex indicates a commonly used threshold for high metallicity (solar). 106

Figure 37 SNR occurrence per unit SFR as a function of [O/H], binned in 0.2 dex intervals using the D16 metallicity calibration. The y-axis shows the number of SNRs divided by the total SFR within each metallicity bin. This is the same as Fig. 25, but with metallicity derived using the D16 calibration. 107

Figure 38 RGB images for 19 PHANGS-MUSE galaxies. 109

Figure 39 RGB images for 19 PHANGS-MUSE galaxies (continued). 110

Figure 40 RGB images for 19 PHANGS-MUSE galaxies (continued). 111

Figure 41 RGB images for 19 PHANGS-MUSE galaxies (continued). 112

Figure 42 RGB images for 19 PHANGS-MUSE galaxies (continued). 113

LIST OF TABLES

Table 1 Properties of PHANGS–MUSE galaxies used in this work. 22
Table 2 Number of identified SNRs and SNR candidates in 19 galaxies. 35
Table 3 Parent sample catalog generated in this work (see text for details). Notes. (*) Measured emission lines are in Table A.2 in Appendix A.3. 42
Table A.1 Environmental masks applied to each criterion for 19 galaxies. 96
Table A.2 Fitted emission lines and masked sky lines 102
Table A.3 Identified objects in M83 (part). 103
Table A.4 Identified objects in M83 (continued). 104

LISTINGS

ACRONYMS

ISM	Interstellar Medium
SN	Supernova
SNe	Supernovae
SNR	Supernova Remnant
IFU	Integral Field Unit
MUSE	Multi Unit Spectroscopic Explorer
PHANGS	Physics at High Angular Resolution in Nearby GalaxieS

CCSNe	Core-collapse supernovae

Part I

LITERATURE

1

INTRODUCTION

1.1 GALAXIES & INTERSTELLAR MEDIUM

Galaxies are complex ecosystems composed of stars, gas, dust, and dark matter, evolving through a combination of internal processes and external interactions. A significant fraction of the baryonic mass in galaxies resides not in stars but in the Interstellar Medium (ISM), which plays a pivotal role in regulating star formation and galactic evolution (Kennicutt 1998; Putman, Peek & Joung 2012). The ISM is highly structured and multiphase, encompassing cold molecular clouds, warm ionized regions, and hot diffuse gas (Draine 2011; McKee & Ostriker 1977).

The structure of galaxies is governed not only by gravitational dynamics but also by the thermodynamic state of their ISM. Maintaining this multiphase structure requires a continuous input of energy to counteract radiative cooling and prevent large-scale collapse. Without sufficient energy injection, the thermal pressure alone cannot support the vertical structure of galactic disks, especially in star-forming regions (Ostriker, McKee & Leroy 2010).

Among the sources of energy input, stellar feedback plays a crucial role. This includes photoionization, stellar winds, and Supernova (SN) explosions. While all three mechanisms influence the ISM, Supernovae (SNe) are particularly significant due to their immense energy output ($\sim 10^{51}$ ergs per event) and their capacity to generate strong shocks that affect the ISM structure on large scales (Hopkins et al. 2014; Kim & Ostriker 2017). These shocks stir turbulence, heat the surrounding gas, and trigger or quench subsequent star formation. Moreover, SNe inject freshly synthesized heavy elements into the ISM, promoting chemical enrichment and contributing to the galactic metal budget (Nomoto et al. 2006).

Despite these advances, major uncertainties remain about how efficiently SNe couple their energy and metals to the ISM, and on what spatial scales this feedback is most relevant. Addressing these open questions is central to linking stellar evolution with galaxy-scale processes.

Star formation occurs predominantly within dense molecular clouds, but the process is far from isolated. Massive stars, once formed, rapidly shape their surroundings through ionizing radiation and winds, culminating in SN explosions that redistribute energy and metals. These feedback processes create a turbulent and self-regulating environment, influencing the next generation of star formation (Krumholz 2014).

Understanding the spatial distribution of metals within galaxies, and how these correlate with feedback-driven structures such as Supernova Remnants (SNRs), is essential for constraining models of galaxy formation and evolution. Observational studies have shown that gas-phase metallicities vary both radially and locally across galaxies, reflecting the combined effects of star formation history, gas accretion, outflows, and mixing processes (Sánchez et al. 2019; Zaritsky, Kennicutt & Huchra 1994). Spatially resolved spectroscopy, especially through Integral Field Units (IFUs) such as Multi Unit Spectroscopic Explorer (MUSE), has enabled detailed mapping of ISM conditions across nearby galaxies, revealing localized abundance variations associated with stellar feedback and small-scale star-forming regions (Kreckel et al. 2019). However, not all core-collapse SNe are coincident with bright H II regions, indicating a possible delay between star formation and explosion, or the dispersal of natal clouds prior to the SN event (Mayker Chen et al. 2024).

SNe provide an instantaneous view of stellar death and feedback, while their remnants (SNRs) offer a much longer-lived record of how that feedback interacts with the surrounding ISM. Studying both together therefore provides a uniquely powerful window into the life cycle of baryons in galaxies. In this context, SNRs serve as powerful probes of the ISM and its enrichment history. By studying the interplay between SNRs and their surrounding ionized gas, we gain insight into how feedback redistributes metals and modifies the ISM on sub-kpc scales. This sets the stage for exploring the physics of supernova explosions and remnants, and how they shape the observable signatures used to study galaxy evolution.

1.2 SUPERNOVA PHYSICS

Supernovae (SNe) are among the most energetic events in the Universe, releasing $\sim 10^{51}$ erg of energy in a single explosion. Depending on the progenitor systems, SNe are broadly classified into two main types: core-collapse supernovae (CCSNe), resulting from the gravitational collapse of massive stars ($8\,M_\odot$), and thermonuclear supernovae (Type Ia), arising from the runaway fusion of a white dwarf in a binary system (Filippenko 1997; Heger et al. 2003).

Core-collapse SNe mark the violent endpoints of massive star evolution and dominate the SN rate in star-forming galaxies (Li et al. 2011; Tammann, Loeffler & Schroeder 1994). They are typically associated with late-type, actively star-forming systems, whereas Type Ia SNe are also found in older, passive galaxies. These explosions not only terminate stellar lifecycles but also transform their environments: the extreme energy released produces strong shocks that alter the density, ionization, and turbulence of the surrounding medium (Hopkins et al. 2014; McKee & Ostriker 1977). In contrast to stellar winds or radiation, which act continuously but moderately, SNe deliver *impulsive* feedback, driving turbulence and outflows on scales well beyond their progenitor clouds (Kim & Ostriker 2017; Walch et al. 2015).

From a nucleosynthetic perspective, SNe are primary sources of heavy elements. Core-collapse SNe synthesize α-elements such as O, Ne, and Mg, while Type Ia SNe provide most of the iron-peak elements (Matteucci 2001). These distinct yields make SNe powerful diagnostics of stellar populations and chemical evolution: the abundance patterns they produce are long-lived tracers of star formation history and binary evolution across galaxies (Maiolino & Mannucci 2019).

Observationally, SNe also serve as direct probes of stellar populations and star formation rates. Their occurrence rates and spatial distributions constrain both the demographics of progenitor stars and the efficiency of binary channels (Li et al. 2011). Large-scale transient surveys have revealed correlations between SN rates and global galaxy properties such as stellar mass, metallicity, and star formation activity (Graur et al. 2017a), motivating efforts to link these trends to local interstellar conditions. The remnants they leave behind—supernova remnants (SNRs)—extend the observational window, preserving the imprint of explosions for 10^4–10^5 years. This makes them invaluable for studying how stellar feedback shapes the interstellar medium on resolved spatial scales.

In the following subsections, we discuss the classification of SNe, the mechanisms of their feedback, and the physical environments in which they occur. Particular attention is given to the role of CCSNe, whose progenitors dominate star formation regions, and to the diagnostic value of SNRs in connecting feedback processes with the chemical and dynamical structure of the ISM.

1.2.1 *Supernova Types*

Supernovae (SNe) are broadly classified into two main types: core-collapse supernovae (CCSNe), resulting from the gravitational collapse of massive stars, and thermonuclear (Type Ia) supernovae, which arise from the explosion of white dwarfs in binary systems (Filippenko 1997; Heger et al. 2003). CCSNe encompass a variety of subtypes (e.g., Type II, Ib/c, stripped-envelope), but in this work we group them together, as the classification of individual remnants is typically not feasible based on our available data.

This traditional classification is based primarily on optical spectra, particularly the presence or absence of hydrogen and helium lines. The two main categories differ not only in observational characteristics but also in progenitor channels, explosion mechanisms, and evolutionary timescales:

1. Core-collapse supernovae (CCSNe), including Type II and Type Ib/Ic, result from the core collapse of massive stars ($8\,M_\odot$) at the end of their nuclear lifetimes. These explosions produce most of the Universe's α-elements and inject substantial energy into the ISM (McKee & Ostriker 1977).

2. Type Ia SNe originate from the thermonuclear disruption of carbon–oxygen white dwarfs in binary systems, likely through accretion or mergers. They are the pri-

> mary sources of iron-group elements and serve as standardizable candles in observational cosmology (Maoz, Mannucci & Nelemans 2014).

While CCSNe occur promptly within $\sim 10^6$–10^7 years after star formation, Type Ia SNe exhibit a wide range of delay times, from a few hundred million to several billion years (Brandt et al. 2010; Maoz, Mannucci & Brandt 2012). The relative occurrence of each SN type therefore depends strongly on galaxy morphology, star formation activity, and stellar population age. In star-forming galaxies, CCSNe dominate the observed SN rate, comprising roughly 70–80% of all SNe, with Type II events accounting for about half and stripped-envelope (Ib/Ic/IIb) SNe contributing another ~25–30% (Graur et al. 2017a; Li et al. 2011). Type Ia SNe make up the remaining 20–30% in such systems. In contrast, in passive galaxies, Type Ia events overwhelmingly dominate (80–90%) due to the lack of young massive stars.

Understanding the rates and environments of different SN types is essential for constraining stellar evolution, binary interactions, and galactic chemical enrichment. These distinctions also form the basis for interpreting the demographics of supernova remnants, which is a central focus of this thesis.

1.2.2 *Supernova Feedback*

Supernova feedback is a key process in regulating star formation and shaping the multiphase structure of the ISM. When a SN explodes, it releases approximately 10^{51} erg of energy into the surrounding environment as kinetic energy, thermal energy, and radiation (Chevalier 1974). This injection can drive turbulence, heat and compress the gas, and even expel material from the galactic disk, thereby suppressing further star formation (Dekel & Silk 1986).

In particular, CCSNe occurring in stellar clusters can act collectively to form superbubbles and power large-scale outflows (Veilleux, Cecil & Bland-Hawthorn 2005). These mechanisms are crucial for understanding the regulation of baryon cycling and the development of galactic winds. SN feedback is widely implemented in theoretical models and cosmological simulations to reproduce observed galaxy scaling relations, such as the stellar mass–halo mass and mass–metallicity relations (Somerville & Davé 2015).

The efficiency of SN feedback depends sensitively on local environmental conditions. In dense environments, rapid radiative cooling can dissipate the energy quickly, limiting its impact. In contrast, low-density, low-metallicity environments allow for longer cooling times and more effective coupling of SN energy to the gas. Magnetic fields and pre-existing turbulence also influence how energy and momentum are distributed throughout the ISM (Kim & Ostriker 2015; Martizzi, Faucher-Giguère & Quataert 2015).

1.2.3 *Supernova Environment*

The environment into which a supernova explodes significantly affects its evolution, feedback impact, and observational characteristics. Metallicity is particularly important in this context, as it influences progenitor evolution, explosion conditions, and post-explosion dynamics.

For CCSNe, metallicity controls the mass-loss rate of massive stars via line-driven stellar winds (Vink, Koter & Lamers 2001). Higher metallicities lead to stronger winds and more extended circumstellar material, which in turn affects the structure of the surrounding medium and the early SN light curves (Smartt 2009). Lower-metallicity progenitors are more compact and may retain more of their initial mass until collapse.

For Type Ia SNe, metallicity affects the cooling rates and nuclear burning pathways of the white dwarf progenitor, influencing the nucleosynthetic yields and explosion energetics (Seitenzahl & Townsley 2017). This can affect both their cosmological utility and the role they play in galactic chemical enrichment.

On a galactic scale, the metallicity of the ISM regulates the gas cooling curve, impacting the dissipation of SN energy (Sutherland & Dopita 1993). In metal-rich regions, cooling is efficient, and the SN feedback is shorter-lived, whereas in metal-poor environments, the feedback may persist longer and drive stronger large-scale effects (Martizzi et al. 2015).

Recent observations reveal that supernovae are spatially clustered, often occurring in regions of active star formation and in chemically inhomogeneous environments (Krumholz, McKee & Bland-Hawthorn 2019). This enhances the importance of measuring the local metallicity around SNe and their remnants to understand both the progenitor population and the cumulative effects of feedback and enrichment.

At ~50–100 pc scales, Mayker Chen et al. (2024) finds that only ~41% of recent SNe are coincident with bright H II regions, suggesting that many explode either outside classical H II regions or after these regions have faded or been dispersed. Their results underscore the complexity of linking progenitors to local star-forming environments and motivate the use of spatial smoothing when studying environmental properties such as metallicity and star formation rate around supernova remnants. These considerations are central to the methodology adopted in this thesis.

These links between supernovae, their environments, and the multiphase ISM provide the broader physical framework within which this thesis investigates the metallicity properties of SNRs in nearby star-forming galaxies.

1.3 SUPERNOVA REMNANTS PHYSICS

Supernovae mark the terminal explosions of stars, briefly visible for days to months depending on the type, releasing large amounts of energy, momentum, and heavy elements into the surrounding ISM (Thornton et al. 1998). While the optical signature of the explosion fades rapidly, the long-lasting impact is encoded in the evolution of the resulting SNRs. These remnants, formed by the interaction between SN ejecta and the ambient medium, persist for 10^4–10^5 years, offering unique observational windows into the processes that regulate the thermal, chemical, and kinematic state of the ISM.

SNRs are expanding shock-heated structures where the decelerating ejecta drive shock fronts into the ISM, compressing magnetic fields and accelerating particles to relativistic speeds (Weiler & Sramek 1988). Although SNRs do not directly preserve the details of the explosion mechanism, their morphology, composition, and evolution reflect integrated signatures of progenitor properties and surrounding environmental conditions. As such, they remain critical agents in the long-term baryon cycle and chemical evolution of galaxies (Efstathiou 2000).

1.3.1 *Supernova Remnants Evolution*

The evolution of a SNR proceeds through several dynamical stages, each shaped by local ISM density, metallicity, and magnetic field structure (Fig. 1).

1. **Free Expansion (Blast Wave) Phase**: Lasting $\sim 10^2$–10^3 years, this initial phase is dominated by high-velocity ($10^4\,\mathrm{km\,s^{-1}}$) ejecta expanding into the surrounding medium. The swept-up mass remains small compared to the ejecta mass.

2. **Sedov-Taylor (Adiabatic) Phase**: When swept-up mass exceeds the ejecta mass, the remnant enters a self-similar adiabatic phase. Radiative losses are minimal and the expansion follows $R(t) \propto t^{2/5}$ (Sedov 1959). This phase lasts $\sim 10^4$–10^5 years and heats the ambient gas to 10^6–10^7 K. The shock velocities during this stage shape the observable line widths in emission lines across various bands.

3. **Radiative (Pressure-Driven Snowplow) Phase**: As the remnant cools, the shocked shell becomes radiative, forming a thin, dense layer that continues expanding due to residual pressure.

4. **Momentum-Conserving Phase and Dissipation**: Once thermal pressure diminishes, expansion proceeds under residual momentum until the remnant fades into the ambient medium over $\sim 10^6$ years. Remnant shapes at this stage are sensitive to ISM inhomogeneities.

The duration and morphology of these phases depend on environmental parameters. Low-density or metal-poor regions result in slower cooling and more extended Sedov phases (Thornton et al. 1998). High-density environments lead to more compact and rapidly evolving remnants.

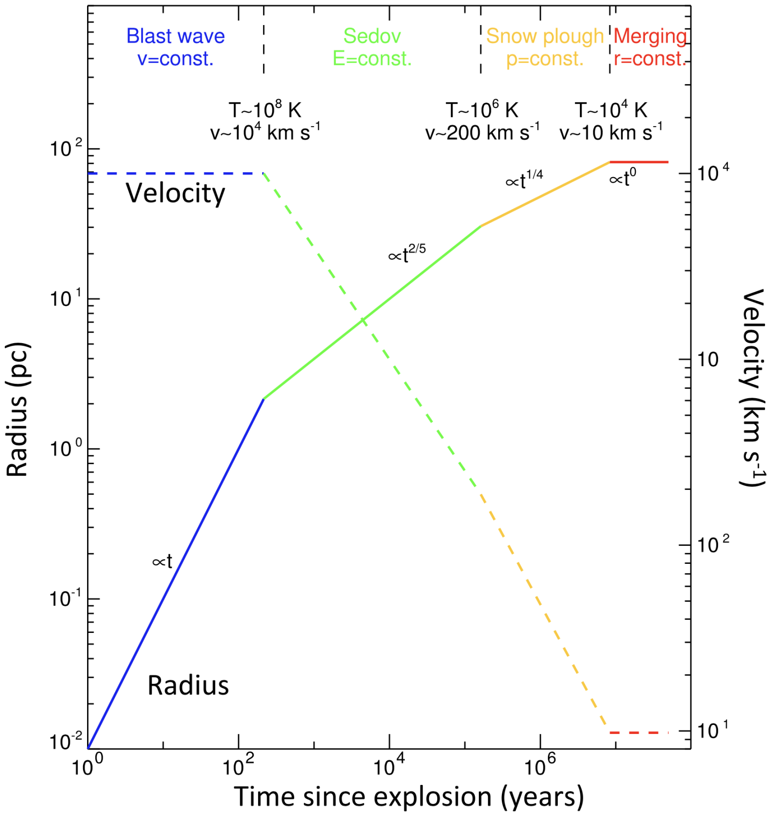

Figure 1: Schematic illustration of the evolutionary phases of core-collapse supernovae. The solid line shows the radius (left axis) increasing with time since explosion (x-axis), while the dashed line shows the velocity (right axis) decreasing. Credit: Micelotta, Matsuura & Sarangi (2018) and references therein.

1.3.2 *Supernova Remnants Observables*

Early extragalactic SNR studies examined basic criteria for identifying SNRs by optical or radio brightness and angular size, and compared their chemical abundances with those of H II regions (Dodorico 1978). Although the techniques and data were far more limited, fundamental issues such as distinguishing SNRs from H II regions and understanding environmental abundances remain central to modern studies.

SNRs emit across the electromagnetic spectrum, with each band tracing distinct physical conditions.

1.3.2.1 *Radio*

In radio, SNRs emit synchrotron radiation from relativistic electrons in shock-accelerated magnetic fields. This non-thermal emission traces the geometry of the shock and reveals cosmic-ray acceleration efficiency (Reynolds 2008). Over 300 Galactic SNRs have been identified in the radio (Green 2019), though selection effects likely render the sample incomplete by a factor of ~ 2–3 (Brogan et al. 2006). Radio surveys are particularly effective in dusty or embedded environments where optical lines are obscured.

1.3.2.2 *X-ray*

X-ray emission arises from shock-heated plasma, providing diagnostics of hot gas (10^6–10^7 K), density, and elemental abundances. Emission includes thermal bremsstrahlung and metal-line emission from highly ionized species (e.g., Fe, Si, O). High-resolution imaging from Chandra and XMM-Newton has mapped reverse shocks and ejecta distribution, constraining explosion asymmetries and nucleosynthesis yields (Vink 2011). More recently, wide-field soft X-ray surveys such as eROSITA have enabled improved SNR census in nearby galaxies (e.g., the Large Magellanic Cloud), discovering new remnants or candidates and comparing their X-ray morphology with optical and radio counterparts to better understand their shock-heated structures and environmental absorption (Zangrandi et al. 2024).

1.3.2.3 *Optical*

In the optical, SNRs are identified via shock-excited emission-line ratios, most commonly with [S II]/H$\alpha > 0.4$ (Blair & Kirshner 1985). Optical IFU spectroscopy, such as from MUSE, allows spatially resolved diagnostics of line ratios, abundances, and kinematics, enabling systematic surveys of SNRs in nearby galaxies (Emsellem et al. 2022; Li et al. 2024).

1.3.3 *Supernova Remnants Populations*

Population studies connect individual SNRs to galaxy-wide feedback and star formation histories.

In the Milky Way, ~300 confirmed SNRs are cataloged (Green 2019), although extinction and distance uncertainties limit completeness. X-ray and radio surveys preferentially detect different evolutionary stages, often biased toward either young (compact X-ray-bright) or old (radio-bright) remnants.

Extragalactic SNRs studies, especially in nearby galaxies (e.g., M33, M83, NGC 6946), benefit from known distances and face-on geometries. Narrow-band imaging and [S II]/Hα diagnostics identify hundreds of candidates (Lee & Lee 2014b; Matonick & Fesen 1997). However, these methods miss young, non-radiative SNRs or remnants in very low-density media.

Recent IFU surveys, such as PHANGS–MUSE, have enabled the detection of large, homogeneous SNR samples across diverse environments using kinematics, shocks, and line diagnostics (Long et al. 2022; Winkler et al. 2021; Winkler et al. 2023). These samples allow investigation of how SNR properties correlate with metallicity, stellar age, and feedback structures.

Motivated by this, several studies have examined how local ISM conditions affect SNR evolution. For example, Bozzetto et al. (2017) showed that in the Large Magellanic Cloud, core-collapse SNRs tend to occur in denser environments compared to Type Ia SNRs, indicating that environmental density, like metallicity can influence remnant visibility, morphology, and evolution. These findings underscore the importance of characterizing the local metallicity and star formation environment to interpret observed SNR populations in a physically meaningful way.

Theoretical simulations, including sub-grid SN feedback models and resolved hydrodynamic simulations, have also advanced in recent years (Keller et al. 2014; Smith, Sijacki & Shen 2018). These models are crucial for interpreting observational samples and understanding how SN feedback operates across spatial scales.

Despite these developments, observational biases remain: young remnants in optical, diffuse shells in radio, and faint X-ray remnants in metal-poor environments are still underrepresented. Multi-wavelength synergy and comparison with star formation tracers and chemical abundance maps are thus essential for building a complete picture of SNR populations and their role in galaxy evolution (Maoz & Badenes 2010; Sarbadhicary et al. 2017).

1.4 OPEN QUESTIONS

Despite substantial advances in our understanding of stellar feedback and its role in shaping the ISM, several key questions remain unresolved, many of which directly motivate the investigations presented in this thesis.

One major open question is how efficiently supernovae couple their energy into the surrounding ISM, and how this coupling depends on local environmental conditions such as gas-phase metallicity, density, or clustering of star formation. While theoretical models suggest that supernova feedback is essential for regulating the multiphase structure of the ISM, controlling star formation, and maintaining galactic pressure support, the observable signatures of such feedback, particularly in resolved and external galaxies, remain under debate. The specific scaling relations affected include the star formation efficiency, mass–metallicity relation, and stellar mass–halo mass relation (Somerville & Davé 2015).

A second challenge lies in the detectability and persistence of localized chemical enrichment from individual or clustered core-collapse supernovae. These explosions are well established as dominant sources of α-elements, yet whether their yields leave identifiable imprints in the surrounding H II regions depends on the explosion timescales, mixing efficiency, and background metallicity gradient. Most current observations lack the spatial resolution or sample size to robustly test these effects across statistically meaningful populations of supernova remnants, especially on 100 pc scales where feedback is expected to be strongest.

Third, a key theoretical uncertainty concerns the placement of supernovae with respect to different phases of the ISM. The effectiveness of SN feedback depends not only on the total energy released but also on where within the galactic ISM that energy is injected. Recent simulation work (e.g., the SILCC project; Walch et al. 2015) has demonstrated that explosions occurring in low-density environments can efficiently drive turbulence and outflows, whereas those in dense gas may lose energy rapidly through radiative cooling. However, observational constraints on the relative positioning of supernovae and ISM phases remain limited. Determining whether SNe tend to explode in dense star-forming clouds, interarm regions, or superbubbles carved by previous generations of feedback is crucial for constraining feedback prescriptions in cosmological models. Observationally, recent work shows that only ~41% of CCSNe are found within bright H II regions, suggesting significant delays, movement of progenitors, or pre-explosion clearing of the local environment (Mayker Chen et al. 2024).

A fourth open problem concerns the systematic identification and characterization of SNRs in external galaxies. While the Milky Way and Magellanic Clouds host the most well-studied SNRs due to their proximity and multi-wavelength coverage, distance uncertainties, extinction, and projection effects complicate their use in population studies. For more distant galaxies, especially beyond the Local Group, new techniques are needed, such as optical IFU spectroscopy to distinguish shocked gas from photoionized emission in crowded star-forming environments. These limitations restrict both the completeness of SNR catalogs and our ability to draw statistical conclusions about feedback processes across different galactic environments.

Finally, the relationship between SNR populations and their host galaxy properties, like star formation rate, metallicity, or dust content, remains poorly constrained. While simulations predict that the impact of supernova feedback depends strongly on these global properties, few observational studies have connected resolved SNR demographics to host galaxy-scale trends. Such connections are critical not only for interpreting current observations but also for calibrating sub-grid feedback models used in large-scale simulations of galaxy formation.

These questions form the basis for the work presented in this thesis:

- In Chapter 2, we present a new catalog of 2,233 SNR candidates across 19 nearby star-forming galaxies using MUSE spectroscopy, providing one of the largest homogeneous extragalactic samples to date.

- In Chapter 3, we investigate the local gas-phase metallicity around SNRs to test whether recent supernova activity leaves a detectable imprint in the chemical environment and explore how enrichment signatures vary with ISM conditions.

- In Chapter 4, we outline future directions including multi-wavelength follow-up, spatial cross-matching with molecular clouds and dust maps, and theoretical comparisons, with the goal of closing the remaining gaps in our understanding of SNR feedback.

By systematically addressing these questions, this thesis contributes to a more complete and empirically grounded picture of how supernovae (SNe) and their long-lived remnants (SNRs) shape the physical and chemical evolution of galaxies.

Part II

MAIN

Here we list published work, to be published work and exploratory works.

2

DISCOVERY OF ~2200 NEW SUPERNOVA REMNANTS IN 19 NEARBY STAR-FORMING GALAXIES WITH MUSE SPECTROSCOPY

This chapter, including Appendix A, comprises the article published in *Astronomy & Astrophysics*, Volume 690, Article A161, published online on 3 October 2024. The paper has been reformatted to match the thesis style. DOI: 10.1051/0004-6361/202450730

Contributions: The thesis author served as the lead author of this publication and was responsible for all text, data analysis, and figure production. The project was initiated and scientifically supervised by Dr. Kathryn Kreckel, who provided guidance on the overall direction and gave extensive feedback on the manuscript and figures. Dr. Sumit Sarbadhicary contributed through regular discussions and technical input, particularly regarding coding strategies. Other co-authors offered feedback on specific aspects of the analysis. In particular, Dr. Knox Long provided expert advice on the comparison to the M83 SNR catalog.

Abstract: Supernova feedback injects energy and turbulence into the interstellar medium (ISM) in galaxies, influences the process of star formation, and is essential to understanding the formation and evolution of galaxies. In this paper we present the largest extragalactic survey of SN candidates in nearby star-forming galaxies using exquisite spectroscopic maps from MUSE. SNe exhibit distinctive emission-line ratios and kinematic signatures, which are apparent in optical spectroscopy. Using optical integral field spectra from the PHANGS–MUSE project, we identified SNRs in 19 nearby galaxies at ~100 pc scales. We used five different optical diagnostics: (1) line ratio maps of [S II]/Hα; (2) line ratio maps of [O I]/Hα; (3) velocity dispersion map of the gas; and (4) and (5) two line ratio diagnostic diagrams from Baldwin, Phillips & Terlevich (BPT) diagrams to identify and distinguish SNRs from other nebulae. Given that our SNRs are seen in projection against H II regions and diffuse ionized gas, in our line ratio maps we used a novel technique to search for objects with [S II]/Hα or [O I]/Hα in excess of what is expected at fixed Hα surface brightness within photoionized gas. In total, we identified 2,233 objects using at least one of our diagnostics, and defined a subsample of 1,166 high-confidence SNRs that were detected with at least two diagnostics. The line ratios of these SNRs agree well with the MAPPINGS shock models, and we validate our technique using the well-studied nearby galaxy M83, where all the SNRs we found are also identified in literature catalogs, and we recovered 51% of the known SNRs. The remaining 1,067 objects in our sample were detected with

only one diagnostic, and we classified them as SNR candidates. We find that ~35% of all our objects overlap with the boundaries of H II regions from literature catalogs, highlighting the importance of using indicators beyond line intensity morphology to select SNRs. We find that the [O I]/Hα line ratio is responsible for selecting the most objects (1,368; 61%); however, only half are classified as SNRs, demonstrating how the use of multiple diagnostics is key to increasing our sample size and improving our confidence in our SNR classifications.

Authors: Jing Li (李婧), Kathryn Kreckel, Sumit Sarbadhicary, Oleg V. Egorov, Brent Groves, Knox S. Long, Enrico Congiu, Francesco Belfiore, Simon C. O. Glover, Ashley .T Barnes, Frank Bigiel, Guillermo A. Blanc, Kathryn Grasha, Ralf S. Klessen, Adam Leroy, Laura A. Lopez, J.Eduardo Méndez-Delgado , Justus Neumann, Eva Schinnerer, Thomas G. Williams.

2.1 INTRODUCTION

The interstellar media (ISM) of galaxies are dotted with supernova remnants (SNRs), which are emission nebulae produced by supernova (SN) shocks propagating through the ambient ISM.Over 300 SNRs have been discovered in the Milky Way (Green 2019), and more than a thousand SNRs and SNR candidates have been found in external galaxies from multiwavelength surveys (see Long 2017; Vučetić, Arbutina & Urošević 2014, and references therein). SNRs are vital to our understanding of collisionless shocks (e.g., Chevalier, Kirshner & Raymond 1980; Marcowith et al. 2016; McKee & Hollenbach 1980; Raymond 1979), cosmic ray acceleration (Bell et al. 2013; Blandford & Eichler 1987; Blasi 2013), progenitor models and explosion physics of supernovae (SNe) (e.g., Chevalier 2005; Krause et al. 2008; Patnaude & Badenes 2017; Schaefer & Pagnotta 2012), the formation and survival of dust grains in SN ejecta (e.g., Dwek & Arendt 1992; Sarangi, Matsuura & Micelotta 2018; Williams & Temim 2016), the properties of central compact objects (e.g., Dubner et al. 1998; Holland-Ashford et al. 2017; Katsuda et al. 2018), and the effects of shocks on interstellar clouds (e.g., Koo et al. 2020; Reach et al. 2006; Slane et al. 2015; White & Long 1991).

Extragalactic SNR surveys provide a unique perspective into the evolution of SNR shocks, their stellar progenitors, and impact on the surrounding ISM. They are complementary to Galactic SNRs, which undoubtedly offer the most detailed multiwavelength views of shocks (e.g., Milisavljevic et al. 2024), but are also affected by distance uncertainties, variable line-of-sight extinction, and source confusion at low latitudes where most objects are located (e.g., Green 2005; Green et al. 2008; Reach et al. 2006). Examples of well-studied extragalactic SNR populations include those in the Magellanic Clouds (e.g., Long, Helfand & Grabelsky 1981; Maggi et al. 2016; Maggi et al. 2019; Mathewson & Clarke 1973), M31 (Galvin & Filipovic 2014; Lee & Lee 2014a; Magnier et al. 1995), M33 (Gordon et al. 1999; Lee & Lee 2014b; Long et al. 2018; Long et al. 2010; White et al. 2019), M83 (e.g., Blair et al. 2014; Dopita et al. 2010; Long et al.

2022; Winkler, Blair & Long 2017), NGC 6946 (e.g., Lacey, Duric & Goss 1997; Long et al. 2020, 2019; Matonick & Fesen 1997), M51 (Winkler et al. 2021), and the Sculptor Group galaxies (e.g., Blair & Long 1997; Kopsacheili et al. 2024; Pannuti et al. 2002, 2000).

With extragalactic surveys, one can observe the distribution of SNRs of different ages across entire galaxies for face-on galaxies at the known fixed distances of the galaxies. This leads to reliable estimates of SNR sizes and luminosities at different wavelengths, from which one can infer a variety of statistical information about the SNR population, such as the distribution of evolutionary stages, visibility times, ambient densities, and magnetic field properties (Asvarov 2014; Badenes, Maoz & Draine 2010; Chomiuk & Wilcots 2009; Elwood, Murphy & Díaz-Rodríguez 2019; Gordon et al. 1999; Long et al. 2010; Sarbadhicary et al. 2017; Thompson, Quataert & Murray 2009). The spatial correlation of these SNRs with ISM and stellar population surveys of nearby galaxies have led to unique constraints on the progenitor age distribution of SNe (e.g., Auchettl et al. 2019; Badenes et al. 2009; Díaz-Rodríguez et al. 2018; Jennings et al. 2014; Koplitz et al. 2021; Maoz & Badenes 2010; Williams et al. 2019, 2014), highly relevant to the many open questions about progenitor models of Type Ia and core-collapse SNe (see Maoz et al. 2014; Smartt 2015, for detailed discussion).

The discovery and identification of these extragalactic SNRs have been primarily at optical wavelengths from observations of forbidden emission lines. The most widely used diagnostic to distinguish SNRs from photoionized nebulae has been the $[\mathrm{S\,II}]/\mathrm{H}\alpha > 0.4$ criterion (e.g., Dodorico, Dopita & Benvenuti 1980; Mathewson & Clarke 1973; Parker et al. 1979), since low-ionization species like S^+ are more abundant in the extended recombination zones of radiative shocks compared to H II regions (Allen et al. 2008; Dopita et al. 2005; Raymond 1979). This contrasts with the Milky Way, where SNRs are primarily identified with radio continuum observations that can pierce through the midplane dust, and the power-law index of their synchrotron spectra can be measured (Anderson et al. 2017; Cotton et al. 2024; Dokara et al. 2021; Green 2019). The Magellanic Clouds also have a significant number of SNRs identified at X-ray (for young SNe) and radio wavelengths (e.g., Bozzetto et al. 2023; Kavanagh et al. 2022; Maggi et al. 2016; Maggi et al. 2019; Zangrandi et al. 2024). Beyond the Local Group, however, radio and X-ray observations have yet to reach sufficient spatial resolution and sensitivity to independently discover large numbers of SNRs like optical surveys (Russell et al. 2020).

Most optical SNR surveys have relied on narrowband filter imaging, which, despite its success in discovering many SNRs, is not without its limitations. A major issue is the continuum subtraction, which is done by scaling the flux from a broadband image or an off-band narrowband image. This was often suboptimal in surveys, due to variable seeing conditions and color properties of stars in the fields (e.g., Blair et al. 2014; Dopita et al. 2010), which particularly affected the recovery of faint, low surface brightness SNRs (Long et al. 2022). Typically the filters blended adjoining lines, such as the [N II]λ6549,6583 and Hα, which compromised the [S II]/Hα ratio (Blair et al. 2014). As a result, narrowband imaging and band ratios alone were often not sufficient to confirm objects as SNRs, and additional medium- or high-resolution follow-up spectroscopy of individual objects was necessary to provide additional line ratios and kinematic indicators (Long et al. 2018; Winkler et al. 2017).

The proliferation of wide-field integral field unit (IFU) spectroscopy with instruments such as Multi Unit Spectroscopic Explorer (MUSE) (Bacon et al. 2010) and Spectromètre Imageur à Transformée de Fourier pour l'Etude en Long et en Large de raies d'Emission (SITELLE) (Drissen et al. 2019) has significantly improved our ability to survey extragalactic nebulae with comparable efficiency as narrowband imaging, while at the same time circumventing many of its shortcomings. The ability to obtain a spectrum per pixel at high sensitivity and medium spectral resolution ($R > 10^3$) has led to more accurate modeling and subtraction of the underlying stellar continuum, and separation of adjoining emission lines. Integral field spectrograph has also opened up access to additional line diagnostics for identifying SNRs, such as [O I] and [O II] (Fesen, Blair & Kirshner 1985); linear combinations of S, N, and O forbidden lines (Kopsacheili et al. 2020); and the widths of forbidden emission lines, which are expected to be broader than in H II regions due to the presence of high-velocity shocked material (Points et al. 2019). The promise of IFU-based SNR searches have already been demonstrated in individual galaxies such as NGC 300 (Roth et al. 2018), NGC 3344 (Moumen et al. 2019), NGC 4030 (Cid Fernandes et al. 2021), M83 (Long et al. 2022), and NGC 4214 (Vicens-Mouret et al. 2023), with more recent work building toward cataloging thousands of shock-ionized nebulae across larger galaxy samples (Congiu et al. 2023, hereafter C23).

In this paper we push the boundaries of extragalactic SNR studies even further, to a sample of 19 galaxies in the range of $5-20$ Mpc, as part of the Physics at High Angular Resolution in Nearby GalaxieS (PHANGS)-MUSE survey (Emsellem et al. 2022). We have already characterized and constructed catalogs of likely H II regions and DIG in these galaxies (see, e.g., Belfiore et al. 2022; Congiu et al. 2023; Egorov et al. 2023; Emsellem et al. 2022; Groves et al. 2023; Santoro et al. 2022), which is critical for identifying SNRs. Although at these distances the SNRs are unresolved or barely resolved (average spatial resolution of 67 pc), this is the largest single survey of extragalactic SNRs ever conducted, with a diverse sample of host galaxies that span a range of stellar masses and star formation rates. These galaxies have substantial multiwavelength data at ~1" resolution or better from facilities including, but not limited to, Hubble Space Telescope (HST), James Webb Space Telescope (JWST), Atacama Large Millimeter/submillimeter Array (ALMA), Karl G. Jansky Very Large Array (VLA), AstroSAT, and Chandra X-ray Observatory (CXO). This multiwavelength synthesis provides the most complete observational census of the multiphase ISM and the multigeneration stellar population that are associated with SN explosions.

The focus of the current paper is to introduce the catalog, the selection procedure adopted, and the basic properties of the PHANGS-MUSE SNRs. Subsequent papers will investigate the correlation of these SNRs with stellar population and ISM maps of the galaxies. The paper is organized as follows. In Sect. 3.2 we introduce the PHANGS-MUSE dataset for our sample. Then in Sect. 2.3 we explore methods for identifying SNRs in these galaxies and describe how we constructed our catalogs. The resulting catalogs and SNRs properties are presented in Sect. 3.3. Further discussion and comparison with literature works are included in Sect. 3.4. Finally, we summarize the main conclusions in Sect. 2.6.

Table 1: Properties of PHANGS–MUSE galaxies used in this work.

Name	parent number	SNRs number	Distance [Mpc]	plate scale pc/″	$\log(M_\star)$ [$M_\odot$]	log(SFR) [$M_\odot yr^{-1}$]	PA [deg]	i [deg]	Survey Area [kpc^2]
IC 5332	36	24	9.0	43.7	9.68	-0.39	74.4	26.9	34
NGC 628	120	79	9.8	47.7	10.34	0.24	20.7	8.9	89
NGC 1087	123	29	15.9	76.8	9.94	0.11	359.1	42.9	126
NGC 1300	23	15	19.0	92.1	10.62	0.07	278.0	31.8	356
NGC 1365	63	38	19.6	94.9	11.00	1.24	201.1	55.4	409
NGC 1385	114	63	17.2	83.5	9.98	0.32	181.3	44.0	101
NGC 1433	46	24	18.6	90.3	10.87	0.05	199.7	28.6	426
NGC 1512	25	20	18.8	91.3	10.72	0.11	261.9	42.5	266
NGC 1566	180	101	17.7	85.8	10.79	0.66	214.7	29.5	208
NGC 1672	61	28	19.4	94.1	10.73	0.88	134.3	42.6	250
NGC 2835	187	119	12.2	59.2	10.00	0.10	1.0	41.3	87
NGC 3351	46	24	10.0	48.3	10.37	0.12	193.2	45.1	73
NGC 3627	152	86	11.3	54.9	10.84	0.59	173.1	57.3	85
NGC 4254	332	154	13.1	63.5	10.42	0.49	68.1	34.4	169
NGC 4303	303	130	17.0	82.4	10.51	0.73	312.4	23.5	214
NGC 4321	132	80	15.2	73.7	10.75	0.55	156.2	38.5	191
NGC 4535	75	54	15.8	76.5	10.54	0.34	179.7	44.7	124
NGC 5068	194	92	5.2	25.2	9.41	-0.56	342.4	35.7	23
NGC 7496	21	6	18.7	90.8	10.00	0.35	193.7	35.9	92

Notes. For Cols. *parent* and *SNRs*, see Sect. 2.3.1.4 for their detailed classification. Distances of PHANGS galaxies come from Anand et al. 2020, with a complete set of references provided in the acknowledgments. Their stellar masses and star formation rates (SFRs) are from Leroy et al. 2021. Position angle (PA) and inclination (i) come from the CO (2-1) dynamics of PHANGS-ALMA (Lang et al. 2020). Survey areas are using the values from Belfiore et al. 2022.

2.2 DATA

We selected SNRs using data from the PHANGS-MUSE survey of 19 nearby (20 Mpc) galaxies, conducted using the Multi Unit Spectroscopic Explorer (MUSE) instrument mounted on the Very Large Telescope (VLT) in Chile (Bacon et al. 2010). MUSE provides ~arcsecond-resolution integral field spectroscopy in the wavelength range of 4800 to 9300 Å at a spectral resolution of $R \sim 3000$. Full details of the sample, observations, reductions, and data products are found in Emsellem et al. (2022). These 19 galaxies (see Table 1) populate the star-forming main sequence of galaxies, with stellar masses in the range of $10^{9.4} - 10^{11} M_{\odot}$. The pixel scale is 0.2"/pixel and the typical seeing in R-band is 0.8" (Emsellem et al. 2022), corresponding to an average spatial resolution of 67 pc at the distance of our targets (Anand et al. 2020; Scheuermann et al. 2022). Our ~100 pc resolution is larger than the typical size of SNRs (Asvarov 2014; Long et al. 2010; Tüllmann et al. 2011), but is well suited to spatially distinguish SNRs from nearby unrelated H II regions and surrounding DIG. To limit the effects of spatial blending between SNRs and surrounding line emitting regions we used the native resolution data, which provide the best possible spatial resolution at the expense of a lightly varying point spread function (PSF) between fields. As many of the regions are found to be blended with luminous H II regions (see Sect. 2.5.3), our source identification is limited more by seeing than by sensitivity. Using smoothed data (e.g., the "copt" data products), we obtain a sample of objects that is 60% smaller.

The main PHANGS-MUSE data products we used are the total line intensity and kinematic (velocity and velocity dispersion) maps for the set of strong lines discussed below. A detailed description of the datasets, including the data analysis pipeline (DAP) used to extract these parameters, is given in Emsellem et al. 2022, and here we provide a summary. Spectral fitting is performed by using the penalized pixel-fitting code `pPXF` (Cappellari 2017; Cappellari & Emsellem 2004). The stellar continuum in the spectra was identified and removed using stellar population templates from the E-MILES simple stellar population models (Vazdekis et al. 2016). Emissions lines were fitted with Gaussian templates to recover line fluxes as well as line kinematics (velocity and velocity dispersion). We note that at the MUSE spectral resolution, we generally find that the line emission associated with SNRs is well described by single Gaussian fits. In `pPXF`, we performed fitting for 23 lines along with their corresponding gas kinematics. The kinematics of some emission lines were grouped together and fitted simultaneously, such as Balmer lines, and both low- and high-ionization lines. In this work we used [S II]λ6716, [S II]λ6730, Hα, [O I]λ6300, [O III]λ5006 fluxes and [S II]λ6716 velocity dispersion. We note that Hα and [S II], lines commonly used for SNR identification, are fit independently. Variations in seeing due to the differences in wavelength between these line maps are negligible (<0.01"; Emsellem et al. 2022). For fluxes, a signal-to-noise ratio (S/N) cut of $S/N \geqslant 5$ is applied, while for the velocity dispersion, a higher cut S/N $\geqslant$ 20 is used (Egorov et al. 2023), hereafter E23. These S/N cuts are applied before identifying SNRs in all maps.

We also made use of the Groves et al. (2023) and Santoro et al. (2022) catalog of H II regions to compare with our SNR properties. Groves et al. (2023) identified 23,244 nebulae as H II regions, imposing on a S/N cut of five for all emission lines and using Baldwin, Phillips & Terlevich (BPT) diagnostics ([O III]/Hβ versus [O I]/Hα and [O III]/Hβ versus [S II]/Hα) for classification (Baldwin, Phillips & Terlevich 1981; Kauffmann et al. 2003; Kewley et al. 2001).

Before selecting objects from the images, we also masked and excluded regions that suffer from contamination by foreground stars (provided as star masks by Emsellem et al. 2022), as well as regions where the ionized gas may have shocks from processes other than SNRs. For example, regions close to the galactic centers and bars can exhibit line ratios and physical conditions consistent with widespread shocks caused by large-scale supersonic inflows or outflows of gas (Athanassoula 1992; López-Cobá et al. 2022). In addition, some of the galaxies in our sample (e.g., NGC 1365) contain active galactic nucleus (AGN), which also strongly affects the line ratios in the central regions. As a result, we used the environments defined in Querejeta et al. (2021) to mask the centers of all galaxies to avoid shocked emissions from potential AGN, and the bar region for galaxies showing increased gas turbulence over large areas. For bar regions that were without increased shocked regions, we did not mask them off (see Table A.1 in Appendix A.1 for a complete list of which environmental mask is applied for each galaxy).

2.3 METHODS

2.3.1 *Parent sample identification*

Distinguishing SNR from other nebulae is a long-standing problem in nearby galaxies (Rhea et al. 2023; Sabbadin, Minello & Bianchini 1977). At ~100 pc resolution, most ionized nebulae appear to be luminous and compact sources. However, with multiple emission-line diagnostics, it is possible to find and classify SNRs.

The [S II]/Hα line ratio is historically the most commonly used diagnostic (Blair, Kirshner & Chevalier 1981; Blair & Long 2004) to separate SNRs from H II regions. This diagnostic works because the shocked region is richer in warm [S+] with respect to H II regions, which translate into a much higher [S II]/Hα line ratio (Allen et al. 2008). A similar situation applies to [O I]. Indeed, the [O I]/Hα line ratio has been predicted to be a better diagnostic for distinguishing SNRs and H II regions than the more commonly used [S II]/Hα line ratio (Kopsacheili et al. 2020). However, this emission line is normally weaker than [S II], and in the very local universe, it can be affected by blending with sky line airglow emission. Thanks to the redshift of our sample, the intrinsic [O I] emission is shifted from sky emission, and the depth of our MUSE data allows us to obtain sufficient S/N in our [O I] fluxes to consider it in our selection of SNRs.

Another prominent feature of SNRs is their broad emission-line profiles arising from the presence of fast radiative shocks of ~200 km s^{-1} (Long 2017), which significantly exceeds the typical ~20 km s^{-1} velocity dispersion of H II regions (Winkler et al. 2015). This kinematic information provides a promising alternate identification method (Egorov et al. 2023; Long et al. 2022; Points et al. 2019; Winkler, Long & Blair 2023). Finally, by combining multiple line ratios (such as in BPT diagrams) it is possible to determine the dominant ionization mechanism, whether it is photoionization-dominated or shock-dominated (Congiu et al. 2023; Makarenko et al. 2023).

We explore the use of five different criteria in this paper. These are the [S II]/Hα line ratio, the [O I]/Hα line ratio, the [S II]λ6716 velocity dispersion (σ) and two BPT diagnostics: [O I]-[O III] and [S II]-[O III]. We identify objects using each of these five different criteria separately and combine these catalogs to construct our "parent sample" of objects, which we later classify as either SNRs or SNR candidates. All these criteria are explained below in more detail.

The Python package `astrodendro`[1] was used to select objects from line ratio maps and line kinematic maps `astrodendro` is a tool used for calculating dendrograms (Rosolowsky et al. 2008), which visually represent the hierarchical clustering of data points, particularly in astronomical data analysis. We use astrodendro to identify regions around local maxima (above a threshold `min_value`), selected based on their contrast with the surrounding pixels (`min_delta`) and required to have a minimum associated area that indicates the line ratio to be coherent over about the area of a PSF.

We require regions used in further analysis to contain at least 10 pixels, which is the approximate area of the PSF. This ensures that all considered regions are detected over the whole area of the PSF and do not reflect an artifact or 'hot pixel.' We further require all regions to have a diameter of less than 200 pc, as otherwise they would be unphysically large compared to literature catalogs of SNRs (Asvarov 2014).

In this analysis, we do not aim to produce a complete catalog of SNRs in these galaxies but rather try to provide a sample that is as pure as possible. Many of the choices made in the following sections are designed to minimize the selection of spurious objects, such that all of the objects in our final catalog are credible SNRs and SNR candidates, as judged in a subsample of objects by visual inspection. The well-studied nearby galaxy M83 is used as a benchmark to validate our method in Sect. 2.3.3, and we compare with other approaches to identify 'shocked' nebulae in Sect. 2.5.4.

2.3.1.1 *Selection via [S II]/Hα and [O I]/Hα*

[S II] emission arises not only from shocks in SNRs but also through photoionization, such as in H II regions or the DIG. We initially tried to identify SNRs directly from

---

[1] https://dendrograms.readthedocs.io/en/stable/index.html

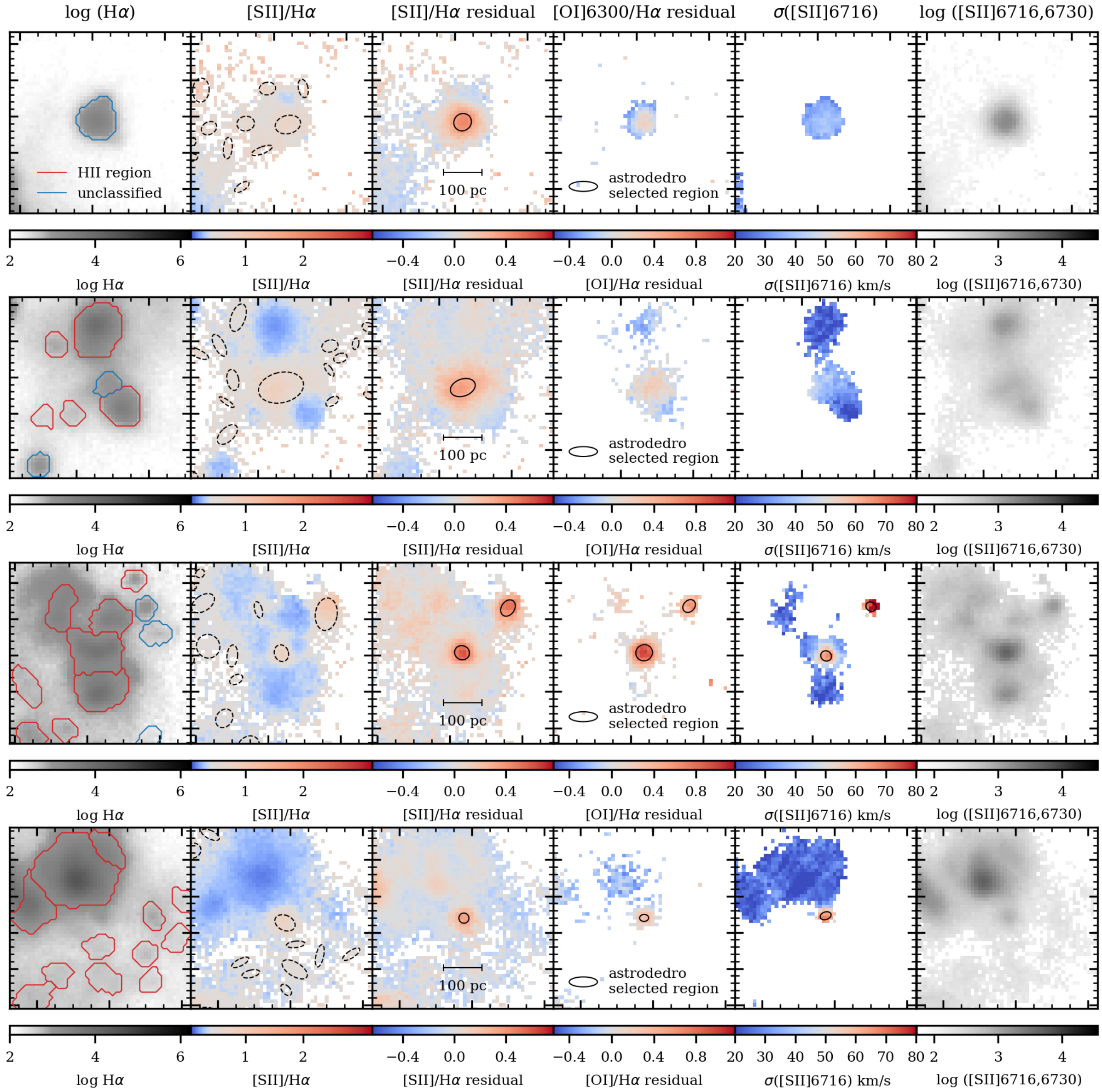

Figure 2: Zoomed-in image on four regions, showing (from left to right) log Hα flux ($10^{-20}\mathrm{cm}^{-2}\mathrm{erg}\,\mathrm{s}^{-1}$), [S II]/Hα, [S II]/Hα residual, [O I]/Hα residual, and [S II] velocity dispersion maps and log [S II] flux. Objects identified by our method as SNRs and SNR candidates are marked with black solid ellipses. Objects identified in the Groves et al. 2023 nebular catalog as H II regions are enclosed by red solid lines, while regions unclassified in that catalog are outlined with blue solid lines. Region contours in the first column are from Groves et al. (2023). The second column shows region contours identified by `astrodendro` without any photoionization correction. The remaining columns show regions identified by `astrodendro` after using our final selection methods. It is apparent that many of the regions in the second column are spurious.

the line ratio maps, and ran `astrodendro`, identifying peaks where the `min_value` was set to a threshold of 0.4 in [S II]/Hα and a threshold of 0.017 in [O I]/Hα, based on shock models (Kopsacheili et al. 2020). We found 36,826 objects in the [S II]/Hα maps and 15,891 objects in the [O I]/Hα maps. This implies nearly 1000 − 2000 SNRs per galaxy, which appears unphysically high (although see Sect. 2.5.1) considering that even galaxies like M83, NGC 6946, and M51, which have similar star formation rates as the PHANGS sample and are about a factor of 2-4 closer, only have on the order of a few hundred SNRs that have been spectroscopically identified (Long et al. 2022; Winkler et al. 2021).

Visual inspection reveals that the majority of these objects found in the PHANGS-MUSE sample are at the boundaries of H II regions and at low Hα surface brightness, implying they are either artifacts due to noise or associated with DIG. Figure 2 shows cutout images of four areas in NGC 628 and the regions identified within them. These images compare the region boundaries identified in the Groves et al. 2023 nebular catalog, where objects were identified via their Hα morphology, with the objects identified by `astrodendro` using the [S II]/Hα and [O I]/Hα ratio maps. The first column illustrates objects identified by Groves et al. 2023 and classified as H II regions (red lines) or unclassified regions[2] (blue lines), overlaid on the Hα image. The second to fifth columns show peaks identified by `astrodendro` overlaid on the corresponding line-ratio or velocity dispersion map. The last column indicates the [S II] flux in log scale. It is apparent that the 0.4 threshold in [S II]/Hα selects not only SNRs but also spurious regions, which in shallower imaging would not have been detected (see also Winkler et al. 2023). After accounting for the contributions of photoionized emission to our maps (see below), our region selection becomes much cleaner, and can often be more directly associated with the 'unclassified' nebular objects. At low surface brightness, most star-forming galaxies show widespread line emission arising from DIG, which makes up ∼50% of the integrated Hα emission of galaxies (Zurita, Rozas & Beckman 2000). DIG typically shows elevated levels of [S II]/Hα, [N II]/Hα and [O I]/Hα (Haffner et al. 2009), and can thus be confused for low surface brightness SNRs (e.g., Blair & Long 1997; Long et al. 2022). As shown in Belfiore et al. 2022, both the [S II]/Hα and [O I]/Hα line ratios in the DIG can be modeled by leaking radiation from H II regions, suggesting the DIG is principally powered by leakage of radiation from H II regions with a typical mean free path for the ionizing radiation of ∼2 kpc.

At high surface brightness, SNRs might be blended in projection with giant H II regions (see the third row in Fig. 2). If a SNR is seen in projection against an H II region, there is the possibility that the SNR will be outshone by the H II region, and thus be challenging to distinguish. To exclude the contribution from DIG and H II regions to the [S II]/Hα and [O I]/Hα line ratio maps, we build on the results of Belfiore et

---

[2] These regions do not have a definitive classification in Groves et al. 2023. This is principally because they are composite or shock-dominated objects in the BPT diagrams (e.g., AGN outflows, SNRs, planetary nebulae), although in some cases they simply have low S/N in one or more of the key diagnostic lines.

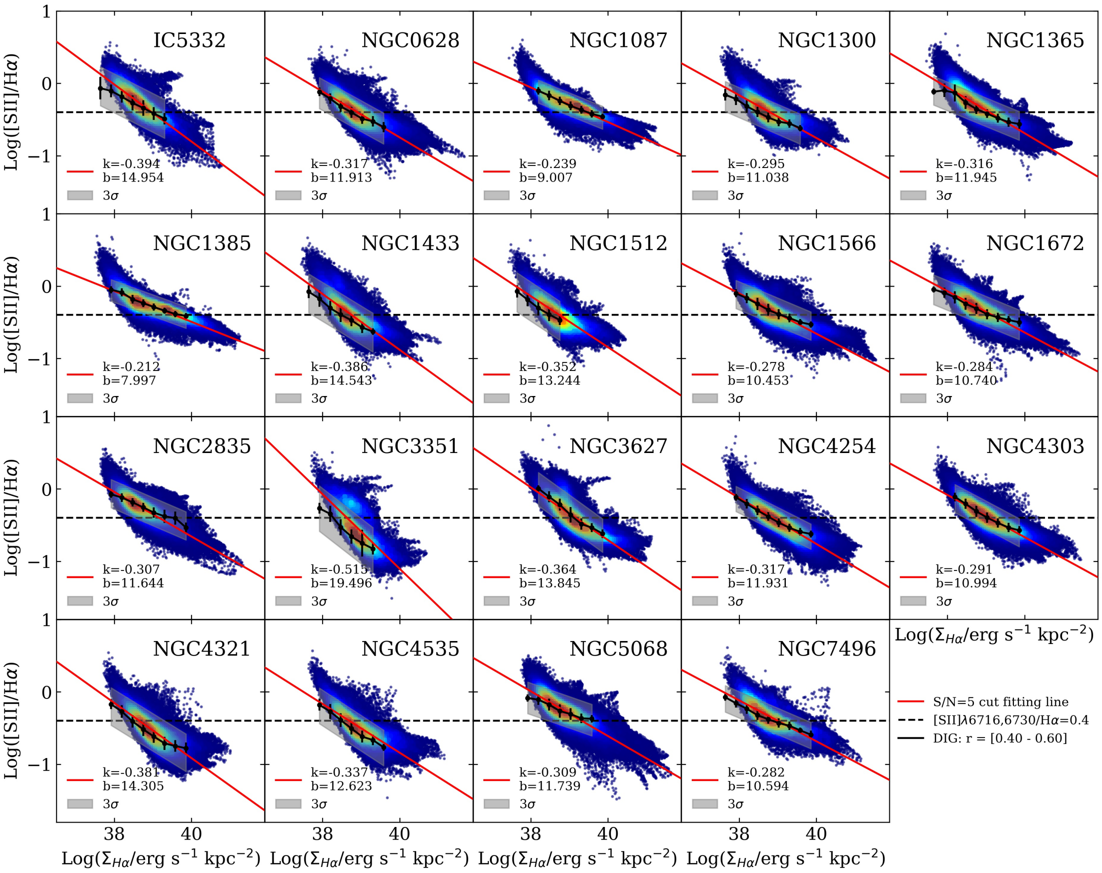

Figure 3: Log([S II]/Hα) as a function of logarithm Hα surface brightness for all pixels in each galaxy. The red solid line is the fitted correlation for each galaxy, with slope and intercept values given in the legend of each panel. The black solid line is representative of the DIG relation, as measured between 0.40 R_{max} (maximum radial coverage) and 0.60 R_{max} for each galaxy from Belfiore et al. (2022). The gray area indicates the 3σ range of this relation. SNRs typically lie above the fitted lines and show a looping structure toward the upper right. The horizontal black dashed line indicates the typical value of [S II]/Hα = 0.4 used to select SNRs. Many low Hα surface brightness pixels associated with the DIG have [S II]/Hα $\geqslant$ 0.4.

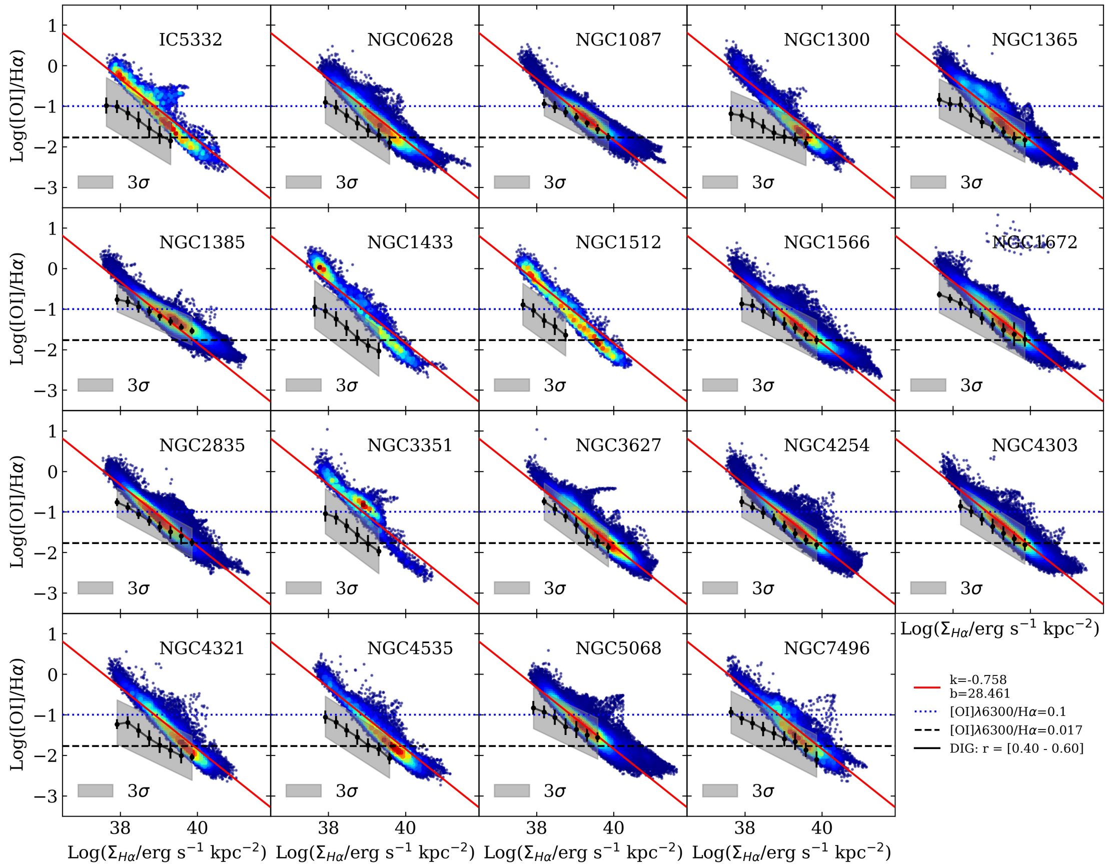

Figure 4: log([O I]/Hα) as a function of log Hα surface brightness for all pixels in all 19 galaxies. The red solid line is the fitted global correlation for all galaxies, with slope and intercept provided in the lower right corner of this plot. The black solid line is representative of the DIG relation, as measured between 0.40 R_{max} (maximum radial coverage) and 0.60 R_{max} for each galaxy from Belfiore et al. (2022). The gray area indicates the 3σ range of this relation. The black dashed line indicates the theoretical value of [O I]/Hα = 0.017 to select SNRs (Kopsacheili, Zezas & Leonidaki 2020). The horizontal blue dotted line indicates the empirical value of [O I]/Hα = 0.1 used select SNRs. For NGC 1672, the individual pixels lying above the majority come from an SNe that just happened several days before our observation.

al. 2022, who carried out a detailed characterization of DIG in the PHANGS-MUSE galaxies. Belfiore et al. (2022) spatially binned the line emission to study the faint DIG, and found strong anti-correlations between the Hα surface brightness and common diagnostic line ratios, which they show can be well fitted by photoionization models as a function of ionization parameter (in this context, a proxy for Hα intensity).

We examine the correlations between line ratio and Hα surface brightness on a pixel-by-pixel level in each of the 19 galaxies (Figs. 3 and 4), in order to search for regions exhibiting anomalously high line ratios at fixed Hα surface brightness. We expect that most pixels are dominated by photoionization, as SNRs typically only contribute ~5% of the Hα flux of an entire galaxy (Vučetić et al. 2014). Overall, we find very good agreement with the binned relations found in Belfiore et al. (2022) for the [S II]/Hα line ratios, as our data is sufficiently deep that the [S II] line is detected in a large fraction of the pixels. For the fainter [O I] line, it is apparent that we are limited by sigma-clipping at low Hα surface brightness, where [O I] is less frequently detected, and the majority of our pixels reflect $\sim 3\sigma$ outliers in the binned distribution. At high surface brightness, however, the relations agree. As is apparent in Figs. 3 and 4, we expect that in many ways our pixel-based fits are more conservative, as they generally result in steeper slopes that do not correctly model the DIG line ratios at low surface brightness. We emphasize here that as a result of our sensitivity limits, we expect that our sample is both incomplete and biased toward selecting SNR with high line ratios.

Given the observed trends, we derive linear scaling relations to characterize the expected line ratios for log [O I]/Hα (taking all galaxies jointly) and log [S II]/Hα (taking each galaxy separately) as a function of log Hα surface brightness. We used a linear regression model to fit these pixels to get a slope and an intercept, provided in Figs. 3 and 4. As we find that the [O I]/Hα versus Hα surface brightness shows uniform trends for all 19 galaxies, we fit all galaxies together, although we caution that these fits are not necessarily representative of the full DIG due to the S/N limitations on detecting [O I]. Pixels belonging to SNRs are apparent in some cases, as shown in the horizontal stripes above the fitted relation. We are generally searching for spatially coherent objects that are outliers with high line ratios, and we tailor our object selection to identify regions based on the pixel distribution and our own visual inspection.

Using these relations, we construct line-ratio residual maps as

$$\left(\frac{[\mathrm{S\,II}]}{\mathrm{H}\alpha}\right)_{\mathrm{residual}} = \log\left(\frac{[\mathrm{S\,II}]}{\mathrm{H}\alpha}\right)_{\mathrm{obs}} - \log\left(\frac{[\mathrm{S\,II}]}{\mathrm{H}\alpha}\right)_{\mathrm{fit}}, \tag{1}$$

where the subscripts `obs` denotes the observed line flux and `fit` is calculated as a function of the Hα surface brightness from the linear fit equations. $([\mathrm{O\,I}]/\mathrm{Ha})_{\mathrm{residual}}$ is calculated in a similar way.

In our residual maps, we measure the standard deviation (σ) and use `astrodendro` to identify peaks assuming a `min_value` of 2σ in $[\mathrm{S\,II}]/\mathrm{H}\alpha_{\mathrm{residual}}$ and 1σ in $[\mathrm{O\,I}]/\mathrm{H}\alpha_{\mathrm{residual}}$. `min_delta` is set to 0.1 dex to avoid selecting the second maximum peak that is close to the highest peak. We chose these thresholds to guarantee we did not miss objects (as judged by visual inspection). We identify 880 objects selected from the [S II]/Hα line ratio residual, and 1368 objects selected from the [O I]/Hα line ratio residual.

To judge the impact of any sigma-clipping bias at low Hα surface brightness, which principally affects the [O I]/Hα line ratios, we repeated this analysis using the fit and σ determined from the DIG binned data, and identifying 3σ pixel-scale outliers. This resulted in a very similar number of objects selected by their [S II]/Hα residuals, and only slightly fewer objects selected by their [O I]/Hα residuals, indicating that our fine-tuning of the `astrodendro` parameter `min_value` results in a roughly equivalent selection of objects.

2.3.1.2 *Selection via velocity dispersion maps*

As mentioned earlier, the spectral resolution of our MUSE data also enables the selection of SNRs from broadened emission lines in their spectra. In particular, we use the velocity dispersion of the [S II] line, corrected for instrumental broadening, to select our SNRs. We note that the kinematics of [S II]λ6716 has been tied in the fit with other low-ionization lines to further improve the reliability of the measurement; however, all of these (e.g., [S II]λ6730, [N II]$\lambda\lambda$6548,84, [O I]$\lambda\lambda$6300,64; see Emsellem et al. 2022) should be strongly associated with shocks. While the Hα velocity dispersion can, in principle, be utilized, we find that the [S II] line kinematics can be more directly and uniquely associated with SNR shocks. On average, the line kinematics typically agree between both tracers within 5 km s^{-1}.

An S/N cut of 20 for [S II]λ6716 is applied to ensure errors in the measured velocity dispersion remain below 10% when deconvolved from the ~50 km s^{-1} instrumental velocity dispersion (Bacon et al. 2017; Egorov et al. 2023). With smoothing and binning, higher S/N is achieved across the map, but SNRs become blended with H II regions and DIG, and it is thus more challenging to identify by their kinematic signatures. At low S/N, DIG might be hard to distinguish kinematically from SNRs, as it also produces broadened line emission due to its turbulent nature and increased scale height (Haffner et al. 2009; Levy et al. 2019). After masking galaxy centers, we do not see evidence that we are biased toward selecting DIG emission with this method as our S/N cut on [S II] has effectively masked most of the DIG; however, with sufficiently deep data it remains challenging to distinguish these components (Winkler et al. 2023).

We take a conservative approach and set our `astrodendro` threshold to select peaks with velocity dispersion larger than 50 km s^{-1} (full width at half maximum (FWHM) = 118 km s^{-1}) for our parent sample. We visually tested different thresholds and then chose this value that optimized the number of detected SNR candidates without including too many spurious detections. A `min_delta` of 10 km s^{-1} is used to make sure local peaks are identified properly. A total of 352 objects are identified using this technique.

2.3.1.3 *Selection via BPT distances*

In addition to the aforementioned criteria of [S II], [O I] and velocity dispersion that are traditionally used for selecting SNRs, we also explore the properties, and the potential for selecting SNRs using BPT diagrams, widely used to assess the line emission mechanism in galaxies (Baldwin et al. 1981; Veilleux & Osterbrock 1987). Here we did not consider the [O III]/Hβ versus [N II]/Hα diagram as [N II]/Hα varies more with metallicity (see Sect. 3.3). On the ~100 pc scale of an individual nebula (top row of Fig. 5), regions that are dominated by shock heating lie above the extreme starburst line (Kewley et al. 2001), while regions dominated by photoionization from OB stars lie below this line (Congiu et al. 2023). These diagrams make use of the same [S II]/Hα and [O I]/Hα line ratios as we describe in Sect. 2.3.1.1; however, from the shape of the extreme starburst line it is apparent that a single fixed threshold may not be appropriate in all physical conditions.

For this reason, we select pixels as shock-heated versus photoionized based on their distances from the extreme starburst line in the [O III]/Hβ versus [O I]/Hα and [O III]/Hβ versus [S II]/Hα BPT diagrams (Kewley et al. 2006), as shown in Fig. 5. Here "distance" refers to the Euclidean distance (square root of the sum of vertical and horizontal separation squared) to the closest point on the extreme starburst line in both BPT diagrams. While the DIG also populates a similar parameter space in such diagrams (Zhang et al. 2017), the [O III] emission is particularly faint and is effectively excluded with our S/N>5 cut.

We construct maps of these two BPT distances, and run `astrodendro` on each, with a `min_delta` of 0.05 dex to avoid selecting the local maxima. We use a minimum distance of ± 0.2 dex to classify pixels as shocks (positive distance) versus photoionized (negative distance), where the chosen threshold of 0.2 is roughly the 3σ uncertainty in the ratios measured for all pixels with $S/N \geqslant 5$. Figure 5 (bottom row) shows the integrated line ratios for all objects in our final catalog. SNRs do preferentially populate the shock-heated regime, and those SNRs found to be populating the photionized regime have typically been selected via one of our other criteria, or are blended with H II regions(see Sect. 2.5.3). A total of 635 objects are identified using the BPT distance in the [O III]/Hβ versus [O I]/Hα diagram, and a total of 372 objects are identified using the BPT distance in the [O III]/Hβ versus [S II]/Hα diagram.

2.3.1.4 *Final parent sample construction and integrated line flux measurements*

We employ five criteria to select objects, and using the central coordinates determined through `astrodendro`, we perform a crossmatch within a 1" radius across all objects. This process yields a `parent sample` consisting of 2233 objects selected by at least one of our criteria. In cases where the `astrodendro` centers differ across the five maps, we adopt the center of the first criterion that identified the object as an SNR or SNR candidate (following the order in which we present the criteria in this paper). A sum-

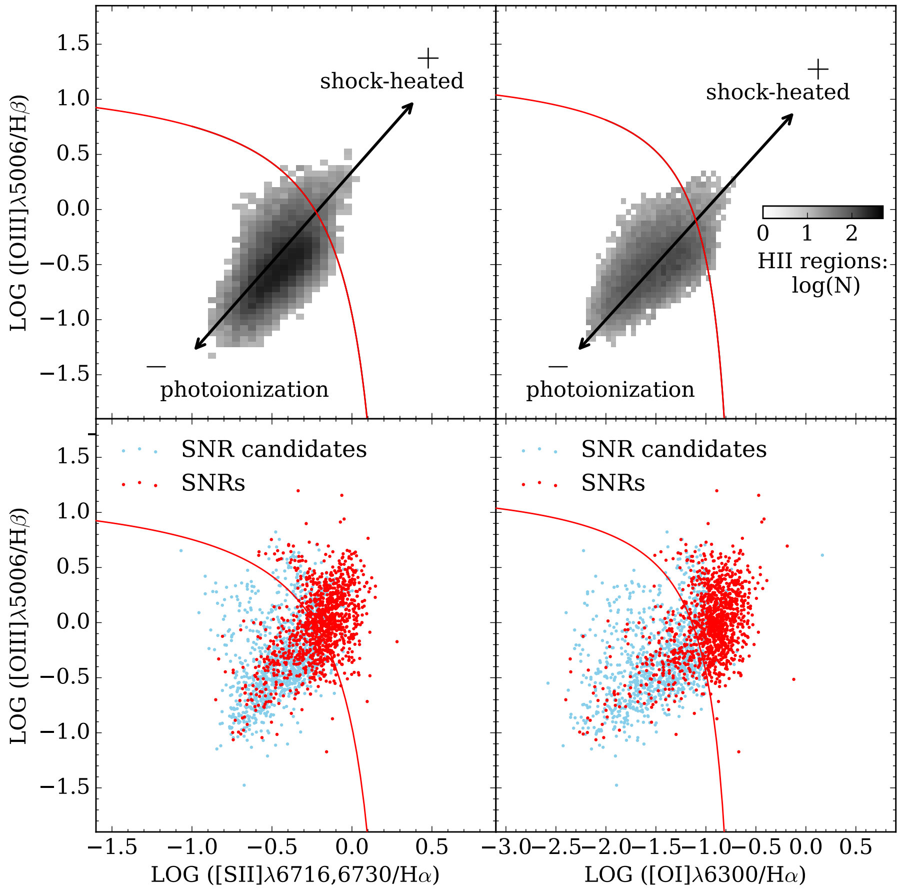

Figure 5: BPT diagrams with demarcation line from Kewley et al. (2006) with an indication of BPT distances as defined as the distance to the red solid extreme starburst lines. The plus sign (+) indicates positive distance where shock-heating dominates, while the minus sign (–) indicates negative distance where photoionization dominates. The top left and top right plots show the distribution density of nebular regions in these 19 galaxies (Groves et al. 2023). In the bottom left and bottom right plots, SNRs and SNR candidates are indicated by red and blue dots, respectively. Nebular regions tend to occupy the photoionized region, while SNRs are concentrated in the shocked areas.

mary of how these different criteria each contribute to the total sample is presented in Sect.2.3.2 and revisited in Sect. 2.5.2.

Figure 6 shows a map of the parent sample identified within NGC 628 using each criterion, and Fig. 7 shows a zoomed-in SNR of NGC 628, demonstrating the distinct range of values of each criterion at the SNR location compared to the surrounding region. For all 19 PHANGS-MUSE galaxies, the locations of 2233 objects in the parent sample are shown in Fig. 9 and Appendix A.2. We find on average 118 objects per galaxy, which are located throughout the disks of each galaxy.

For this parent sample we measure line fluxes, velocities, and velocity dispersions from the integrated spectra of these objects (see Table A.2 in Appendix A.3) using the PHANGS-MUSE data analysis pipeline or DAP (described in Emsellem et al. 2022). We expect most SNRs will not be not resolved in our galaxies, so we use a fixed radius of 50 pc for all objects, comparable to or slightly larger than the PSF in all galaxies, and measure emission-line fluxes and kinematics integrated over this area (see Emsellem et al. 2022 and Groves et al. 2023 for more details on how emission-line fluxes and gas dynamics are measured using the DAP).

It is important to note a caveat in the interpretation of these emission-line fluxes. The integrated line flux ratios [S II]/Hα and [O I]/Hα that we measure from the integrated spectra here are different from the [S II]/Hα and [O I]/Hα residual maps that we use to identify objects in Sect. 2.3.1.1. While we use `astrodendro` to identify SNRs from line flux ratios residual maps, when running the DAP we are unable to apply such a correction. Corrections for background photoionized emission have not been extensively undertaken in previous research, so we believe the line measurements in our catalog are directly comparable to literature results. We emphasize that these line fluxes may be biased by the DIG background, or any H II region they overlap with. However, disentangling these background effects is challenging as they do not exhibit a smooth morphology. As can be seen in Fig 2, when the identified object overlaps with a H II region, the [S II]/Hα ratio is less distinct from the environment; however, after our photoionization correction, the [S II]/Hα ratio becomes more prominent. Hereafter, line fluxes for our SNRs and SNR candidates all refer to integrated flux without background subtraction.

2.3.2 *Parent sample classification*

Table 2: Number of identified SNRs and SNR candidates in 19 galaxies.

Sample	number	[O I]/Hα residual	[S II]/Hα residual	σ([S II]λ6716)	BPT distance ([O I]-[O III])	[S II]-[O III]
parent sample	2233	1368	880	352	635	372
SNRs	1166	658	727	255	569	325
– isolated	964	464	549	189	543	322
– blended	202	194	178	66	26	3
SNR candidates	1067	710	153	97	66	47
– isolated	498	226	86	80	65	46
– blended	569	484	67	17	1	1

Notes. The columns from left to right are the category of SNR sample, sample size, and the number of SNRs satisfying each of our five criteria: [O I]/Hα, [S II]/Hα, [S II] velocity dispersion, and BPT distance as defined in the [O III]/Hβ versus [O I]/Hα diagram and in the [O III]/Hβ versus [S II]/Hα diagram.

We have used five criteria in Sect. 2.3.1 to identify objects for our parent sample. While the [S II]/Hα line ratio has most commonly been used in the literature to identify SNRs (e.g., Long et al. 2022), all of the diagnostics we employ are valid indicators of SNR shocks. To increase our confidence in our identification of these objects as true SNRs, we consider how to combine our different criteria and the integrated line fluxes to identify a robust subsample of objects that we can classify as SNRs.

Table 2 presents a breakdown of how many objects are identified by each criterion. We identify the largest number of objects using the [O I]/Hα line ratio maps (1368), and the smallest number of objects using the [S II]λ6716 velocity dispersion (352). Among our five criteria, 1476 objects were only selected by only one criterion, 757 objects were selected by at least two criteria, 365 objects were selected by at least three criteria, 184 objects were selected by at least four criteria and 68 objects were selected by all five criteria. Given the range of characteristics apparent in our parent sample, we investigate using different pairs of criteria, as this provides a secondary confirmation of our SNR classification. Figure 8 (left) presents a visualization of what fraction of objects are matched pairwise between the five criteria. Clearly, the [O I]/Hα residual and [S II]/Hα residuals produce the most overlap (~20% of the parent sample), but are still not perfectly in agreement, and also show non-negligible ~10% overlap with the remaining indicators. We also note that a large number of objects (414) do not match between any two criteria, but exhibit high line ratios in their integrated line fluxes ([O I]/Hα>0.1 and [S II]/Hα>0.4), such that in previous work, they would have resulted in clear SNR classifications.

Based on this analysis of the 2233 objects from our parent sample, we define two subsamples. The "SNR candidates" are those objects only selected by one criterion, and either [S II]/Hα<0.4 or [O I]/Hα<0.1. The rest of the objects we classify as "SNRs", which means that at least two of the five methods identify the object, or both the integrated [S II]/Hα and [O I]/Hα are high enough that the line emission is best explained by shock excitation. Figure 8 (right) presents a visualization of how objects are matched pairwise for just the SNR sample. [O I]/Hα residual and [S II]/Hα residuals select about half of the objects, but other pairs of diagnostics are also contributing significantly (10-20%) to the SNR sample.

We present spectra for four representative SNRs and one typical H II region in Fig. 10 in order to show the typical sensitivity and spectral features that we observe. In all panels, the strong sky lines at 6300Å and 6363Å are masked. The top two panels show the spectra for two SNRs with high [S II]/Hα $>$ 0.8, the middle two panels for two SNRs with high-velocity dispersion > 80 km s^{-1}, and the bottom panel for a representative H II region. The broadened emission lines are apparent by eye for the two high-velocity dispersion SNRs compared to the H II region, as is the increased [S II]/Hα ratio in the top two SNRs.

For the SNRs and SNR candidates, when we place them in the [O I]/Hα v.s [S II]/Hα parameter space, we can clearly see that (by design) the majority of SNRs lie above

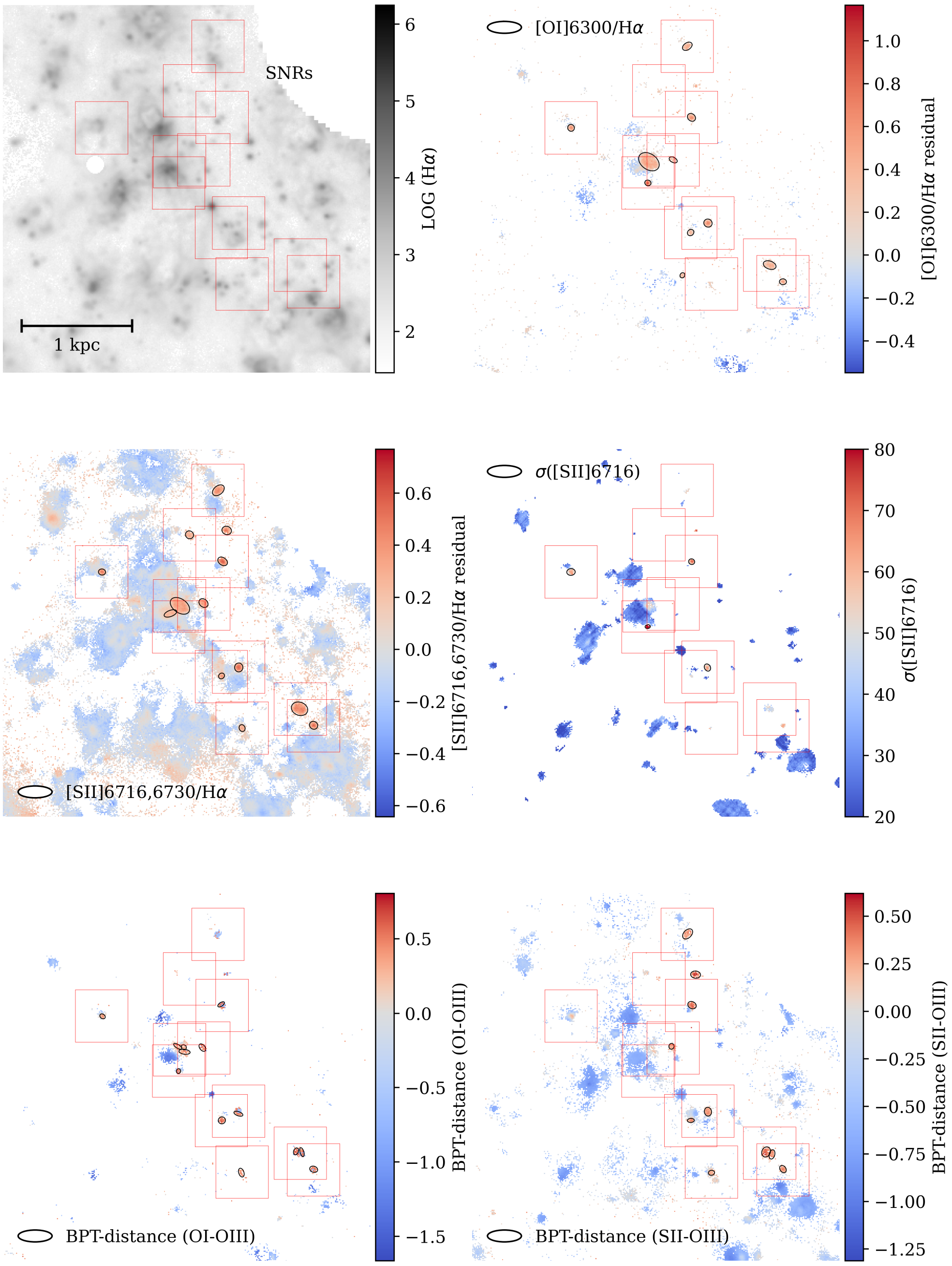
SNRs
1 kpc
LOG (Hα)
6
5
4
3
2
[OI]6300/Hα
[OI]6300/Hα residual
1.0
0.8
0.6
0.4
0.2
0.0
−0.2
−0.4
[SII]6716,6730/Hα
[SII]6716,6730/Hα residual
0.6
0.4
0.2
0.0
−0.2
−0.4
−0.6
σ([SII]6716)
80
70
60
50
40
30
20
BPT-distance (OI-OIII)
0.5
0.0
−0.5
−1.0
−1.5
BPT-distance (SII-OIII)
0.50
0.25
0.00
−0.25
−0.50
−0.75
−1.00
−1.25

Figure 6: Zoomed-in map (3 kpc × 3 kpc) of the SNR population recovered in one of the galaxies in our sample, NGC 628, using our five selection criteria (described in Sect. 2.3). Panels from top left to bottom right show the log Hα emission, [O I]/Hα residual map, [S II]/Hα residual map, [S II]λ6716 velocity dispersion, BPT distance (OI-OIII) map, and the BPT distance (SII-OIII) map. Objects selected by each individual criterion are marked with black ellipses in the corresponding subplot and the locations of objects classified as SNR are marked with red boxes. Pixels with low S/N (⩽5), and those corresponding to stellar sources, and the central region of the galaxy, have been masked (see text for details).

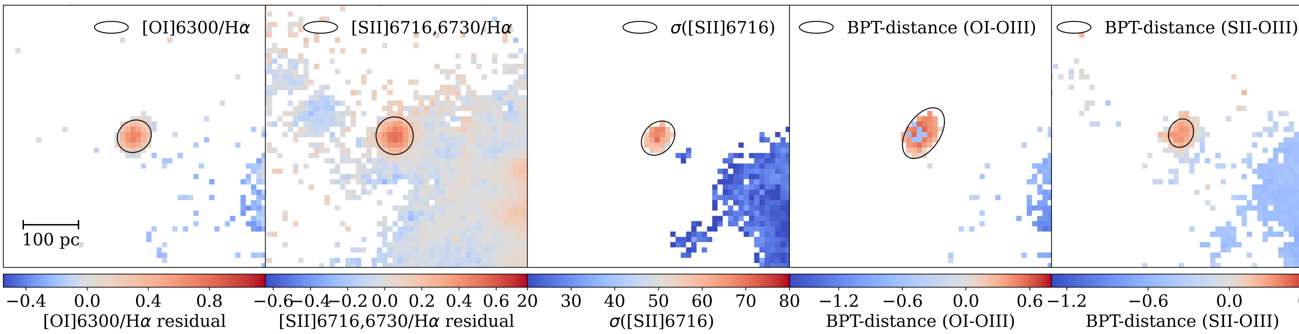
[OI]6300/Hα
[SII]6716,6730/Hα
σ([SII]6716)
BPT-distance (OI-OIII)
BPT-distance (SII-OIII)
100 pc
−0.4 0.0 0.4 0.8
[OI]6300/Hα residual
−0.6 −0.4 −0.2 0.0 0.2 0.4 0.6
[SII]6716,6730/Hα residual
20 30 40 50 60 70 80
σ([SII]6716)
−1.2 −0.6 0.0 0.6
BPT-distance (OI-OIII)
−1.2 −0.6 0.0
BPT-distance (SII-OIII)

Figure 7: Example of what one SNR (in NGC 628) looks like when using the five criteria. This SNR is selected in the [O I]/Hα residual map, [S II]/Hα residual map, [S II]λ6716 velocity dispersion, BPT distance (OI-OIII), and BPT distance (SII-OIII) maps. The selection is marked with a black ellipse.

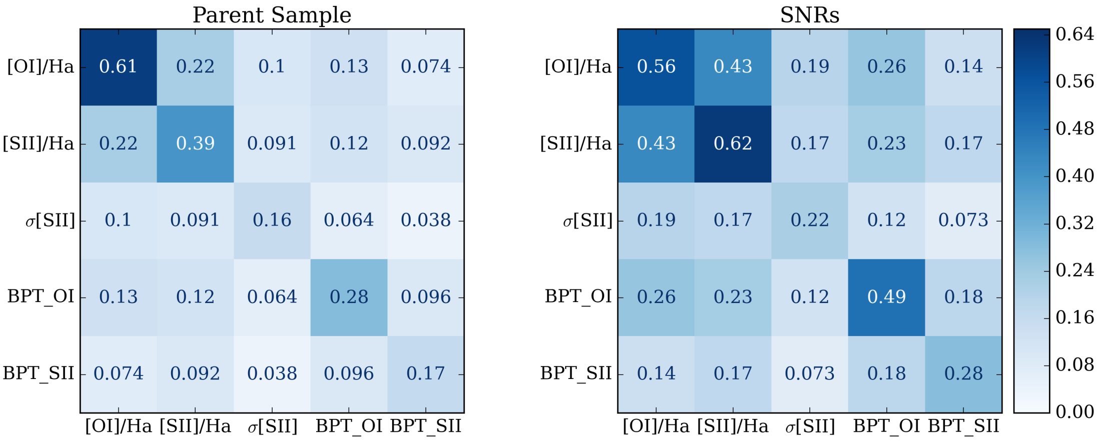
Parent Sample

	[OI]/Ha	[SII]/Ha	σ[SII]	BPT_OI	BPT_SII
[OI]/Ha	0.61	0.22	0.1	0.13	0.074
[SII]/Ha	0.22	0.39	0.091	0.12	0.092
σ[SII]	0.1	0.091	0.16	0.064	0.038
BPT_OI	0.13	0.12	0.064	0.28	0.096
BPT_SII	0.074	0.092	0.038	0.096	0.17

SNRs

	[OI]/Ha	[SII]/Ha	σ[SII]	BPT_OI	BPT_SII
[OI]/Ha	0.56	0.43	0.19	0.26	0.14
[SII]/Ha	0.43	0.62	0.17	0.23	0.17
σ[SII]	0.19	0.17	0.22	0.12	0.073
BPT_OI	0.26	0.23	0.12	0.49	0.18
BPT_SII	0.14	0.17	0.073	0.18	0.28

Figure 8: Fraction of objects in the parent sample (left) and SNR sample (right) that are identified by specific pairwise combination of our five criteria ([O I]/Hα residual, [S II]/Hα residual, [S II]λ6716 velocity dispersion, BPT distance (OI-OIII), and BPT distance (SII-OIII).

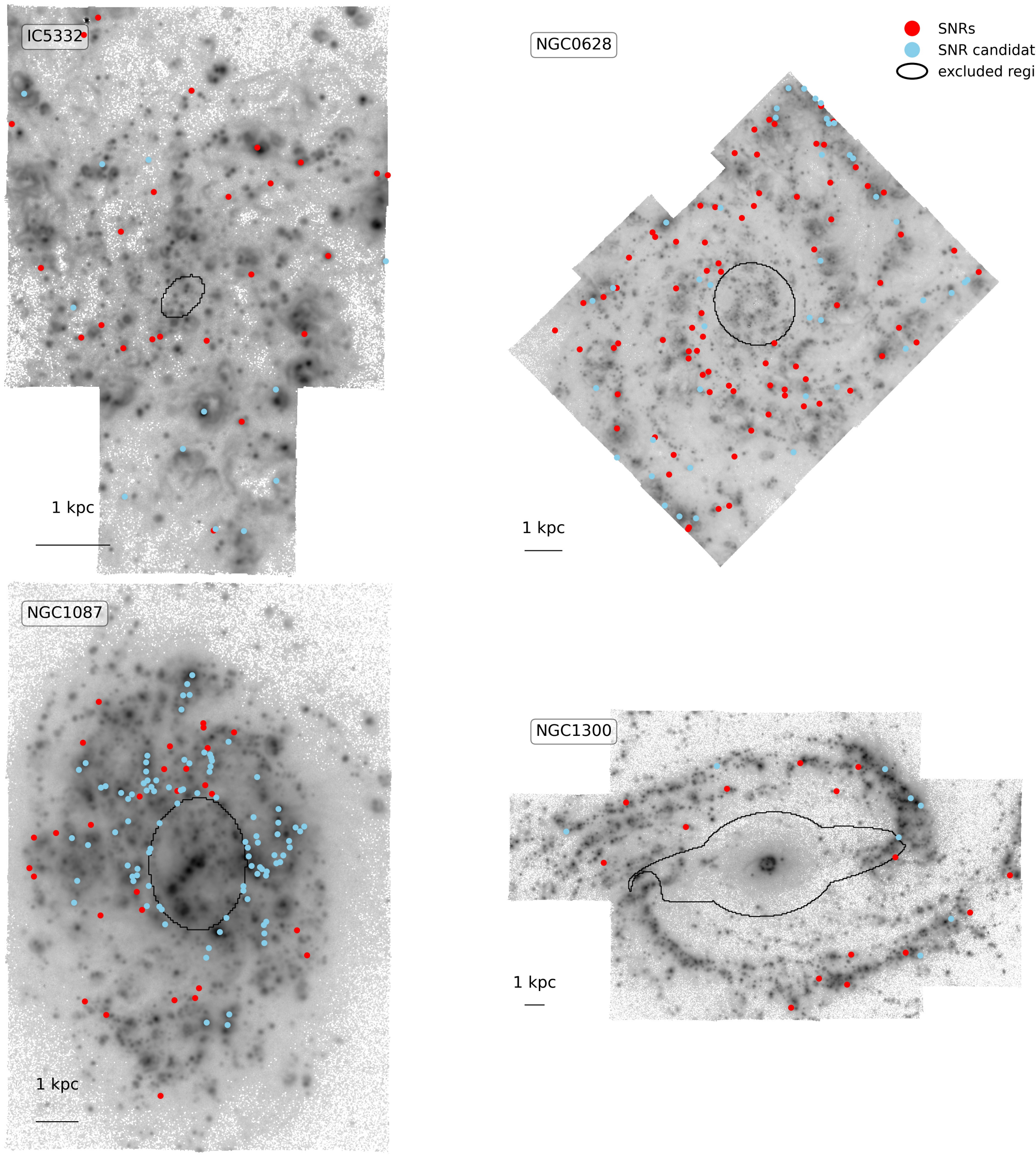
IC5332
NGC0628
SNRs
SNR candidates
excluded region
1 kpc
1 kpc
NGC1087
NGC1300
1 kpc
1 kpc

Figure 9: Parent sample of 2233 objects identified across the 19 PHANGS-MUSE galaxies, compared to the Hα emission. The galaxy name is in the upper left corner. SNRs are indicated by red dots while SNR candidates are in blue. The background shows the Hα map. Regions excluded from our search are outlined in solid black. Most galaxies have the center masked (see Appendix A.1 for more details). We observe SNRs to be distributed across the full field of view, and good qualitative correspondence with Hα bright sites of star formation (see Appendix A.2 for the rest of the galaxies).

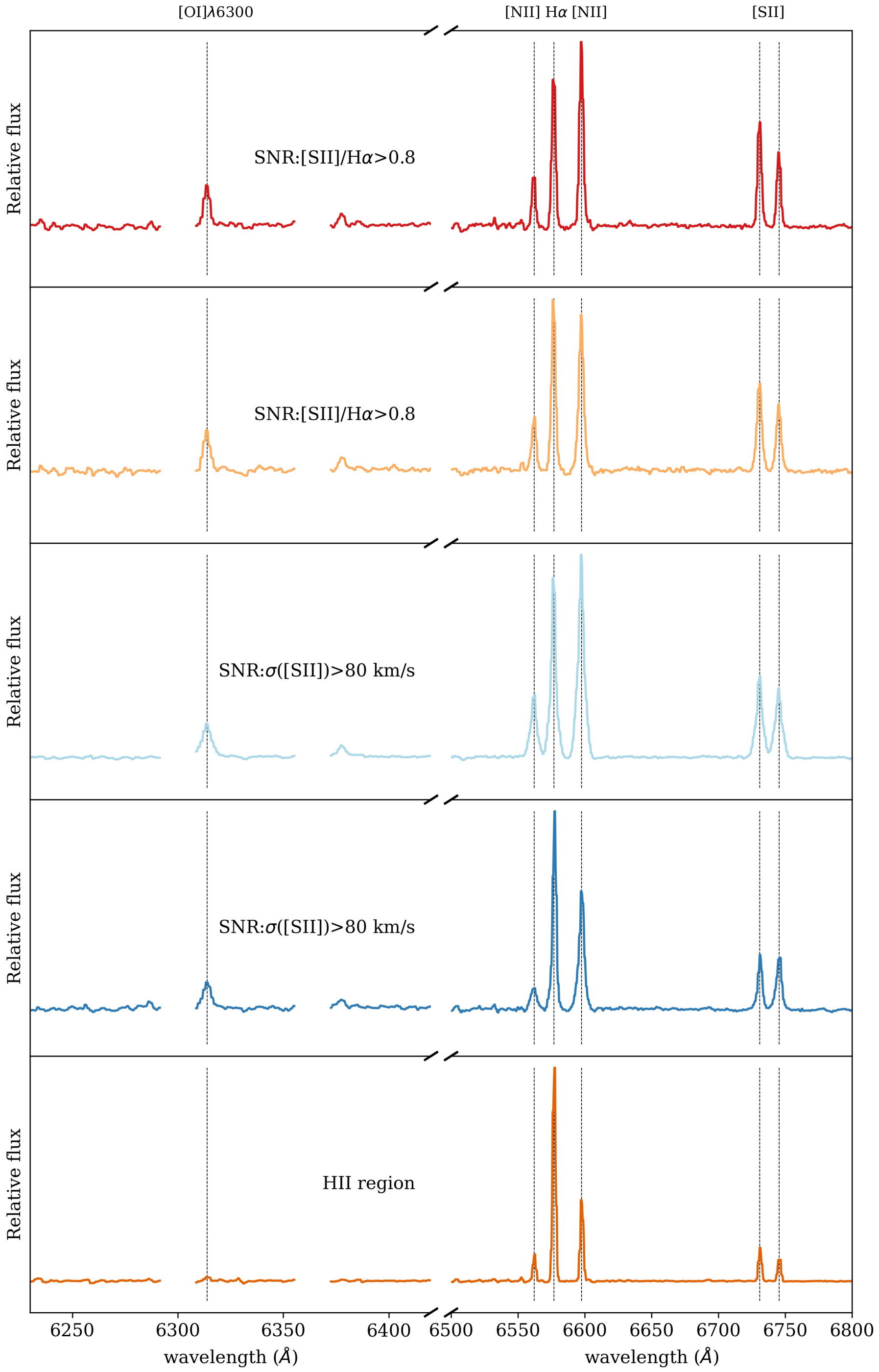

Figure 10: Spectra for four SNRs and an H II region in NGC 628. Top two: SNRs with high [S II]/Hα value > 0.8; middle two: SNRs with high-velocity dispersion > 80 km s^{-1}; bottom one: H II region. Characteristic lines, e.g., [O I], [S II], [N II], and Hα are labeled in the plot. All SNRs have broader emission lines than the H II region, though this is most apparent in the two SNRs (NGC0628_17 and NGC0628_48) as they were selected to have particularly broad lines. The sky emission at [O I]λ6300Å, λ6363Å has been masked.

[O I]/Hα>0.1 and [S II]/Hα>0.4 (see Fig. 11a) while the SNR candidates distribution overlaps with the H II regions (see Fig. 11b) making it difficult to distinguish SNR candidates from H II regions. The distinct boundary at 0.1 for [O I]/Hα in H II regions arises from the definition of these objects in Groves et al. (2023) using BPT diagram cuts.

Table 3: Parent sample catalog generated in this work (see text for details). Notes. (*) Measured emission lines are in Table A.2 in Appendix A.3.

Column Name	Unit	Description
`Index`	–	Global SNR ID
`gal_name`	–	Galaxy name
`sample_name`	SNRs/SNR candidates	Classification of parent sample
`gal_dist`	Mpc	galaxy distance
`snr_dist`	arcsecond	deprojected distance to the galaxy center
`r_over_reff`	–	ratio of distance to the effective radius of the galaxy
`environment`	–	environment mask
`Ha6562_lumi`	$\mathrm{erg\ s^{-1}}$	Hα luminosity, has been corrected for Milky Way foreground extinction
`ID`	–	local SNR ID
`match`	–	numbers of matched criteria
`OI`	boolean	whether identified in [O I]/Hα residual map
`SII`	boolean	whether identified in [S II]/Hα residual map
`SII_sigma`	boolean	whether identified in [S II] velocity dispersion map
`BPT_OI`	boolean	whether identified in [O I] BPT distance map
`BPT_SII`	boolean	whether identified in [S II] BPT distance map
`SII_Ha`	ratio	the value of [S II]/Hα
`iso_flag`	boolean	blended is False, isolated is True
`region_ID`	number	if blended, ID of HII region object is blended with
`RA`	degree	right ascension coordinate
`DEC`	degree	declination coordinate
`Emission*_FLUX`	$10^{-20}\mathrm{cm^{-2}erg\,s^{-1}}$	emission-line flux, has been corrected for Milky Way foreground extinction
`Emission_FLUX_ERR`	$10^{-20}\mathrm{cm^{-2}erg\,s^{-1}}$	emission-line flux error
`Emission_VEL`	$\mathrm{km\,s^{-1}}$	emission-line velocity
`Emission_VEL_ERR`	$\mathrm{km\,s^{-1}}$	emission-line velocity error
`Emission_SIGMA`	$\mathrm{km\,s^{-1}}$	emission-line velocity dispersion
`Emission_SIGMA_ERR`	$\mathrm{km\,s^{-1}}$	emission-line velocity dispersion error

Using the region footprints identified by Groves et al. 2023, we measure how many of the objects in our parent sample fall in projection on top of nebulae. In total, ~35% of our objects overlap with nebulae classified as H II regions. ~30% overlap with unclassified nebulae (typically labeled 'unclassified' as they are found to be inconsistent with photoionization based on diagnostic line ratios), indicating that these objects are likely also identifiable by their Hα morphology. The remaining ~35% of the parent sample is not included in the nebular catalog at all, and half of these are classified as SNRs, indicating how many objects would be missed if only line flux intensity is used for object selection. Within our catalog, we label those objects that overlap with H II regions as 'blended', while those that do not overlap (or overlap with unclassified regions in the Nebular catalog) we identify as 'isolated'.

We provide integrated properties for all objects in our parent sample as a machine readable catalog with the list of columns provided in Table 3. The catalog includes the host galaxy name and distance, object classification, object distance to the galaxy center in units of effective radius, environment mask that SNR lies on, coordinates, which criterion selected the object, emission-line fluxes, gas kinematics, isolated flag, [S II]/Hα value, and Hα luminosity.

2.3.3 *Validation of methods: Comparison with supernova remnants in M83*

Our SNR identification method differs somewhat from past SNR searches in nearby galaxies, which were done using visual identification of Hα bright sources that exhibit high [S II]/Hα line ratios. In addition to our automated source detection, we also differ by using line-ratio "residual" maps to account for diffuse emission, and make use of multiple optical line diagnostics for selection, including the kinematics (from the velocity dispersion maps) of our sources.

To test how well our identification method can recover SNRs, we apply our technique to the well-studied SNR population in M83. This galaxy has an extensive MUSE mosaic (Della Bruna et al. 2022) and is well matched to our sample in terms of stellar mass, star formation rate, and morphology, but is closer in distance (4.61 Mpc; Saha et al. 2006) and thus reaches significantly higher physical resolution (~20 pc). M83 is one of the best-studied galaxies in terms of its SNR population, with a total of 366 SNRs identified using a combination of X-ray, IR and optical data (Blair et al. 2014; Blair, Winkler & Long 2012; Dopita et al. 2010; Long et al. 2014; Williams et al. 2019), including recent work that used MUSE data to expand the SNR catalog (Long et al. 2022) (L22 hereafter).

The comparison between the objects we detect and the SNRs in the L22 catalog is visualized in Fig. 12. After masking the galaxy center, we identify a parent sample of 125 objects that satisfy at least one of our five criteria (see Appendix A.4 for a complete table). Within the MUSE footprint (excluding the center), L22 identifies 188 SNRs and we recovered 96 of these (51%). If we adjust our threshold for selecting sources in the

[S II]/Hα residual map then we can recover more of the known SNRs, but introduce a lot (>200) of additional SNR candidates that are not in the L22 catalog and may just be spurious detections or dynamically induced shock networks in the ISM. In all, 96 out of 125 (76.8%) of our parent sample correspond to known SNRs.

Statistically, the unrecovered 92 objects have lower median Hα surface brightness and [S II]/Hα than the recovered 96 ones, which makes their identification difficult using our method. In addition, the SNRs listed in L22 include 16 SNRs selected using methods other than optical lines (e.g., X-ray and [Fe II]1.644μm). We do not expect to detect these objects in the optical, and do not recover any of them.

If we construct a SNR sample in M83, consisting of objects that satisfy at least two criteria using our methods, then 58 SNRs are identified. All of them are also identified as SNRs in L22. This demonstrates that our method can recover SNRs with high confidence by leveraging multiple-line diagnostics.

The 67 objects in the parent sample that are identified using only one method make up our SNR candidate sample. 57% of these are contained in L22. This suggests that we can generally consider many of these SNR candidates to be true SNRs. Of the objects not in the L22 catalog, based on visual inspection some look like reasonable SNR candidates, while others do not. For example, we identify a cluster of regions to the north-east of the galaxy center, along the bar and close to the bar-end, none of which exist in the literature catalogs and may instead be due to shocks associated with the bar dynamics.

This comparison demonstrates that overall our technique produces a reliable SNR catalog. Even our SNR candidates are often correctly identifying SNRs. By applying an automated peak-finding algorithm, we save time by not having to carry out a visual inspection and have a reproducible, homogeneous selection. However, the choices we have made in how we identify objects and construct our SNR catalog clearly do not produce a complete catalog and are also biased toward selecting only 'typical' SNRs. We do not recover the very young SNR in M83 identified by Blair et al. 2014, although it could in principle be identified by its broadened [S II] lines. However, it is so compact (1 pc in diameter), that when blended at 100 pc scales with neighboring H II regions it is no longer selected by its kinematic signatures, and we expect such young objects are systematically missed in our catalog.

2.4 RESULTS

2.4.1 *Comparison with* H II *regions*

We compare the integrated emission-line properties of our sample of SNRs with H II regions identified in Groves et al. (2023). As we can see in the comparison in Fig. 13, SNRs have higher [O I]/Hα and [S II]/Hα ratios than H II regions at the same Hα luminosity. These ratios decrease with increasing Hα luminosity. This reflects our selection biases, as a faint SNR blended with a brighter H II region will no longer exhibit the distinctive line ratios and line kinematics that we select for with our methods. This can be seen directly, as SNRs appearing in projection with H II regions (light red circles in the figure) have higher Hα luminosities and correspondingly lower [O I]/Hα and [S II]/Hα ratios.

In Fig. 14a, we see a concentration of both SNRs and H II regions at small r_{eff}. This is expected as both closely follow the star formation rate distribution (Cronin et al. 2021), which is more concentrated in the inner regions of galaxies (Leroy et al. 2021). We find hints of radial trends in the SNR line ratios, with higher line ratios found in SNRs compared to H II regions at all radii, and higher values of [S II]/Hα in SNRs at smaller radii. Generally, the [S II] line is brighter for higher shock velocities (Allen et al. 2008). Since SNR shocks typically slow down over time, this is indicative of a larger population of younger SNRs. Given the overall larger number of SNRs at small radii, this likely simply reflects the higher probability of detecting these younger SNRs, although higher ambient densities around SNRs at smaller galactic radii could also be playing a role.

We also find similar trends in the metallicity-sensitive [N II]λ6583/Hα line ratio with radius (Fig. 14b). In most previous SNR surveys that have relied on narrowband imaging, the [N II]λ6583 lines often ended up convolved within the Hα filter and not studied separately; however, with MUSE we can cleanly separate the [N II]λ6583 and Hαλ6562 lines. The higher line ratios at smaller radii could be a consequence of higher ISM metallicities (Kreckel et al. 2019; Pessa et al. 2021).

In Figs. 15a and 15b, we compare the velocity dispersion (corrected for instrumental broadening) of the Hα line and the [S II]λ6716/[S II]λ6730 emission-line ratio, which is a density-sensitive diagnostic[3]. We can clearly see that while H II regions are concentrated at low-velocity dispersions of 30-40 $\mathrm{km\,s^{-1}}$, SNRs can have velocity dispersions that reach more than 100 $\mathrm{km\,s^{-1}}$, owing to the presence of higher-velocity shocked material in the SNRs. Velocity dispersion is also one criterion that we used in Sect. 2.3.1.2 to identify SNRs. Regarding ambient densities, most of the SNRs have line ratios consistent at the 3σ level with the low-density limit (~10-100 $\mathrm{cm^{-3}}$), with only ~15% of regions showing ratios corresponding to significantly higher densities (>100 $\mathrm{cm^{-3}}$). A similar distribution of values has also been seen in the SNRs of nearby galaxies (e.g., Long et al. 2018, 2022). No visible trend exists between the [S II] doublet ratio and the velocity dispersion of the SNRs.

Figure 15b shows the power of combining velocity dispersion and [S II]/Hα ratio together to distinguish SNRs from H II regions. Our SNRs populate a region of parameter space that has both high-velocity dispersions and high [S II]/Hα values. The distinction is clearer in this regime; however, it becomes complicated when SNRs overlap with H II regions as indicated by light red circles in the figure.

---

[3] More specifically, the ratio traces the electron density in the post-shock [S II] recombination zone, and is proportional to the preshock density (Dopita et al. 2016).

We compare our observed SNRs with the MAPPINGS (Allen et al. 2008) model in Fig. 16. Different grids show different ISM metallicities. Here we adapted the Dopita et al. (2005) abundance model as opposed to the default solar models. Each grid samples a range of shock velocities and magnetic field strengths (0~10 μG). We see that our SNRs are consistent with grids sampling between Large Magellanic Cloud (LMC) (half solar metallicity) and twice solar metallicities (as defined in MAPPINGS model). This is an important validation of our selection process, that we are indeed primarily picking objects that are consistent with the expected parameter space of shocks (Long et al. 2022). This is consistent with the range of metallicities observed in the H II regions detected in these galaxies (Groves et al. 2023).

2.4.2 *Comparison with the literature: Supernova remnants in other galaxies*

In order to further validate our selected SNR population in the 19 MUSE galaxies, we compare their optical line emission properties with the well-studied SNR populations in four nearby galaxies – M33 (Long et al. 2018), M51 (Winkler et al. 2021), M83 (Long et al. 2022), and NGC 6946 (Long et al. 2019). The SNR populations in these galaxies have been vetted not only with optical spectroscopy, but also multiwavelength information from radio, X-ray, and in some cases near-IR lines (e.g., [Fe II]1.64 μm in M83).

In the process of identifying SNRs, a selection bias may exist in more distant galaxies, as we are prone to selecting more luminous SNRs. These could be bright either because they are young or because the explosion happens in a dense environment. At larger distances (and lower physical resolution) we are also more likely to miss SNRs, as they can be blended with brighter H II regions.

We note that within our sample, there is a set of SNRs that exhibit very high Hα luminosities ($\geqslant 10^{38}$ erg s^{-1}) and relatively low [S II]/Hα ratios ($\leqslant 0.4$). In many respects, these characteristics more strongly resemble H II regions than SNRs; however, as they are selected by multiple criteria we remain confident in their classification as SNRs. We see that these SNRs are almost all identified as blended with H II regions in our sample. If we exclude these, we identify very few SNRs with Hα luminosities above $10^{37.5}$ erg s^{-1}.

In Fig. 17, we compare the line ratios [S II]/Hα and [N II]/Hα of the SNRs in our PHANGS-MUSE galaxies and the four nearby galaxies. Similar to Fig. 16, we find that our SNRs show a range of values of different line diagnostics that are also observed in SNR surveys of more nearby well-studied galaxies. All four galaxies exhibit a similar range in [S II]/Hα, which likely implies that we are sampling SNRs within a similar range of shock velocities.

Interestingly, we find a bimodal distribution for the metallicity-sensitive [N II]/Hα in our PHANGS-MUSE SNRs. The top branch matches well with SNRs in M83, a high-mass and high-metallicity galaxy, while the bottom branch overlaps with SNRs in M33, a low-mass and low-metallicity galaxy. Some SNRs in M51 occupy the same location in this plot with the top branch of our SNRs but some SNRs have much higher [N II]/Hα ratios than any other SNRs. For NGC 6946, the SNRs lie in between the two branches of our SNRs.

We also attempted to determine whether this trend exists within our 19 galaxies, as shown in Fig. 18. In this figure, SNRs belonging to the same galaxy are represented by the same color, ranging from red to purple as the stellar mass of the galaxy decreases. We observe the same trend as identified from the four literature targets, with higher mass systems exhibiting higher [N II]/Hα ratios than lower mass galaxies, which likely relates to metallicity offsets between these targets. A more detailed investigation of these trends with metallicity is beyond the scope of this work, but also agrees qualitatively with the trends expected based on shock models (see Fig. 16).

In summary, the comparison with MAPPINGS models in Fig. 16 and with the nearby SNR population in Fig. 17 provides a crucial validation of our SNR selection process and the purity of our SNR catalog. Despite not being able to resolve their structure, it is clear that we are picking objects that are consistent with the parameter space of shocks, as well as the observed range of properties of well-studied SNRs in nearby galaxies.

2.5 DISCUSSION

2.5.1 *Expected number of supernova remnants and inferred supernova frequencies*

We have identified 2233 objects that we classify as SNRs or SNR candidates in 19 nearby galaxies. To explore the completeness of our sample, we compare it with a theoretical estimation of the number of SNRs we expect in each galaxy. The number of core-collapse (CC) SNRs correlates with the star formation rate (SFR) surface density. To estimate the number of SNRs in each galaxy, we calculated the SN rate per unit area following the formalism presented in Bacchini et al. (2021) as

$$R_{cc} = \Sigma_{SFR} f_{cc}, \tag{2}$$

where Σ_{SFR} is the SFR surface density and $f_{cc} \approx 1.3 \times 10^{-2} M_{\odot}^{-1}$ represents the number of core-collapse SNRs for a unit of stellar mass formed under a Kroupa (2002) initial mass function. We neglect SNe associated with type Ia here; however, as estimates of the ratio of CC to type Ia SNe ranges from about 3:1 to 1:1 (Li et al. 2011; Mannucci et al. 2005), accounting for these only decreases the value of f_{cc} by a factor of two at most.

We estimate the SFR surface density from the dust-corrected Hα luminosity (Kennicutt 1998) as

$$\mathrm{SFR}(M_{\odot}\,\mathrm{yr}^{-1}) = 7.9 \times 10^{-42} L(H\alpha)(\mathrm{erg\,s}^{-1}). \tag{3}$$

We account for dust attenuation using the Balmer decrement, assuming a fixed Hα/Hβ = 2.86 (Storey & Hummer 1995) based on Case B recombination and the Calzetti attenuation curve and R_V=3.1 (Calzetti 2001). Combining SFR, the MUSE field of view (FoV) area, and the estimated time (10,000 – 20,000 years; Badenes et al. 2010; Sarbadhicary et al. 2017) for which SNRs remain visible in the optical, we estimate the expected number of SNRs for each galaxy. The comparison of the estimated SNR number and identified SNR number is provided in Fig. 19. For the majority of galaxies, the number of identified SNRs is around half of the expected number of SNRs. When taking the parent sample as a whole, including both SNRs and SNR candidates, we find a better agreement with our simplistic estimation. This suggests that we are recovering about half of the expected SNRs, even more if a large number of our SNR candidates are true SNRs.

In almost all cases, we find fewer SNRs than would be predicted. This is not surprising, as our approach was not designed to be maximally complete. The few galaxies that show more SNRs than predicted do not show any consistent global properties, although one of these (NGC 5068) is the closest galaxy in our sample and another (NGC 4303) is one of the seven galaxies that hosts an AGN. Within the Milky Way, only ~30% of identified SNRs were chosen based on optical observations (Green 2019), suggesting we can expect to miss a large number of objects. On the other hand, we cannot distinguish SNRs due to core collapse from Type Ia ones, which might cause a (small) excess of observed SNRs when compared to our theoretical estimation (Eq. 2). Overall, given the tantalizing correlation between our expected and observed SNR numbers, this suggests that our parent sample is surprisingly indicative of the total estimated SNR population in the surveyed areas.

If we believe we are achieving a fairly complete census of SNe, we can also directly compute an upper limit to the SN frequency for our sample of galaxies. If we assume SNRs remain visible in the optical for 10,000 years (Sarbadhicary et al. 2017), then on average we find a SN frequency of one per 85 years per galaxy, with values of the average time between SNe within individual galaxies ranging from 30 to 476 years (Fig. 20). The galaxies with less frequent SNe (lowest number of SNe per galaxy) are found to be our most distant ($D > 18$ Mpc) targets, which makes sense as we are more likely to have missed SNe in these cases where our physical resolution is worse. The average SN frequency increases to one per 65 years per galaxy if we only consider the 13 galaxies with distances less than 18 Mpc. We find no significant secondary correlation with integrated galaxy properties like global SFR or stellar mass, but our sample is still small. These SN frequencies are only upper limits due to the uncertainties in the SNR visibility timescales but are similar to the frequency of one per 40±10 years estimated for our own Milky Way (Tammann et al. 1994), which is reasonably well matched to the median stellar mass and SFR in our sample of galaxies. Scaling this to the stellar mass contained within the MUSE field of view, this corresponds to a median SN rate per unit mass (SNu; Mannucci et al. 2005) of 1 SNe per 10^{10} M per century.

2.5.2 *Lessons learned when identifying supernova remnants with integral field units*

By using multiple criteria to select objects for our parent sample, we find we are able to nearly double the number of objects identified compared to using any one diagnostic alone. The combination of [O I]/Hα residuals and [S II]/Hα residuals gives the largest number of sources, 1749, corresponding to ~78% of the objects in the parent sample. The combination of [O I]/Hα residuals and BPT (OI-OIII) gives the second largest number of sources, 1703. The BPT diagnostics select fewer objects than the line ratio residual approaches (Table 2); however, they are almost all (~90%) identified as robust (isolated) SNRs by our method. Taken together, all five methods have distinct diagnostic powers.

Our results when using these five different techniques to identify SNRs and SNR candidates reflect the fact that the optical properties of SNRs present a variety of emission-line characteristics, particularly when seen in projection against nearby H II regions and DIG. There is no singular feature that provides high confidence in our SNR classification, but instead, the emission-line characteristics provide a continuous spectrum, with increasing confidence of a correct classification the more independent features we observe. However, we lack an independent method to confirm our classification, making it challenging to robustly determine 'best practices' for SNR determination. Shock models like MAPPINGS provide some guidance (Fig. 16); however, a richer set of highly resolved emission-line maps of SNRs, either via observations (e.g., Drory et al. 2024) or simulations (e.g., Makarenko et al. 2023), would significantly improve our understanding of how to best identify and classify SNRs that are blended with background emission. By introducing an automated approach to source detection, we hope that future work can begin a more systematic exploration of the completeness limits probed by IFU datasets through the injection of simulated objects to test how well SNRs with different characteristics are recovered.

There are other line ratio combinations, not explored in this work, that could also potentially serve as useful diagnostics for the classification of SNRs in IFU datasets. For example, [Fe II]λ8616/Paschen11λ8862 should be higher in SNRs than in H II regions, as iron lines are strong shock indicators (Oliva, Moorwood & Danziger 1989; Reipurth et al. 2000). Unlike other optical [Fe II] lines that are produced by continuum pumping fluorescence (such as λ4287 or λ5158), λ8617 is essentially produced by collisional excitation at low excitation levels (Méndez-Delgado et al. 2021; Mendoza et al. 2023; Rodríguez 1999; Verner et al. 2000). This characteristic, combined with the low ionization potential of Fe^{+}, makes it a promising shock indicator analogous to other [Fe II] lines at far-infrared wavelengths, such as the bright [Fe II] 1.64 µm line (Antoniucci et al. 2014). Additionally, while Fe is typically depleted into dust grains in HII regions (Izotov et al. 2006; Rodríguez 2002), shock waves are capable of efficiently destroying these dust grains and releasing Fe into its gaseous phase (Méndez-Delgado et al. 2022; Mesa-Delgado et al. 2009). Therefore, in the case of overlapping between

SNRs and H II regions, this indicator could favor the conditions of the SNRs. We see clear evidence of this line in some of our spectra; however, the strong neighboring sky lines make a robust extraction of line fluxes challenging and beyond the scope of this work.

The [S III]λ9069/[S II]λ6716,6730 ratio might also be used to diagnose the ionization mechanism (Long et al. 2022). In H II regions, [S III]/[S II] correlates strongly with ionization parameter (Kewley et al. 2001), but it can span a wide range of values depending on the local ISM density and the radiation field produced by the ionizing source (Groves et al. 2023). As shown in L22, high values of [S III]/[S II] provide strong indications of H II regions, but low values are more challenging to interpret as the separation with H II regions is not clear and [S III] can be too weak.

2.5.3 *Classification of the candidate sample and blending with HII regions*

In Sect. 3.3, we only focus on properties of 1166 SNRs, whereas there are still 1067 SNR candidates. Even though we are less certain these are SNRs, they are robust detections using diagnostics that give strong evidence for shock excitation. We also saw in Sect. 2.5.1 that including these objects provides better agreement with the expected number of SNRs given the SFR in each galaxy, and in Sect. 2.3.3 we showed that in M83 about half of our candidates are true SNRs in Long et al. 2022.

One reason it is difficult for us to confirm the nature of individual objects is due to the blending of emission arising from different ionizing sources within our ~100 pc apertures. As shown in Table 2, 202 SNRs (17%) and 569 SNR candidates (53%) are blended with H II regions. In Fig. 21 we see that more than half of the SNR candidates overlap with H II regions and that these objects exhibit systematically lower [S II]/Hα line ratios. This is expected if bright photoionized emission, which exhibits systematically lower ratios, is blended with an unresolved SNR. Clearly, we have more confidence in classifying objects as SNRs when they are isolated. At our resolution, we cannot determine if blended objects are physically associated with H II regions or they just appear in projection against the H II region along our line of sight. In total, 35% of objects in the parent sample are not isolated sources.

As is shown in Sect. 2.4.1, the majority of SNRs that exhibit large Hα luminosities (Fig. 13) are found to be blended with H II regions and have the lowest [S II]/Hα and [O I]/Hα line ratios. Interestingly, if we remove these blended SNRs from the sample then we find a relatively sharp upper Hα luminosity threshold of ~$10^{37.5}$ erg s^{-1}. At these distances, it remains a challenge to properly decompose SNRs from the surrounding photoionized emission, but from our combination of multiple line diagnostics and novel use of the [S II]/Hα residual to account for blended photoionized emission, we have succeeded in identifying a large sample of objects that would have been missed by previous searches.

This can be seen more directly in the four SNR examples shown in Fig. 2. In the third row, it is clear from the Hα intensity that this object sits in a complex star-forming environment, as reflected by the extended photoionization-dominated nebulae outlined in red (left panel). In the [S II]/Hα map this object is not pronounced, but in the residual map it becomes more distinct from the background. Detailed deblending of such objects is beyond the scope of this work but it could be improved in the future by the use of higher-resolution imaging of the ionized hydrogen line emission from HST (Barnes et al. 2022) and JWST (Barnes et al. 2023).

2.5.4 *Characterizing the shocked regions*

Congiu et al. (2023) and Egorov et al. (2023), have both presented catalogs of objects classified as 'shocked' using the same MUSE data for the same sample of 19 galaxies, and here we compare our catalog with their results.

C23 used a contour-based algorithm to identify peaks in a weighted average of [O III]λ5007, Hα and [S II]λ6716, 6731 flux maps. Regions are defined by the surface brightness contours around the closest peak. In this way, the same set of 19 MUSE galaxies are segmented into 40,920 regions and by comparing with different model grids the regions are classified into five types: H II regions, shocked regions (6336), ambiguous, planetary nebula, and unknown. We cross-matched these regions with our parent sample and compare their classification.

Our sample is 35% smaller in total than the 'shocked' sample in C23. 1676 objects (75%) of our parent sample can be associated with the C23 segmentation mask. The 25% of objects missed is comparable to the ~35% of objects that had not been identified in Groves et al. (2023), suggesting that many SNRs are missed when selecting by emission-line flux and morphology alone. Of the objects that can be cross-matched to the C23 catalog, 676 (38%) of our regions are classified as shocked. This is only about 10% of the total number of shocked regions in C23. The SNRs sample shows a better overall agreement, with 512 (56%) of our SNRs identified as shocked in C23. The differences in classification likely reflect a difference between our empirical diagnostics and the model grids used in that work. Moreover, line ratios from our integrated spectra can appear consistent with photoionization (Fig. 11b), given the frequent blending with H II regions and the contamination from the DIG background, which would result in a C23 classification of 'H II region'.

To further demonstrate that the usage of a combination of emission-line ratios and gas kinematics helps to improve the identification of SNRs, we compare our objects with about 1500 regions of locally elevated Hα velocity dispersion identified by E23 in the same sample of galaxies. Only 23% of objects in our catalog reside in the regions identified by E23. This indicates that the kinematic information alone is usually not sufficient for SNR identification. Meanwhile, about 320 unresolved regions with high-velocity dispersion from E23 are considered to be probable SNR candidates because of their high [S II]/Hα line ratio. 65% of these regions coincide with the objects in our catalog. Visual inspection of the remaining objects demonstrates that the majority of them reside in very low surface brightness regions making their classification uncertain, and leaving us with only 25 (about 7%) SNR candidates from E23 that are not present in our catalog.

2.6 CONCLUSIONS

Using optical IFU data from the PHANGS-MUSE survey (Emsellem et al. 2022), we constructed a new catalog identifying 1,166 SNRs plus 1,067 SNR candidates in 19 nearby galaxies, doubling the number of known SNRs in the local universe.

We summarize the key results below:

- We used a total of five criteria to identify objects with `astrodendro` in our ~50 pc resolution observations. Four criteria are based on line-ratio diagnostics ([S II]/Hα, [O I]/Hα, and two BPT diagnostics), and the fifth criterion is based on the [S II] emission-line velocity dispersion. Hα morphology is not used as a criterion in our selection.

- Instead of identifying sources directly in the line ratio maps, we constructed [S II]/Hα and [O I]/Hα residual maps, where we could identify objects that emit brightly at these line ratios given their Hα surface brightness. This allowed us to naturally account for background and foreground photoionized emission, consisting of contributions from both H II regions and DIG.

- Using multiple diagnostics increased our sample size and provided a natural mechanism to robustly construct a SNR catalog. Our SNR catalog consists of all objects identified by at least two criteria, or having integrated line ratios meeting both of the criteria [S II]/Hα > 0.4 and [O I]/Hα > 0.1. The remaining objects are classified as SNR candidates.

- We validated our method by applying it to MUSE observations of M83 (Della Bruna et al. 2022). All of the SNRs we identified using our method are found in literature catalogs (L22), along with 77% of our SNR candidates, giving us confidence that our method is robustly identifying SNRs.

- We demonstrated that the SNRs in our sample have line ratios and line kinematics distinct from H II regions, are consistent with MAPPINGS shock models, and are similar to literature SNR samples. Variations between galaxies in our sample are consistent with the expected variations with metallicity, given the difference in galaxy stellar mass found in our sample.

- We estimated the total number of expected SNRs based on theoretical models, given the current SFR in each galaxy, and we find this agrees within a factor of two with the total number of objects identified. This suggests that while our sample is incomplete, it is illustrative of the SNR population.

- By using line ratios and line kinematics to identify our objects, we were able to locate SNRs that are seen in projection against bright star-forming regions. About 17% of our SNRs are blended with H II regions, while 52% of the SNR candidates are blended. This blending makes confirmation of SNR candidates as true SNRs challenging.

Building statistical samples of SNRs provides a new avenue to quantify the impact of stellar feedback; however, it remains difficult to estimate how complete these SNR catalogs are. By studying a large sample of galaxies with IFU data, we have begun exploring how automatic identification of objects allows us to systematically produce large uniform catalogs. Based on the multiple different criteria explored in this work, [O I]/Hα is the most successful at selecting objects for our parent sample (62%). BPT diagnostics select fewer objects, but they are almost all (~90%) identified as robust (isolated) SNRs.

With these techniques, it is easy to imagine that the next steps can include the injection of simulated objects with different characteristics to quantitatively determine how many can be recovered. High physical resolution simulations have also already begun to provide insights into the interpretation of these variable diagnostics, and the importance of accounting for contaminating background emission (Makarenko et al. 2023). Given the growing number of galaxies observed with multiple emission lines mapped at ~100 pc scales, these automated approaches to identifying SNRs have great potential to significantly increase our SNR samples in the coming years.

ACKNOWLEDGEMENTS: We thank Dr. Angela Adamo for generously sharing M83 data. We extend our sincere gratitude to Dr. Eva Grebel and Dr. Andreas Sander for their valuable discussions and contributions that inspired the concept of the supernova rate (SN rate) in our research.

JL, KK, J.E.M-D and OE gratefully acknowledge funding from the Deutsche Forschungsgemeinschaft (DFG, German Research Foundation) in the form of an Emmy Noether Research Group (grant number KR4598/2-1, PI Kreckel) and the European Research Council's starting grant ERC StG-101077573 ("ISM-METALS").

G.A.B. acknowledges the support from the ANID Basal project FB210003.

F.B. acknowledges support from the INAF Fundamental Astrophysics program 2022.

SCOG and RSK acknowledge financial support from the European Research Council via the ERC Synergy Grant "ECOGAL" (project ID 855130), from the German Excellence Strategy via the Heidelberg Cluster of Excellence (EXC 2181 - 390900948) "STRUCTURES", and from the German Ministry for Economic Affairs and Climate Action in project "MAINN" (funding ID 50OO2206).

Based on observations collected at the European Southern Observatory under ESO programmes 094.C-0623 (PI: Kreckel), 095.C-0473, 098.C-0484 (PI: Blanc), 1100.B-0651 (PHANGS-MUSE; PI: Schinnerer), as well as 094.B-0321 (MAGNUM; PI: Marconi), 099.B-0242, 0100.B-0116, 098.B-0551 (MAD; PI: Carollo) and 097.B-0640 (TIMER; PI: Gadotti).

This research made use of `astrodendro`, a Python package to compute dendrograms of Astronomical data (http://www.dendrograms.org/). Other main Python Packages that have been used are `ASTROPY` (Astropy Collaboration et al. 2013, 2022; Price-Whelan et al. 2018), `NUMPY` (Harris et al. 2020), `MATPLOTLIB` (Hunter 2007) and `PYNEB` (Luridiana, Morisset & Shaw 2014).

Table 1 lists the distances that were compiled by Anand et al. (2020) from Freedman et al. (2001), Jacobs et al. (2009), Kourkchi et al. (2020), Kourkchi & Tully (2017), Nugent et al. (2006), and Shaya et al. (2017) and Scheuermann et al. (2022).

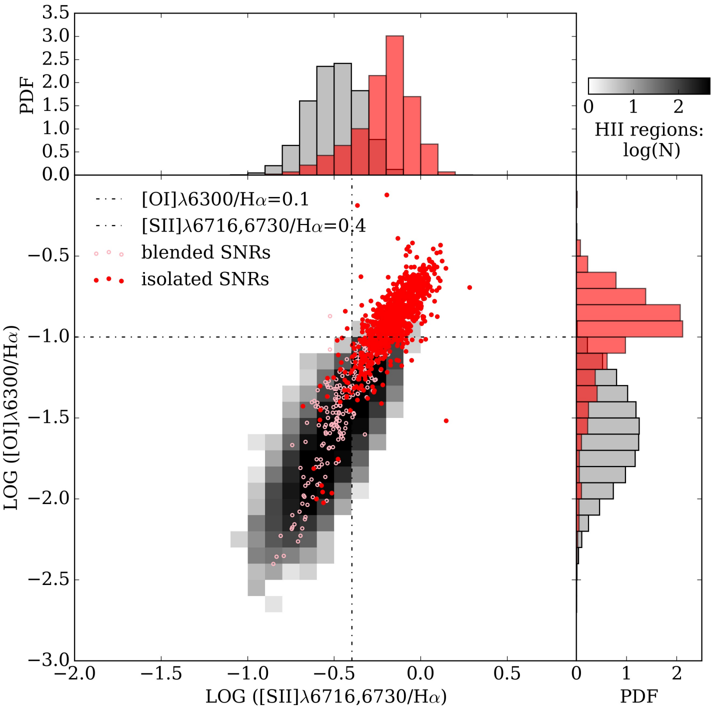

(a) Supernova remnants.

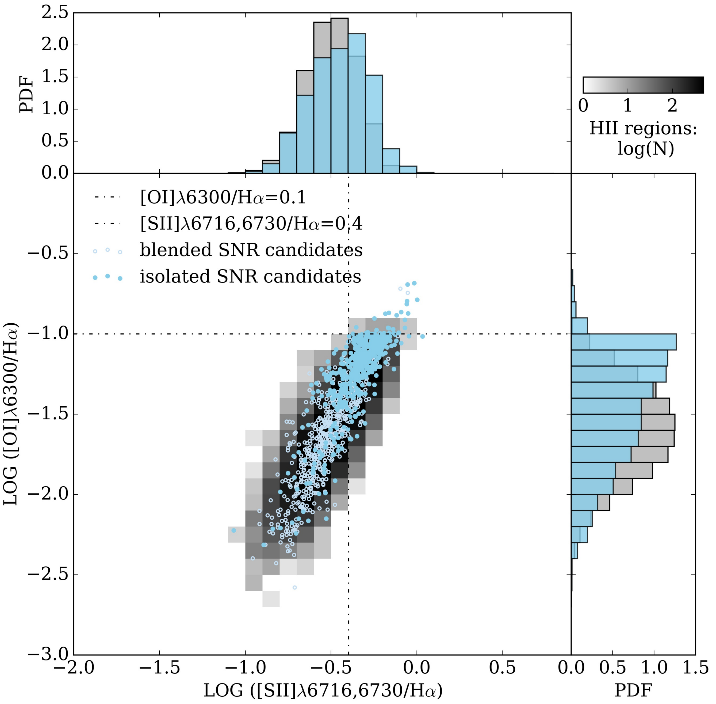

(b) Supernova remnant candidates.

Figure 11: Distribution of identified objects and H II regions density (in grayscale) in the [O I]/Hα versus [S II]/Hα plane. Panel (a): SNRs (red dots); Panel (b): SNR candidates (blue dots). For objects that overlap with a H II region, the symbol is an empty circle in light red or blue. Identified objects tend to occupy different spaces than H II regions in the [O I]/Hα versus [S II]/Hα plane. However, this tendency is more obvious for a SNR than a SNR candidate.

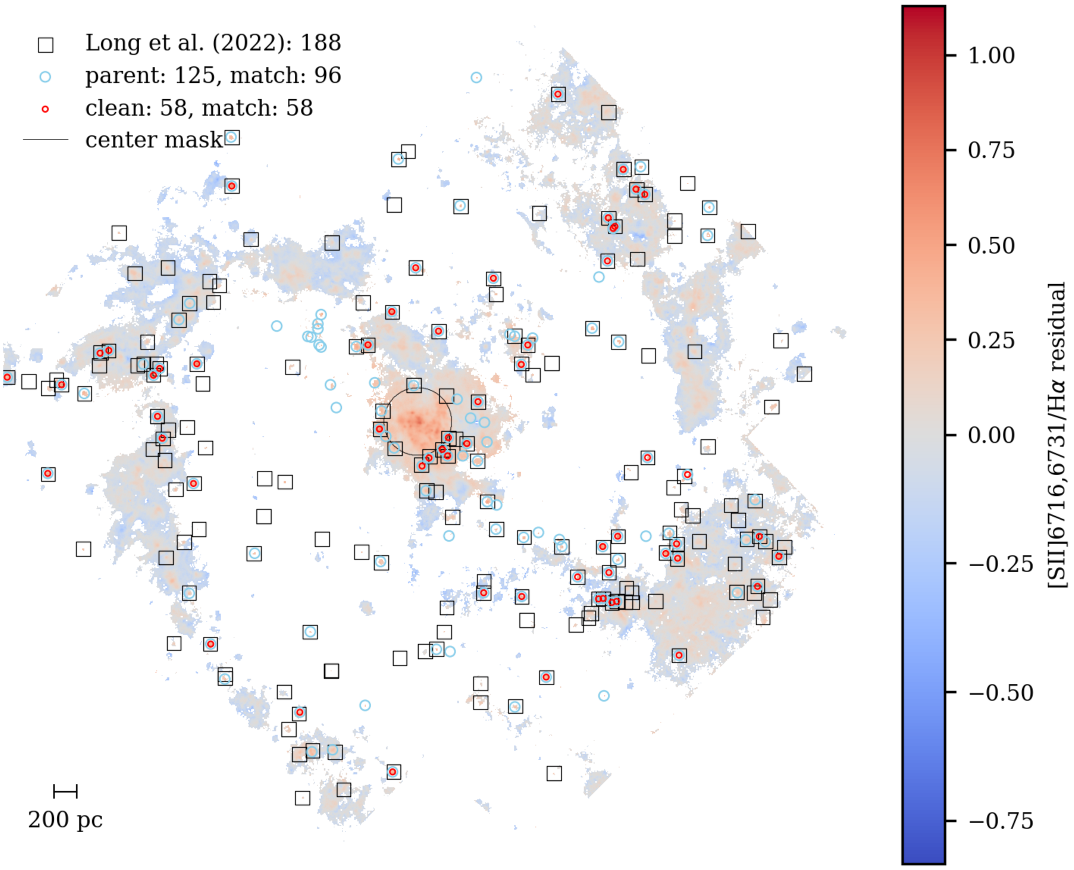
□ Long et al. (2022): 188
○ parent: 125, match: 96
○ clean: 58, match: 58
— center mask
200 pc
1.00
0.75
0.50
0.25
0.00
−0.25
−0.50
−0.75
[SII]6716,6731/Hα residual

Figure 12: SNRs in M83. The locations are indicated of SNRs identified by Long et al. (2022) (black boxes) and those identified by applying methods used in this work (red circles for SNRs and blue circles for SNR candidates). All the objects we identify as SNRs are also identified as SNRs in Long et al. (2022). Overall, 77% of our parent sample were previously identified as SNRs in the literature.

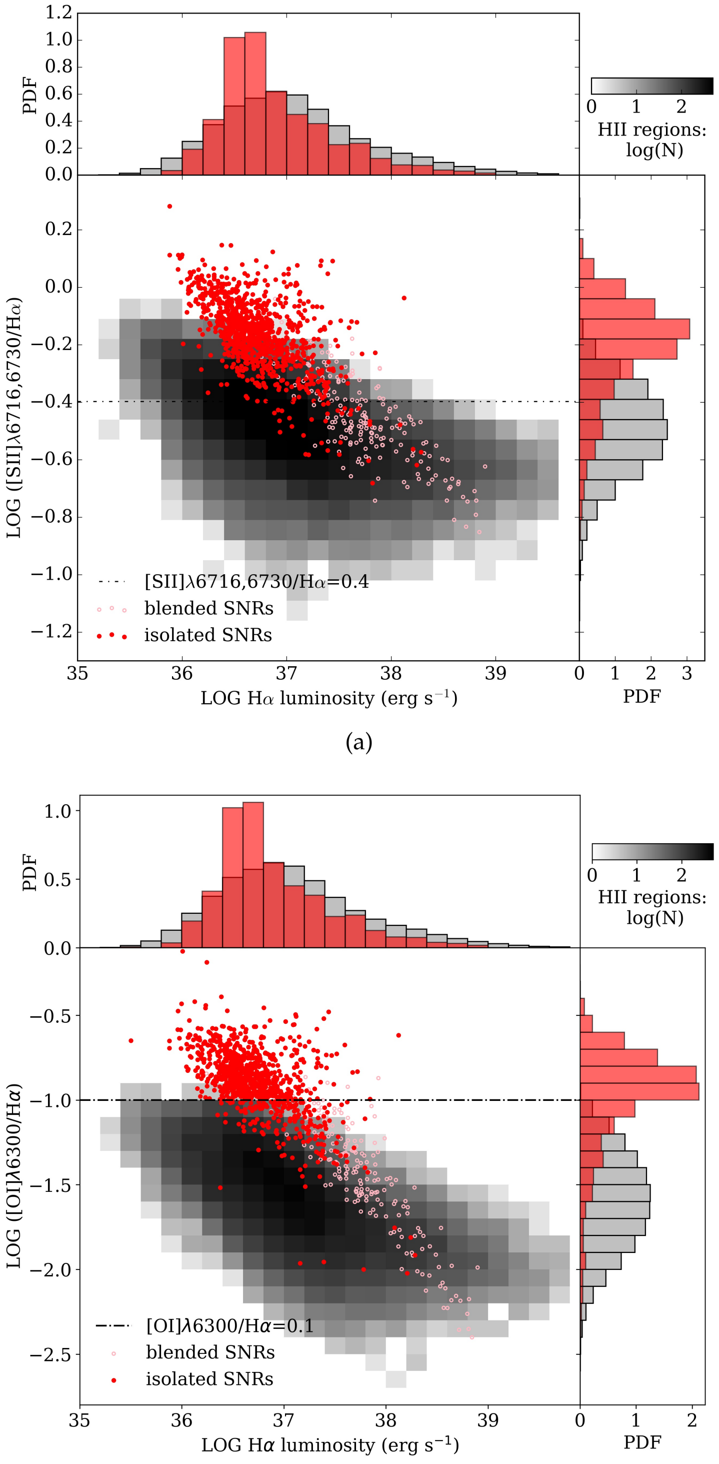

(a)

(b)

Figure 13: [S II]/Hα (top) and [O I]/Hα (bottom) versus Hα luminosity for SNRs (red dots) compared with the H II regions density distribution (in grayscale). For SNRs that overlap with a H II region, the symbol is an empty circle (in light red). Thresholds of [O I]/Hα=0.1 and [S II]/Hα=0.4 (horizontal dash-dotted lines) are shown. SNRs overlapping with H II regions are selected by other criteria so they can still be identified as SNRs. Emission lines are not corrected for the photoionization.

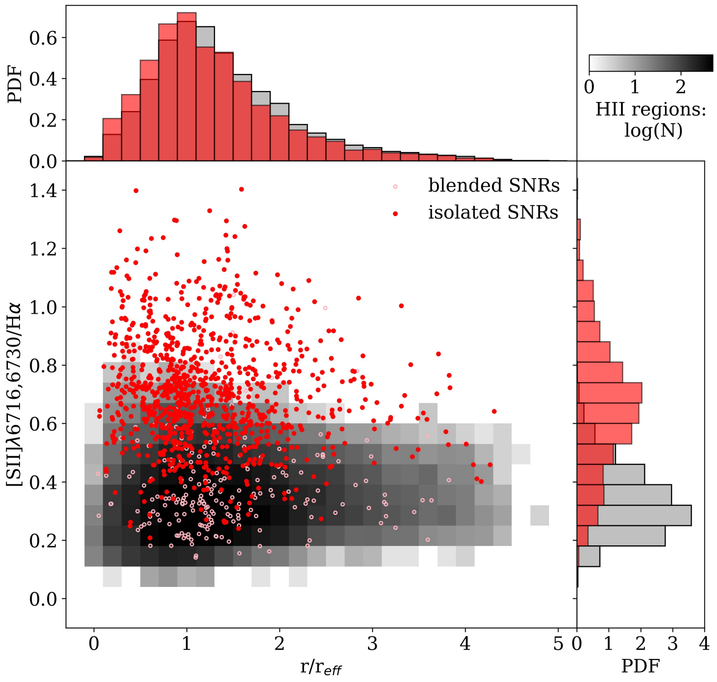

(a)

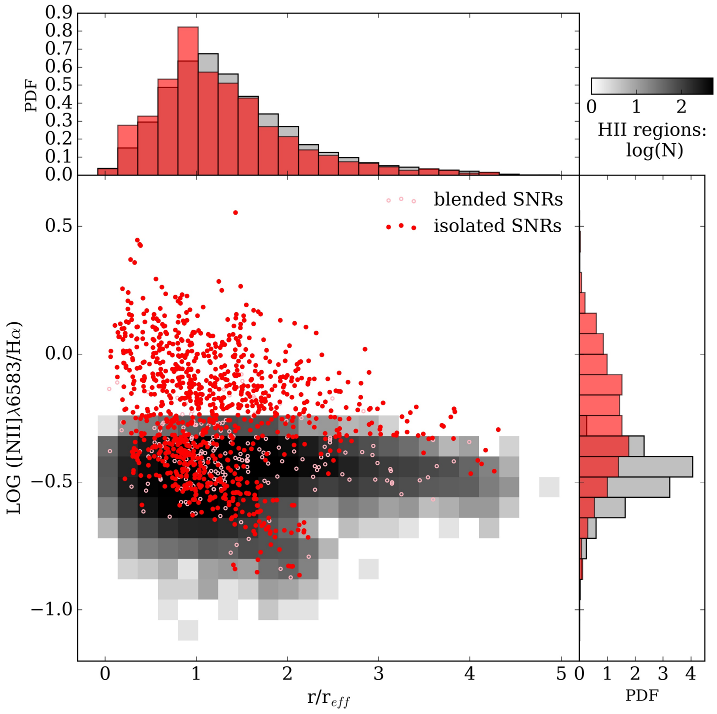

(b)

Figure 14: Radial trends of SNRs and H II regions. r/r$_{\text{eff}}$ is the ratio of SNR distance to the effective radius of the corresponding galaxy. Panel (a): [S II]/Hα changes with the distance to their corresponding galactic centers for SNRs (red dots) and H II regions (in grayscale). Panel (b): [N II]λ6583/Hα change with the distance to their corresponding galactic centers for SNRs (red dots) and H II regions (in grayscale). For SNRs that overlap with a H II region, the symbol is an empty circle in light red. The drop in the numbers at low r/r$_{\text{eff}}$ is likely influenced by the mask in the centers of the galaxies.

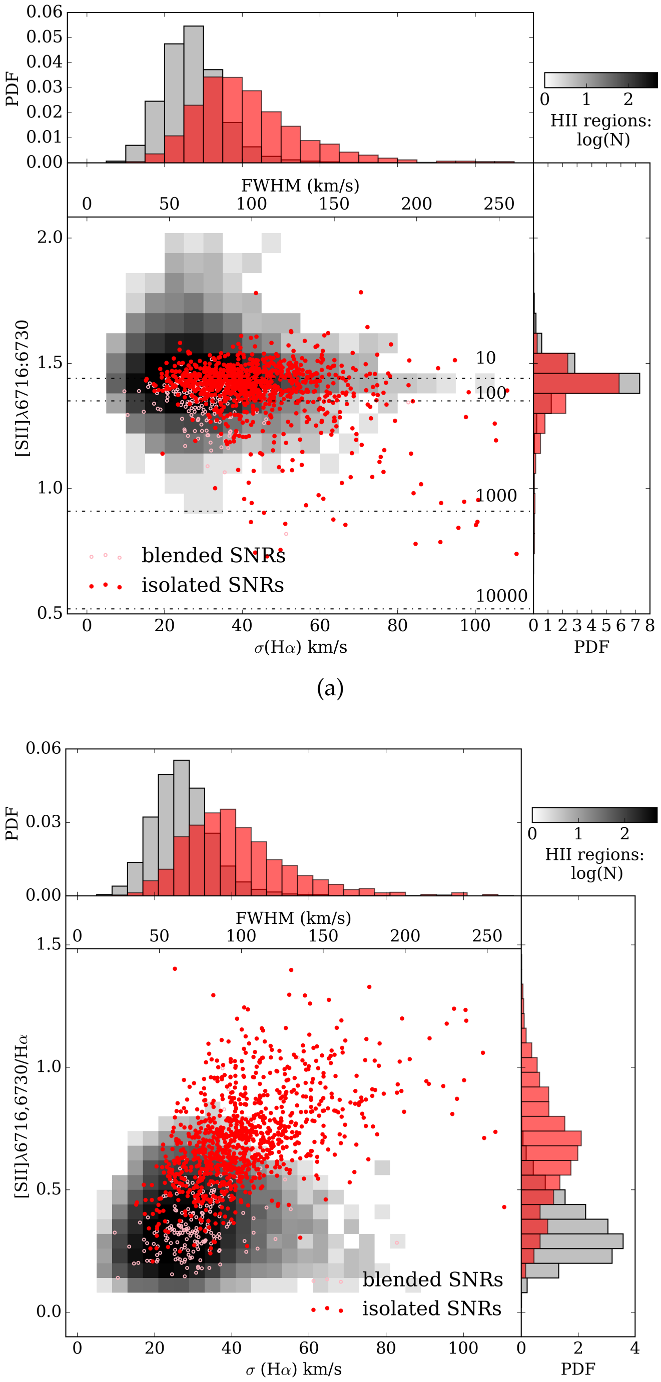

(a)

(b)

Figure 15: Comparison of emission-line ratios and velocity dispersion for supernova remnants (SNRs) and H II regions. Panel (a): Line ratios of [S II] versus velocity dispersion of SNRs and H II regions. The top axis shows the FWHM. The Hα velocity dispersion changes with the [S II]λ6716/[S II]λ6730 ratio for SNRs (red dots) and H II regions (in grayscale). The ratios above 1.4 are not physical and are due to noise. The horizontal dash-dotted lines indicate different electron densities with the corresponding value next to it. Panel (b): Velocity dispersion of Hα changes with [S II]λ6716,6730/Hα ratio for SNRs (red dots) and H II regions (in grayscale). For SNRs that overlap with a H II region, the symbol is an empty circle in light red. These two criteria work effectively together in distinguishing between SNRs and H II regions.

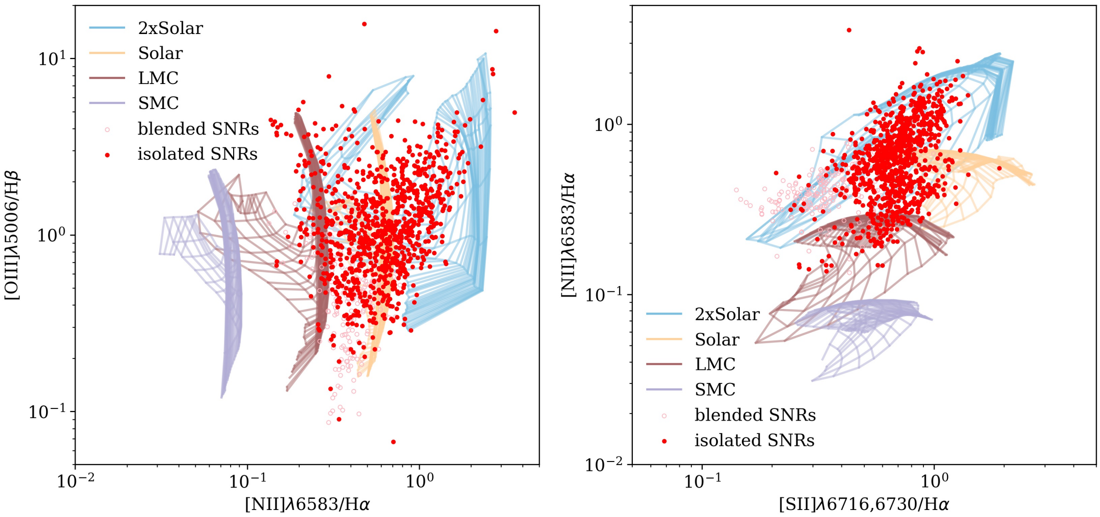

Figure 16: Comparison of supernova remnant properties with MAPPINGS models. Left: Observed [O III]λ5006/Hβ versus [N II]λ6583/Hα for SNRs (red dots). Right: Observed [N II]λ6583/Hα versus [S II]/Hα for SNRs (red dots). For SNRs that overlap with a H II region, the symbol is an empty light red circle. Background grids are MAPPINGS models with different metallicities. Our identified SNRs mostly lie between models for LMC and twice solar metallicities.

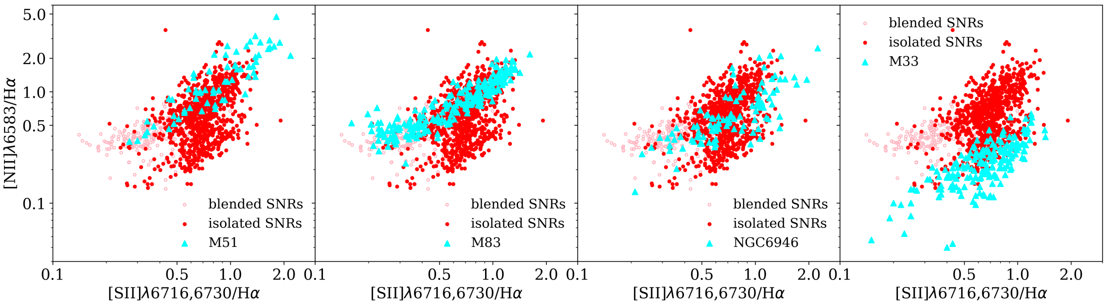

Figure 17: Relation between [S II]/Hα ratio and [N II]/Hα ratio for SNRs identified in four nearby galaxies from the literature (Long et al. 2018, 2022; Long, Winkler & Blair 2019; Winkler et al. 2021) and 19 MUSE galaxies. SNRs are marked with red dots; SNRs that overlap with a H II region are marked as an empty circle in light red.

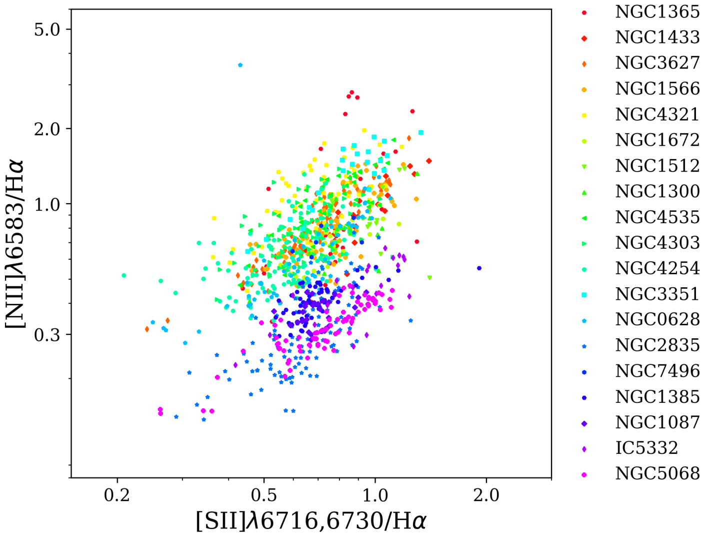

Figure 18: Relation between [S II]/Hα ratio and [N II]/Hα ratio for SNRs in 19 galaxies. SNRs in the same galaxy are marked in the same color and with the symbol. In the legend, from top to bottom, the stellar mass of the galaxy decreases, from $10^{11} M_\odot$ for NGC 1365 to $10^{9.41} M_\odot$ for NGC 5068.

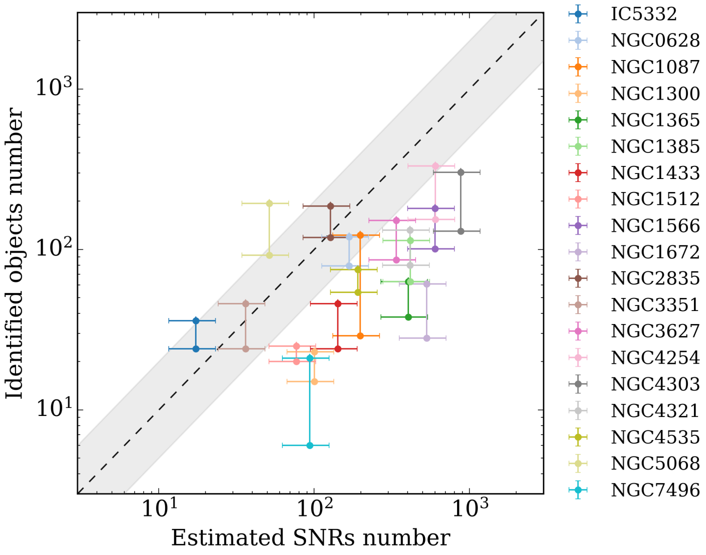

Figure 19: Comparison between the estimated SNR number from the SFR and objects identified in this paper. The lower limit of the identified object is the number of SNRs and the upper limit is the number in the parent sample including SNR candidates. The lower limit of the estimated SNR number is given by the optically visible time of SNRs for 10,000 years and the upper limit corresponds to 20,000 years. The dashed black line is the one-to-one relation. The shaded area provides coverage from two times the recovery rate to 50% of the recovery rate of SNRs.

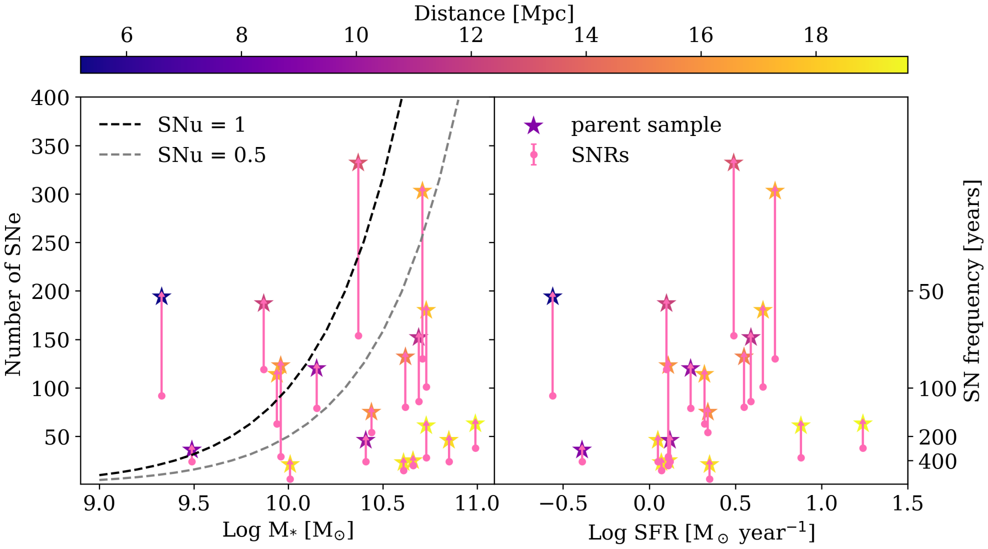

Figure 20: Number of SNe as a function of stellar mass (left) and SFR (right) considering the entire parent sample, colored by galaxy distance and considering galaxy integrated properties measured only within the MUSE field of view. These SN counts can also directly be converted to a SN frequency by assuming SNRs are visible in the optical for 10,000 years. Lines of constant SN rate per unit mass (SNu) are also shown. The star markers represent the number for the parent sample while the circles are the number of SNRs. The line between them shows the range of possible true SNR numbers.

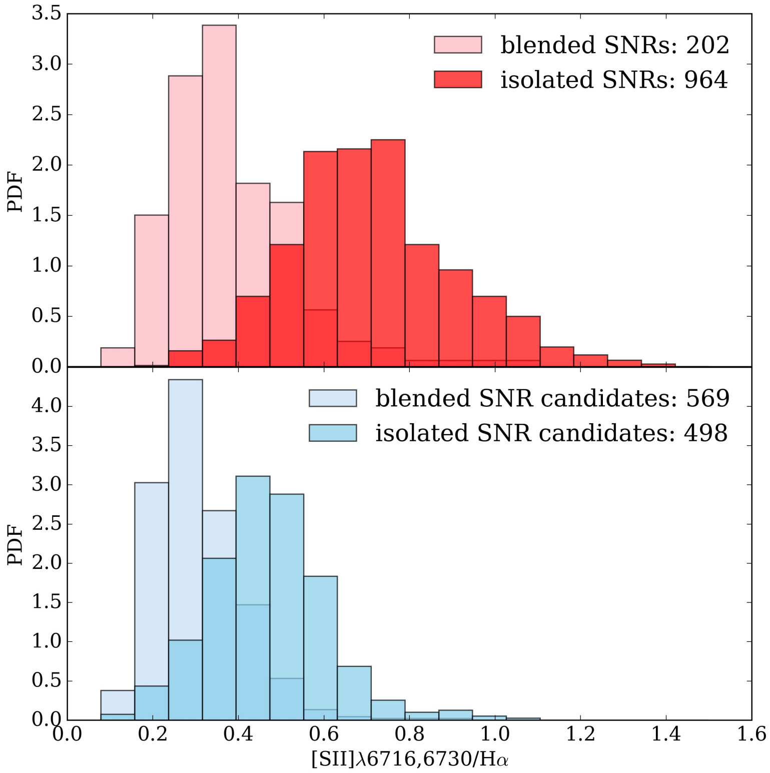

Figure 21: Probability distribution functions of [S II]/Hα for SNRs and SNR candidates that are isolated or overlap with H II region. More SNR candidates (bottom) overlap with H II regions (blended) and have lower [S II]/Hα values than SNRs (top).

3

INVESTIGATING THE SUB-KPC METALLICITY ENVIRONMENT OF SNRS IN NEARBY HIGH-MASS STAR-FORMING GALAXIES

This chapter, including Appendix B, is based on a manuscript currently in preparation for submission to the journal *Astronomy & Astrophysics* under the same title.

Contributions: The text, figures, and data analysis presented here were primarily carried out by the thesis author. The scientific concept, scope, and overall structure of the project were developed in regular discussions with the supervisor, Dr. Kathryn Kreckel, who also provided detailed feedback and guidance throughout the manuscript preparation. Other co-authors contributed by offering suggestions during the development of the analysis and interpretation. Specific input from collaborators is still being incorporated as the paper is not yet finalized. In particular, discussions with Dr. Sumit Sarbadhicary, Dr. Adam Leroy and other members of the collaboration have influenced the scientific framing and contextualization of the results.

The version presented here reflects the current draft at the time of thesis submission and may be subject to changes during the peer-review process.

Abstract: Supernova feedback plays a crucial role in shaping the interstellar medium, driving turbulence, regulating star formation, and influencing the evolutionary pathways of galaxies. Studying the metallicities at supernova remnant sites provides key insights into the physical conditions where SNe occur, as well as the role they play in the chemical enrichment of the ISM, offering a probe of stellar evolution and stellar feedback. Using ~100 pc PHANGS-MUSE optical integral field spectroscopy of nearby star-forming galaxies, we combine the largest extragalactic survey of 1,166 optically selected SNRs with metallicity measurements obtained at the locations of nearby H II regions. We investigate the dependence of SNR occurrence rates on the metallicity of their surrounding ISM and analyze their distribution with respect to local gas-phase metallicity. Our results suggest no significant trend in SNR occurrence rates as a function of ambient metallicity. This may indicate that the metallicity of the ISM does not play a dominant role in influencing SN and SNR formation, or our metallicity coverage is not broad enough to see the clear trend.

Authors: Jing Li (李婧), Kathryn Kreckel, Sumit Sarbadhicary, Oleg V. Egorov, Enrico Congiu, Simon C. O. Glover, Adam Leroy.

3.1 INTRODUCTION

Supernova remnants (SNRs) play a fundamental role in shaping the interstellar medium (ISM) and regulating galaxy evolution by injecting energy and enriching the ISM with heavy elements. After supernova (SN) explosions, SNRs are key tracers of the sites of stellar feedback. They also offer a direct means of studying shock propagation and gas cooling under diverse environmental conditions (Sarbadhicary et al. 2025).

As the direct observation of SN events has grown over time, increasing statistics are available to study how local conditions might impact the rate of SN explosions and their variations for different SN types (Kochanek et al. 2017). Trends observed with host galaxy mass point towards possible dependence on local gas-phase abundance (metallicity) (e.g. Gandhi et al. 2022; Graur et al. 2017b), as this could impact stellar evolution via changes in binary fraction or the initial mass function. However, previous studies have primarily relied on historical supernova (SN) samples and global metallicity estimates (e.g., galaxy centers), which may obscure local variations in interstellar medium (ISM) conditions.

In addition, the literature provides no clear consensus on the specific trends with metallicity. While some observational work suggests that core-collapse SNe (CCSN) preferentially occur in low-metallicity environments (Frohmaier et al. 2020; Pessi et al. 2023), other studies report weak or no correlation between SN rates and metallicity (Briel et al. 2022; Graur et al. 2017a; Schulze et al. 2021). In a recent detailed study of SN host environment metallicities, Pessi et al. (2023) found a particularly striking trend in which high mass galaxies preferentially host SN in low metallicity environments and the occurrence rate of CCSN decreases with the increase of metallicity. These discrepancies likely reflect differences in spatial resolution, sample size, and metallicity diagnostics. Typically, the resolution (1–2 kpc) of large integral field unit (IFU) surveys such as CALIFA (Husemann et al. 2013) or MaNGA (Bundy et al. 2015) is larger than the physical size of H II regions, which are less than a few hundred parsecs. Therefore, their metallicity measurements are not only from the H II region but also the nearby diffuse ionised gas (DIG) (Poetrodjojo et al. 2019). Moreover, spatially resolved studies such as Sánchez et al. (2019) show that even within individual galaxies, metallicity can vary significantly on sub-kiloparsec scales, further complicating the interpretation of environmental metallicity at the explosion sites of SNe.

While any individual galaxy is unlikely to have had an observed SN event (Mayker Chen et al. 2023, 2024), their expanding shock wave can be visible for thousands of years as a SNR (Sarbadhicary et al. 2017), with hundreds detected in any individual galaxy (Li et al. 2024; Long 2017; Long et al. 2022). These SNRs represent a novel tracer of the underlying SN distribution. With physical sizes smaller than 100 pc (Asvarov 2014; Long et al. 2010; Tüllmann et al. 2011), high physical resolution measurements are capable of isolating SNRs and neighboring H II regions, providing robust probes of the local ISM metallicity.

In this work, we exploit optical integral field spectroscopy from the PHANGS–MUSE survey (Emsellem et al. 2022) to study the metallicity of SN sites via an analysis of the SNR population. While the number of SN events for these galaxies remains low (Mayker Chen et al. 2024), a large catalog of SNR sites is available (Li et al. 2024). This is the largest spatially resolved extragalactic SNR sample to date – identifying 1166 SNRs and 1067 SNR candidates across 19 nearby star-forming galaxies (Li et al. 2024). This high-mass galaxy regime is particularly well probed by the PHANGS-MUSE galaxy sample (Emsellem et al. 2022), where detailed measurements and maps of the metal abundances are also available (Groves et al. 2023; Williams et al. 2021). By assuming that ISM abundances are smooth on sub-kpc scales due to efficient mixing (Kreckel et al. 2020; Li et al. 2021; Metha, Trenti & Chu 2021), this enables us to test whether SNRs prefer to exist in low or high local metallicity regions.

This paper is organized as follows: Section 3.2 outlines the sample selection based on SNR identification, along with the methodologies used for measuring metallicity and star formation rate. Section 3.3 presents our results on the SNR distributions and their correlation with ISM metallicity. In Section 3.4, we compare our findings with theoretical predictions and prior observations, discussing implications for galaxy evolution. We conclude in Section 3.5 with a summary and prospects.

3.2 DATA AND METHODS

Our analysis is based on optical integral field spectroscopic data from the Physics at High Angular Resolution in Nearby GalaxieS (PHANGS)–MUSE survey (Emsellem et al. 2022), which provides spatially resolved optical emission-line maps of nearby star-forming galaxies at a resolution of approximately 100 parsecs.

This dataset offers several key advantages. It includes deep optical spectra covering important diagnostic emission lines such as [S II]:$\lambda\lambda$6716,31, Hα, Hβ, [O I]:$\lambda\lambda$6100, and [O III]:$\lambda\lambda$5007 that are essential for distinguishing shock-heated from photoionized nebulae. Along with the ~100 pc spatial resolution, this enables the identification of individual H II regions and SNRs. Gas-phase metallicity measurements are based on strong-line calibrations as presented in Groves et al. (2023). The dataset also provides spatially resolved star formation rate (SFR) maps calculated from Balmer-decrement corrected Hα combined with WISE 22 μm and GALEX FUV maps, as described by Belfiore et al. (2023). Their calibrations account for dust heating by older stellar populations and are accurate to within ~10% at ~100 pc scales.

In the following sections, we provide more details about these datasets from the PHANGS-MUSE survey.

3.2.1 *SNR Catalog*

We use the PHANGS-MUSE SNR catalog from Li et al. 2024, where SNRs were identified using a combination of emission-line diagnostics and gas kinematic criteria. We refer the reader to the paper for details, and only summarize here the multi-criterion approach. First, elevated [O I]/Hα ratios were used as an indicator of shock ionization. Second, elevated [S II]/Hα ratios served as another tracer of shocked gas. Third, enhanced gas velocity dispersion was considered, since SNRs generally exhibit broader emission lines due to expanding shock fronts. Fourth, the distance to the diagnostic classification line in the BPT diagram comparing [O III]/Hβ versus [O I]/Hα was used. Fifth, the distance to the diagnostic classification line in the BPT diagram comparing [O III]/Hβ versus [S II]/Hα was also taken into account. These five diagnostics together enabled robust identification of SNR candidates.

By selecting objects that meet at least one of the five diagnostic criteria, we identified 2,233 candidate SNRs across the 19 galaxies in our sample. To ensure robustness, we focus our analysis on a high-confidence subsample of 1,166 SNRs that satisfy at least two criteria. When compared to the theoretical expectation for the number of SNRs per galaxy, we find that, for most galaxies, the number of high-confidence SNRs is approximately half of the expected value. However, when considering the full sample, including both high-confidence SNRs and candidates, the total number shows better agreement with our simplified estimates.

3.2.2 *Measuring ISM Metallicity*

We use metallicities from the nebular catalog from Groves et al. (2023), which derives gas-phase oxygen abundance (a proxy of metallicity) for individual H II regions using the strong-line S-calibration (Pilyugin & Grebel 2016). Such strong-line techniques, extensively applied in large extragalactic surveys (e.g., Pilyugin, Grebel & Kniazev 2014), provide a robust framework for mapping gas-phase abundances across late-type galaxies.They measure the radial metallicity gradients, following the approach in Kreckel et al. (2019), then remove the radial gradient in metallicity and calculate the second-order variations in metallicity, Δ(O/H), for all galaxies. Typical measurement uncertainty is around 0.01 dex. In Groves et al. (2023), 23,244 out of 30,790 nebulae are classified as H II regions.

Since SNRs are sites of nucleosynthesis and metal enrichment, we expect a metallicity gradient as a function of distance from the SNR location (Thornton et al. 1998). To verify this, in Figure 22, we show the Δ(O/H) – i.e., deviations from the radial metallicity gradient – as a function of distance from SNRs. It is difficult to infer metallicity directly from SNR spectra due to shock-excited emission and complex, non-uniform physical conditions. Therefore, we estimate the metallicity from nearby H II regions, which provide more reliable abundance measurements under photoionization equilib-

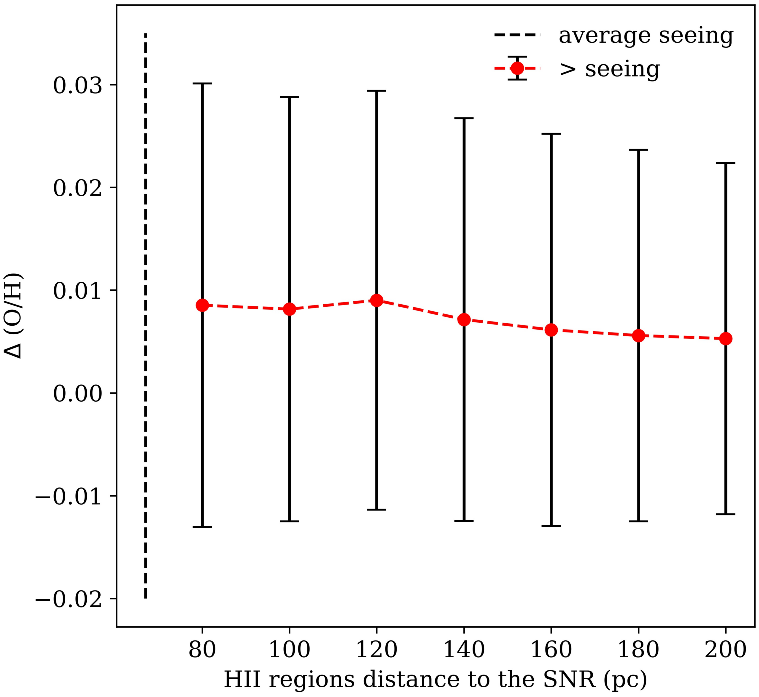

Figure 22: The relation between metallicity residual and distance of H II regions to the SNRs. The average seeing is approximately 67 pc across all galaxies, and H II regions within this distance have been excluded to avoid seeing-related blending effects.

rium (Anderson et al. 2010; Niino, Nagamine & Zhang 2015). This approach is supported by previous studies that have used the metallicity of surrounding H II regions as a proxy for progenitor environments, showing that such measurements can meaningfully reflect the conditions from which the progenitor stars formed (Anderson et al. 2010). We compare the metallicity residual of H II regions located at different distances from SNR sites. The difference in metallicity residual between regions at 100 pc and 200 pc is only 0.002 dex, which is an order of magnitude smaller than the typical measurement uncertainty (~0.01 dex). 2671 H II regions for 1166 SNRs are considered at 100 pc (on average two H II regions per SNR) while 8486 H II reigons for 1166 SNRs are considered at 200 pc (on average 7 H II regions per SNR). This indicates that any metallicity gradient around SNRs is negligible, and our result is independent of the physical scale (up to 200 pc) we select for characterizing the metallicity at the SNR location. We adopt a fiducial distance range of 67–100 pc to estimate the metallicity at each SNR site, taking the median metallicity of H II regions within this range. The inner limit (67 pc) reflects the average seeing across the 19 galaxies.

To evaluate the potential impact of metallicity calibration choice, we also tested alternative methods, including the D16 calibration (Dopita et al. 2016), which has been used in previous studies (e.g. Pessi et al. 2023). While the absolute scales differ slightly, we find a consistent, systematic correlation between methods. Therefore, the choice of calibration does not affect our conclusions. For consistency with other PHANGS-MUSE studies, we adopt the metallicities reported by Groves et al. (2023) throughout the main analysis. Comparative plots demonstrating this cross-method consistency are provided in Appendix B.1.

For each SNR site, we take the median metallicity of nearby H II regions located within 67–100 pc, excluding those whose emission overlaps with an SNR (referred to as "blended SNRs" in Li et al. 2024). We do not impose a minimum number of H II regions for interpolation. The interpolated metallicity at the SNR site is then taken as the median metallicity of the selected H II regions. To clarify, the "SNR metallicity" refers to this interpolated value and is an estimate of the intrinsic gas-phase metallicity at the SNR location.

3.2.3 *Galaxy Star Formation Rate Maps*

To estimate the local star formation rate (SFR), we utilize the SFR maps from Belfiore et al. (2023), which are based on Hα emission corrected for dust attenuation using Balmer decrement and Milky Way extinction (O'Donnell 1994). Since SNRs themselves emit Hα, they are not masked in the SFR maps, making pixel-level SFRs potentially unreliable. Moreover, SFRs are typically defined at the galaxy or sub-kiloparsec scale, rather than for individual pixels (Calzetti 2013). These measurements represent time-averaged star formation over ensembles of star-forming regions, rather than the instantaneous SFR at a specific location. To ensure that the SFR is meaningful on the timescale relevant to the indicators used, we smooth the SFR maps from Belfiore et al. (2023) with a Gaussian kernel corresponding to a physical scale of 1 kpc. As Niino et al. (2015) point out, metallicity measurements at spatial resolutions larger than ~1 kpc tend to average over multiple nearby H II regions, rather than reflect small-scale local variations. This supports our approach of characterizing the broader star-forming environment, rather than pinpointing precise explosion sites. Furthermore, Li et al. (2021) find that metallicity fluctuations—after subtracting global radial gradients—exhibit a typical correlation length of ~1 kpc in a sample of 100 nearby galaxies, with the scale increasing with stellar mass and SFR. Their results provide empirical support for our choice of smoothing scale in both the SFR and metallicity maps.

3.3 RESULTS

In this section, we present our results on the spatial distributions of SNRs, the occurrence of SNRs and their correlation with ISM metallicity.

Figure 23 shows the cumulative distribution of star formation rate (SFR) as a function of gas-phase metallicity, similar to the methodology and Figure 1 of Pessi et al. 2023. For each point along the curve, the x-axis represents a metallicity value, and the

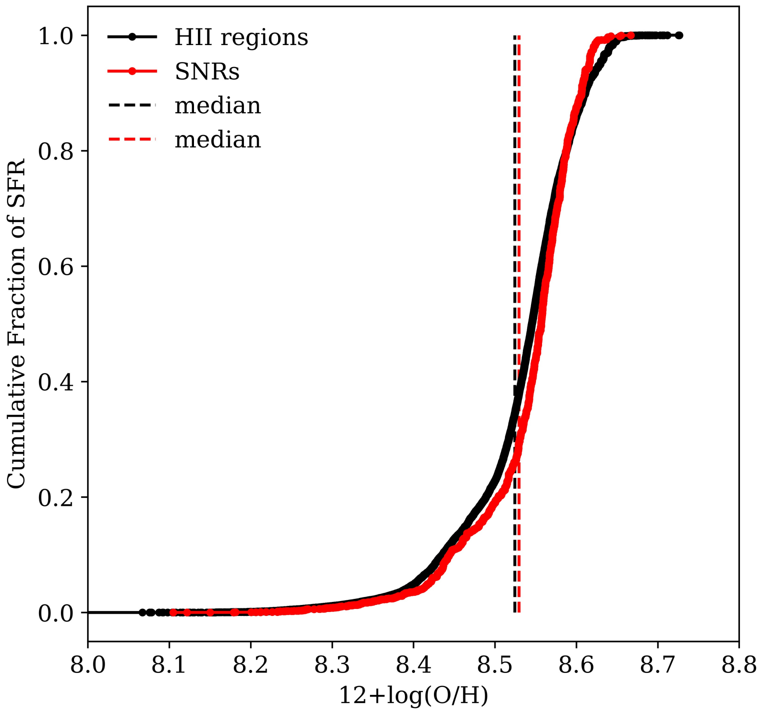

Figure 23: Cumulative distribution of star formation rate (SFR) as a function of 12+log(O/H). The black line shows the distribution for all H II regions in the 19 galaxies, while the red line represents H II regions located near SNRs. Dashed lines indicate the respective median metallicities.

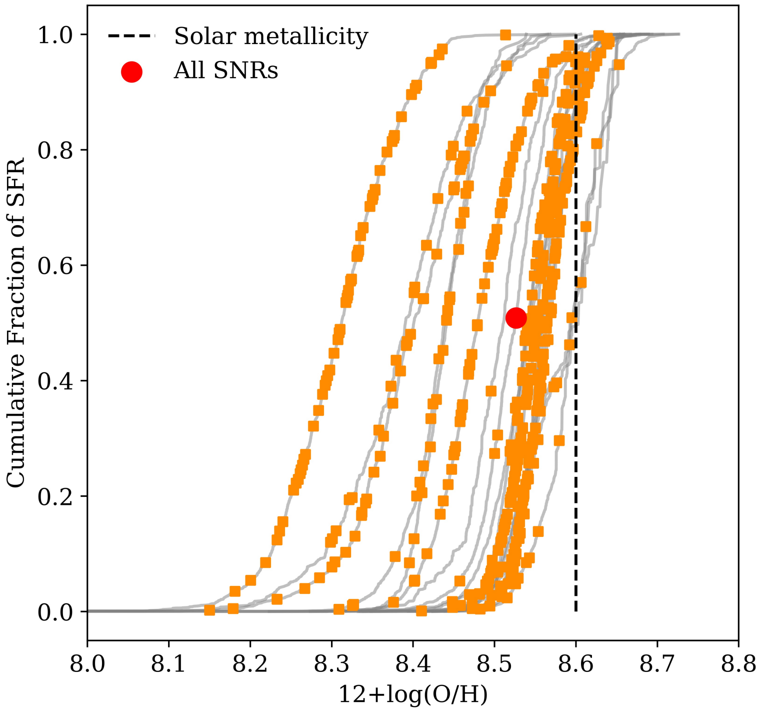

Figure 24: Cumulative distribution of SFR as a function of [O/H] for individual galaxies. Each gray line corresponds to one galaxy's H II region distribution. Orange squares mark the metallicity and SFR rank of the corresponding SNR environments. The dashed black line at 12+$\log_{10}$(O/H) = 8.6 indicates a solar-like metallicity threshold. The red dot denotes the median SNR metallicity across the full sample.

y-axis shows the fraction of total SFR occurring at or below that metallicity. This is computed by sorting all regions by metallicity, summing the corresponding (linear) SFRs, and normalizing by the total SFR. The black curve represents the cumulative SFR distribution of all H II regions across the 19 galaxies in our sample. The red curve shows the same, but only for SNRs given their estimated metallicity. The two curves closely track each other, with a median metallicity difference of only ~0.01 dex – comparable to the measurement uncertainties. We therefore conclude that SNRs are not preferentially located in environments with systematically higher or lower metallicity than the overall star-forming regions in these galaxies.

In Figure 24, we further examine metallicity trends on a per-galaxy basis. Each gray line represents the cumulative SFR fraction of the H II regions as a function of metallicity for a given galaxy. Orange markers indicate the SNR environment's metallicity position within its host galaxy's distribution. The red marker represents the median metallicity for all SNRs. The corresponding SFR fraction is very close to 0.5, which means SNRs are not preferentially located in low- or high-metallicity regimes. As seen

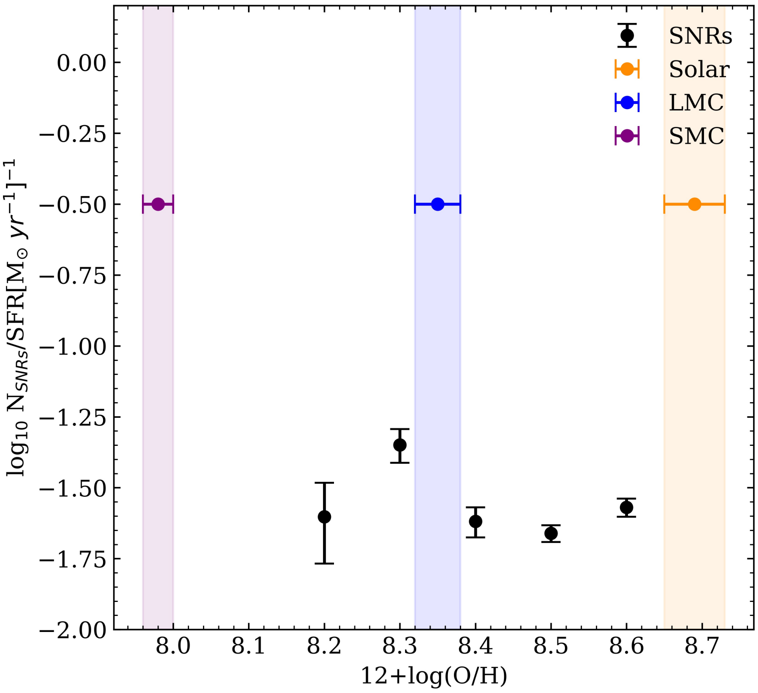

Figure 25: SNR occurrence per unit of star formation rate, plotted as a function of metallicity, estimated by dividing the number of SNRs by the total SFR within each 0.1 dex metallicity bin. The black points represent bin medians. Vertical error bars represent Poisson uncertainties in SNR counts. The orange dot marks the solar abundance (Asplund, Amarsi & Grevesse 2021), while the blue and purple dots represent median metallicities of the LMC and SMC, respectively (Domínguez-Guzmán et al. 2022).

in Fig. 23, the range of metallicities probed by our sample is fairly narrow and focused on the high metallicity regime. This also holds for individual galaxies, and in fact, for each galaxy, we find that the upper end of the metallicity distribution exceeds solar metallicity (8.6 dex).

Figure 25 provides a statistical view of SNR frequency normalized by SFR across different metallicity bins (each bin = 0.1 dex), ranging from 8.15 to 8.75. The count in each bin is [10, 54, 67, 219, 187], so the uncertainty is largest for the first bin, as there are only ten data points. When we fit data points, including the influence of uncertainty, we still do not observe a significant preference for SNRs to occur in any particular metallicity environment.

To place our analysis in context, it is useful to consider how supernova remnants (SNRs) relate to the more commonly studied supernova (SN) events. Studies of SN events are limited to the human timescales over which we have been able to detect and classify these explosions, typically less than the past 100 years, and are visible for even shorter periods of time. Our analysis focuses on the cumulative presence of

SNRs, which remain detectable for much longer periods (Sarbadhicary et al. 2017). For a rough estimate, assuming a typical SN rate of one per 100 years, about 100 SNRs could be visible per galaxy over a 10,000-year timescale due to the longer observability of remnants. As a result, it is unsurprising that the normalization in the y-axis (SNRs per unit SFR) is approximately 100 times higher in our plot than in similar metrics based on SN rates.

3.4 DISCUSSION

We have found no strong correlation between SNR occurrence and local ISM metallicity. The spatial density of SNRs remains relatively uniform across a 0.5 dex metallicity range, suggesting that environmental metallicity does not significantly influence SNR occurrence rates. This is in contrast to what was suggested by Pessi et al. (2023) for SN identified in high metallicity locations, but is consistent with their findings for lower metallicity galaxies. Our analysis is broadly comparable to their work, though several key differences and caveats must be considered.

First, our dataset does not distinguish between core-collapse and Type Ia SNe. Second, SNRs can remain visible for approximately 10,000–20,000 years, which affects their detectability compared to transient SN events. Third, SNRs are the radiating shock wave of the explosion in the ISM, so they are only visible if the surrounding ISM conditions are appropriate (Long et al. 2022). We also note that in this work, we are not able to account for all selection biases in the optical identification of SNRs, particularly due to surface brightness limits, contamination from H II regions, and the limitations of line-ratio diagnostics. These may obscure subtle environmental dependencies (Kopsacheili et al. 2020; Long 2017; Mantovanini, Hurley-Walker & Anderson 2025). However, given the order of magnitude change in core-collapse SN rate reported by Pessi et al. 2023, for all trends to be removed while using SNR tracers in our work would require a fine-tuned set of coincidences.

Overall, our findings suggest that the formation and occurrence rate of SNRs we identify are broadly insensitive to local ISM metallicity, at least within the high metallicity regime probed by our sample. This contrasts with certain theoretical expectations, which propose that lower-metallicity environments may foster more extended SNR evolution due to reduced radiative cooling (Hu et al. 2016; Thornton et al. 1998). Our results imply that local density inhomogeneities, turbulence, and pre-supernova feedback exert a stronger influence on SNR evolution than metallicity, effectively masking any metallicity-dependent trends (Martizzi et al. 2015; McLeod et al. 2021).

With our data set, we are also able to search for signatures of changing abundance patterns as a function of distance from the SNRs (Figure 22), but find no significant variations. Metal enrichment and mixing from earlier generations of stars may homogenize the ISM, reducing spatial metallicity gradients relevant to SNR evolution. For SNRs, even if shocks propagate at 1,000 km/s over 10,000 years, they would only reach distances of about 10 pc. These scales cannot be probed with our current data. From the SILCC simulations (Walch et al. 2015) and the pre-SN clearing work by Chevance et al. (2021), it is evident that the SN site needs to be pre-processed for the feedback to impact larger scales, rather than remaining confined within individual clouds. If such pre-processing had occurred, we might expect to observe its effects on the surrounding metal distribution, but we clearly do not, at least out to distances of 200 pc. To rigorously test this and avoid contamination from other nearby past star-forming events, we repeated our analysis using only isolated SNRs, as defined by Li et al. (2024). In this case, we also did not observe a significant difference between lower and higher metallicity range.

A key limitation of our work is that our sample spans a metallicity range of $8.0 < 12 + \log(\mathrm{O/H}) < 8.8$, with most galaxies clustering around 8.5–8.6 (Groves et al. 2023). This means we do not probe the low metallicity regime extensively. Instead, our analysis focuses more closely on the high metallicity end, where Pessi et al. (2023) previously identified a potential trend. By exploring this 'extreme' end of the metallicity distribution, we are able to test whether a steep drop in SNR rate is apparent, and do not find a significant effect. Future work that incorporates more metal-poor systems, such as dwarf galaxies, may be better suited to revealing such dependencies over a more representative metallicity range.

A final important caveat of our analysis is the lack of progenitor type classification. Our SNR sample does not distinguish between Type Ia and core-collapse events. Since only core-collapse supernovae originate from massive, short-lived stars capable of ionizing their surrounding ISM into H II regions, not all of our H II region–SNR metallicity pairs are suitable for probing the birth environment of massive stars. This limitation may further weaken any observable correlation between SNR presence and local ISM metallicity. The ratio of core-collapse SNe to Type Ia SNe ranges from 3:1 to 1:1 (Li et al. 2011; Mannucci et al. 2005); however, we believe our identified SNRs are largely representative of core-collapse SNe, since the number of SNRs observed does correlate with the SFR in the galaxies as shown in Li et al. (2024).

3.5 CONCLUSIONS

Our study presents the sub-kpc-scale investigation of how local ISM metallicity relates to the occurrence and properties of SNRs, using a sample of 1,166 high-confidence SNR candidates across 19 nearby star-forming galaxies from PHANGS–MUSE.

We find SNRs are not preferentially found in either low- or high-metallicity environments within the metallicity range probed ($12+\log(\mathrm{O/H}) \sim 8.0$–8.8). Both the cumulative SFR distributions and SNR frequency normalized by SFR show minimal variation with metallicity, with median metallicities differing by only ~0.01 dex – comparable to typical measurement uncertainties (~0.01 dex). This suggests that local gas-phase metallicity does not play a dominant role in where SNRs are found within moderately metal-rich galactic disks.

We address several key questions that have remained unresolved in previous studies. While earlier research often relied on global or kpc-scale metallicity estimates, potentially obscuring local environmental trends, our integral-field analysis at approximately 100 pc resolution enables a more precise isolation of the metallicity in the immediate neighborhood of SNRs. Methodologically, we highlight the advantages of inferring metallicity by interpolating from nearby H II regions, rather than relying on shock-contaminated SNR spectra.

While limited to a narrow metallicity range, this work reinforces the idea that environmental metallicity is not a primary factor in SNR occurrence within moderate to solar-metallicity regimes. It provides strong observational constraints for theoretical models of supernova feedback and chemical mixing.

To build on this, future studies could include more metal-poor galaxies, incorporate multi-wavelength observations (e.g., X-ray, radio) for improved SNR classification, and aim for higher resolution metallicity measurements to disentangle small-scale enrichment effects. Such work would further refine our understanding of metal transport and feedback in galaxy disks.

ACKNOWLEDGEMENT:

JL, KK, J.E.M-D and OE gratefully acknowledge funding from the Deutsche Forschungsgemeinschaft (DFG, German Research Foundation) in the form of an Emmy Noether Research Group (grant number KR4598/2-1, PI Kreckel) and the European Research Council's starting grant ERC StG-101077573 (“ISM-METALS").

G.A.B. acknowledges the support from the ANID Basal project FB210003.

F.B. acknowledges support from the INAF Fundamental Astrophysics program 2022.

SCOG and RSK acknowledge financial support from the European Research Council via the ERC Synergy Grant “ECOGAL” (project ID 855130), from the German Excellence Strategy via the Heidelberg Cluster of Excellence (EXC 2181 - 390900948) “STRUCTURES”, and from the German Ministry for Economic Affairs and Climate Action in project “MAINN” (funding ID 50OO2206).

Based on observations collected at the European Southern Observatory under ESO programmes 094.C-0623 (PI: Kreckel), 095.C-0473, 098.C-0484 (PI: Blanc), 1100.B-0651 (PHANGS-MUSE; PI: Schinnerer), as well as 094.B-0321 (MAGNUM; PI: Marconi), 099.B-0242, 0100.B-0116, 098.B-0551 (MAD; PI: Carollo) and 097.B-0640 (TIMER; PI: Gadotti).

This research made use of Python Packages that have been used are `ASTROPY` (Astropy Collaboration et al. 2013, 2022; Price-Whelan et al. 2018), `NUMPY` (Harris et al. 2020) and `MATPLOTLIB` (Hunter 2007).

4

EXPLORATORY WORKS

Contributions: The exploratory works presented in this chapter are based on the author's own analyses of multi-wavelength data within the context of the PHANGS collaboration. These sections are not part of any submitted or published manuscript at the time of thesis submission. The work was carried out under the supervision of Dr. Kathryn Kreckel, who provided general scientific guidance throughout. Some ideas were discussed informally with collaborators, and feedback from group meetings helped shape aspects of the analysis.

4.1 SNR PLACEMENT WITH RESPECT TO MOLECULAR CLOUDS/MOLECULAR GAS

The spatial association between supernova remnants (SNRs) and molecular gas provides key insight into the ambient conditions in which stellar feedback operates. While supernovae (SNe) mark brief explosive events with known subtypes, SNRs provide a time-integrated view of where such explosions occurred, but no longer retain spectroscopic or photometric signatures of the original SN type. As such, SNRs trace the cumulative imprint of feedback, whereas historical SNe pinpoint recent explosions and their environments.

By "placement" we refer to the local molecular gas surface density (Σ_{mol}) at each explosion site, as measured from resolved CO(2–1) maps. Mayker Chen et al. (2023) used this approach to compare 224 SNe (63 stripped-envelope, 101 Type II, and 60 Type Ia) across 43 nearby galaxies, and found that stripped-envelope SNe preferentially occur in regions of high Σ_{mol}, while Type II and Ia SNe are more uniformly distributed.

We apply the same methodology to our much larger SNR sample of 2,233 candidates in 19 galaxies with MUSE and ALMA coverage. Figure 26 presents the cumulative distribution functions (CDFs) of Σ_{mol} at SNR sites (red curves), plotted alongside those for different SN types from Mayker Chen et al. (2023) (orange dashed = Type II, black dotted = stripped-envelope). Two CDFs are shown: one weighted by physical area (top) and one by molecular gas mass (bottom). The vertical lines mark the mean Σ_{mol} for each category. SNRs span a broad range of molecular gas environments, with a peak at moderate surface densities (~10–100 $M_{\odot}$ pc^{-2}). The most extreme, high-density regions are underrepresented, consistent with the view that very young remnants embedded in dense clouds may be optically obscured or undetectable. Moreover, massive stars can rapidly alter their natal environments through early feedback: Chevance et al. (2021) show that molecular clouds are typically dispersed within ~3 Myr by photoionisation, winds, and radiation pressure, well before the first SN occurs. This pre-SN

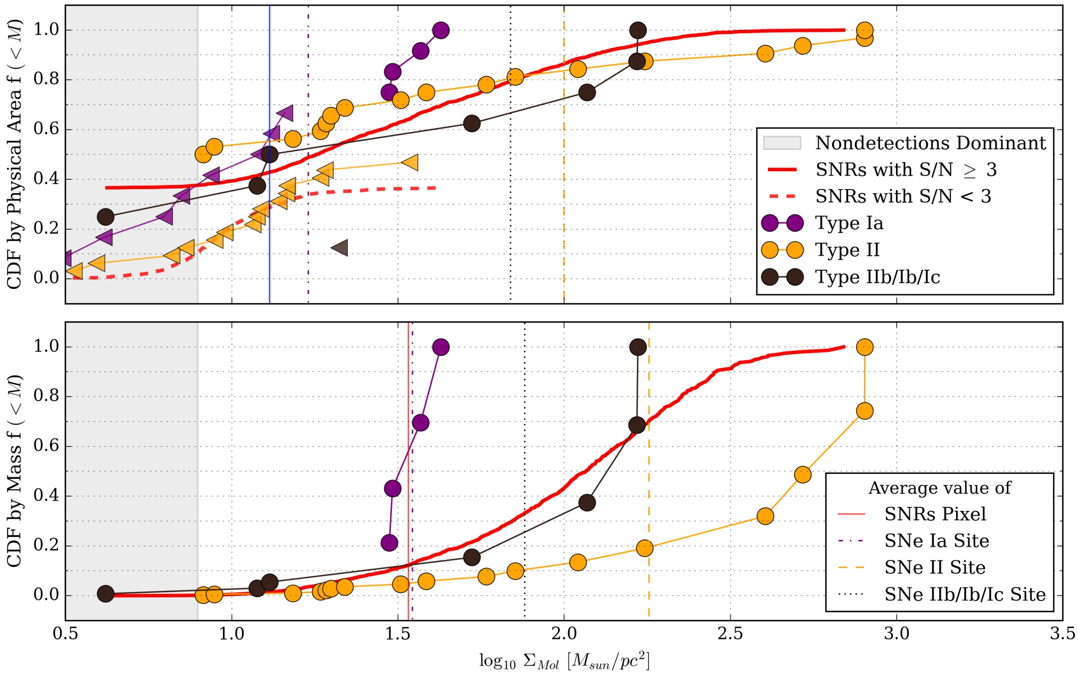

Figure 26: Cumulative distribution functions (CDFs) of molecular gas surface density (Σ_{mol}) at the locations of supernova remnants (SNRs; red curves) compared to supernova subtypes from Mayker Chen et al. (2023) (orange dashed = Type II, black dotted = stripped-envelope). Top panel: CDFs weighted by physical area. Bottom panel: CDFs weighted by enclosed molecular gas mass. Vertical lines indicate the mean Σ_{mol} for each population.

feedback likely reduces the molecular gas density around many SNRs, contributing to their observed scarcity in the highest-Σ_{mol} regions.

The average Σ_{mol} at SNR sites falls between those of Type II and stripped-envelope SNe, suggesting that SNRs sample a mix of feedback environments that evolve over time. Older remnants may have expanded beyond their natal molecular clouds, or their shocks may have disrupted and cleared the surrounding gas. Since we cannot determine the explosion subtype for each remnant, the measured distribution reflects a convolution of multiple progenitor populations, weighted by visibility lifetime and detectability.

Overall, the similarity in trends across both area- and mass-weighted CDFs supports the idea that SNRs provide a complementary view of stellar feedback, probing its longer-term environmental impact in contrast to the instantaneous snapshot offered by historical SNe.

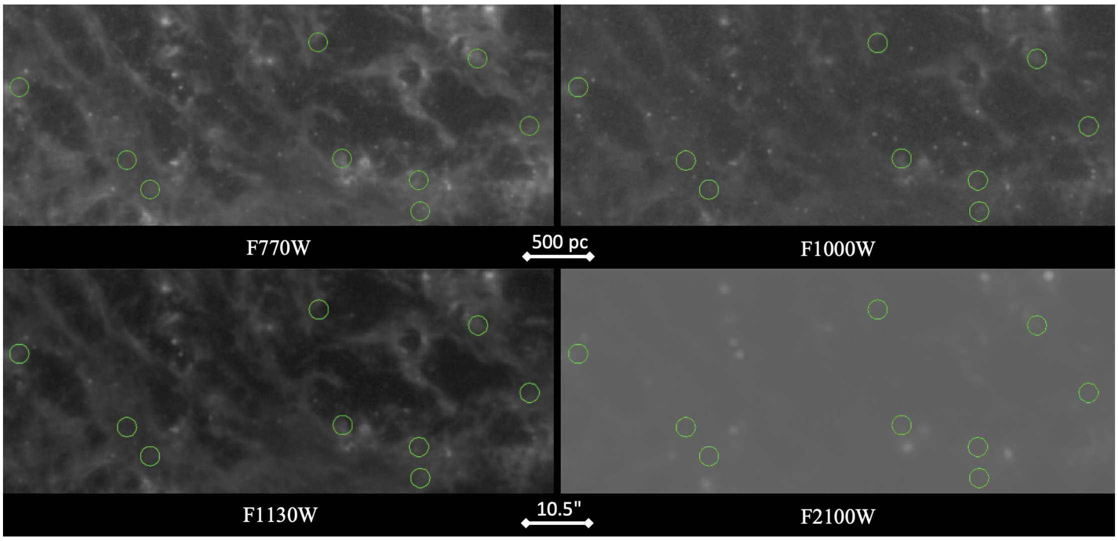

Figure 27: Locations of SNRs (circles) overlaid on JWST/MIRI images (zoom-in views) in four mid-infrared bands: F770W, F1000W, F1130W, and F2100W for NGC 628.

4.2 CONSTRAINING DUST PROPERTIES AT SNR SITES

The interaction between supernova remnants (SNRs) and their surrounding dust environment has long been of interest, particularly in the context of whether shocks can selectively destroy small dust grains and polycyclic aromatic hydrocarbons (PAHs). Theoretical models suggest that the hard radiation fields and mechanical energy of SN shocks are capable of fragmenting or sputtering dust grains, particularly in young remnants with fast shocks. Mid-infrared (mid-IR) observations offer a promising avenue to trace these effects, especially using the unprecedented spatial resolution and sensitivity of the James Webb Space Telescope (JWST). The PHANGS–JWST survey provides systematic multi-band coverage of nearby star-forming galaxies, designed to probe embedded star formation, dust emission, and feedback at scales of a few parsecs (Lee et al. 2023). These datasets are particularly well-suited to studying PAH features in relation to stellar feedback, including SNe and SNRs.

To explore this question observationally, we examined archival JWST/MIRI images for a subset of PHANGS–MUSE galaxies with available coverage. Specifically, we spatially cross-matched our optically selected SNRs with mid-IR emission maps in several MIRI bands (e.g., F770W, F1000W, F1130W, and F2100W), focusing on bands known to trace PAH features. An example SNR–JWST overlay is shown in Figure 27, where the SNR positions are indicated with circular apertures.

Despite the high resolution of JWST, we find that the majority of SNR sites do not exhibit strong localized enhancements or deficits in PAH-tracing emission. This lack of a direct one-to-one correspondence may either reflect a true absence of PAH structure at these locations, or more likely, the strong diffuse background emission masking any subtle local variations. Theoretically, SN shocks are expected to erode or sputter small dust grains and PAHs, with the efficiency depending on grain size, composition, and ambient density (Micelotta et al. 2018).

These findings are broadly consistent with the results of Egorov et al. (2025), who used our SNR catalog to investigate the impact of SN shocks on local PAH abundance in a more systematic fashion. Their study introduced the $R_{\rm PAH}$ metric, defined as the ratio between PAH-dominated mid-IR bands (e.g., F1130W) and the total dust continuum (e.g., F2100W). A higher $R_{\rm PAH}$ indicates a larger relative contribution from PAHs compared to the overall dust emission, while a lower ratio suggests depletion or destruction of PAH grains. This provides an observational proxy for the PAH mass fraction that is sensitive to local processing by shocks and radiation fields, making it a useful diagnostic even for non-specialists.

When averaged over circular apertures of 50 pc diameter, Egorov et al. (2025) found that $R_{\rm PAH}$ at SNR locations is statistically indistinguishable from random control regions across the galaxy disks. Only after applying a careful local background subtraction did they detect subtle residual trends: approximately 65% of SNRs showed mildly suppressed $R_{\rm PAH}$ values, suggesting that some PAH destruction may be occurring, but the effect is modest and often masked by spatial averaging or local emission complexity.

These results imply that SN shocks do not dramatically alter the global PAH budget in star-forming galaxies. Instead, their effects are likely confined to localized, low-contrast regions that require high-resolution imaging and differential background modeling to detect. Our own findings, showing a lack of obvious PAH contrast at SNR positions, independently support this conclusion.

Taken together, these studies suggest that while PAH destruction by SN shocks is theoretically plausible and weakly supported observationally, it is unlikely to account for the galaxy-wide trends between metallicity and PAH abundance seen in integrated measurements. Further constraints will require higher-resolution, background-subtracted spectral mapping of individual SNRs—ideally combining mid-IR, optical, and millimeter observations to trace both dust and gas-phase shock diagnostics.

4.3 HST IMAGING OF SUPERNOVA REMNANTS

High-resolution imaging from the Hubble Space Telescope (HST) provides a unique opportunity to study the structural and environmental properties of supernova remnants (SNRs) at sub-arcsecond scales. In this exploratory work, we combine both broadband and narrowband HST imaging for a subset of optically identified, isolated SNRs from Li et al. (2024). The broadband photometry is particularly useful for constraining stellar clusters and young populations near the remnants, while the narrowband Hα and [S II] filters trace nebular emission from shocked gas. Together, these datasets allow us to probe (1) the spatial relationship between SNRs and possible natal star clusters, (2) the size–luminosity distribution of SNRs from HST Hα morphology, and (3) the electron densities inferred from [S II] line ratios.

4.3.1 *SNR Progenitor Environments and Stellar Cluster Association*

Figure 28a and Figure 28b quantify the projected separations between our optically selected SNRs and catalogued young stellar clusters from Maschmann et al. (2024). In both cases, the distributions show that most remnants are located tens to hundreds of parsecs away from the nearest compact cluster or stellar association, with median offsets far larger than the ∼5–10 pc expected if progenitors had exploded in situ. These quantitative trends are consistent with the visual impression from HST imaging that only a small fraction of SNRs coincide with nearby compact clusters within a few parsecs. Instead, the majority resemble the "dispersed" or "delayed" core-collapse events predicted by binary-evolution models (Wagg et al. 2025; Zapartas et al. 2017), and the offset distributions observed for massive stars and SNRs in atomic-dominated intercloud regions of M33 (Sarbadhicary et al. 2023). The measured separations therefore reinforce the view that many progenitors either formed in loose OB associations, were dynamically ejected from clusters (Oh & Kroupa 2016), or that their natal clusters dissolved on Myr timescales (Krause et al. 2016; Oh, Kroupa & Pflamm-Altenburg 2015).

4.3.2 *Hα Size–Luminosity Relation from HST Imaging*

We next examined the structural properties of SNRs in HST narrowband imaging. For this analysis, we matched our catalog to the compilation of HST-resolved SNRs from Barnes et al. (2025), which provides a homogeneous catalog of nebular sources across PHANGS–HST galaxies. Their work includes visual classifications as well as quantitative measurements of SNR diameters, surface brightnesses, and complexity scores based on WFC3 and ACS narrowband Hα images. These data allow us to compare ground-based MUSE identifications with space-based structural measurements.

In total, we identified ∼150 isolated SNRs with available HST Hα imaging. Figure 29 shows their surface brightness as a function of physical diameter. The distribution reveals large scatter, with no clear correlation between size and luminosity in our heterogeneous sample. This lack of a trend reflects both physical diversity and observational challenges. In particular, reconciling the exquisite HST resolution (0.1) with ground-based IFU data (∼1) is non-trivial: MUSE often blends SNR emission with nearby H II regions, whereas HST resolves detailed shell morphologies. Consequently, direct comparisons of size and flux across the two datasets must be treated with caution.

Theoretically, younger SNRs expanding into dense media should appear compact and luminous, while older remnants fade and expand as radiative losses dominate (Chevalier 1974). Such a trend has been observed in well-studied individual galaxies, such as M83, where Blair et al. (2014) report a clear anti-correlation between size and Hα luminosity. By contrast, in our cross-galaxy sample, spanning multiple environments and variable image depth, this trend disappears, leaving only broad scatter. This difference underscores the difficulty of recovering evolutionary relations from heterogeneous extragalactic samples, and highlights the importance of uniform, deep surveys for constraining SNR evolution.

Future directions: To refine these results, it will be important to combine the morphological complexity scoring of Barnes et al. (2025) with environmental information (e.g., molecular gas, stellar population ages), and to place our cross-galaxy sample in context with homogeneous studies of individual galaxies such as M83. Adding JWST mid-IR morphologies will also provide complementary dust-sensitive diagnostics that may correlate with size and luminosity.

4.3.3 *[S II] Line Ratios and Electron Density Estimates*

Finally, we explored the physical conditions of SNRs using HST [S II] imaging. The flux ratio of [S II]$\lambda6716/\lambda6730$ serves as a classic diagnostic of electron density, sensitive to the range 10–10,000 cm^{-3}. Using aperture photometry, we measured this ratio for 78 isolated remnants with sufficient signal-to-noise.

Figure 30 shows the inferred [S II] ratio as a function of physical diameter. Most SNRs fall in the 50–300 cm^{-3} range, with no strong correlation between density and size. This suggests that local ISM variations dominate over remnant age in setting the emitting density. A handful of compact SNRs exhibit elevated densities ($n_e > 500\ \mathrm{cm}^{-3}$), consistent with interactions with circumstellar material or dense ISM clumps, while the lowest-density objects may represent remnants expanding into evacuated or diffuse environments.

Caveats and Next Steps: The HST imaging provides exquisite structural detail, but several challenges remain. First, cross-matching with ground-based IFU data is hindered by resolution differences and blending with nearby nebular emission. Second, visual classification of SNRs in crowded star-forming regions remains subjective. Third, the size–luminosity relation is strongly affected by selection effects, and robust evolutionary trends require homogeneous, galaxy-specific studies. Future progress will benefit from combining HST optical imaging with JWST mid-IR maps and ALMA molecular gas data, enabling a multi-phase characterization of how SNRs evolve with their environments.

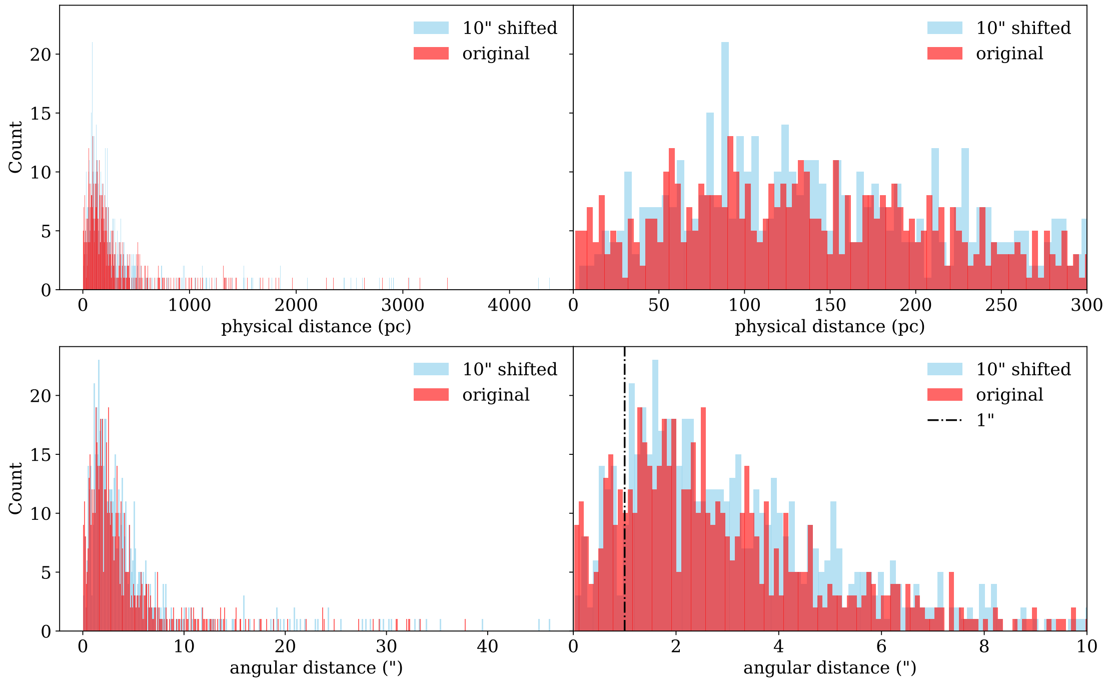

(a) Compact Clusters.

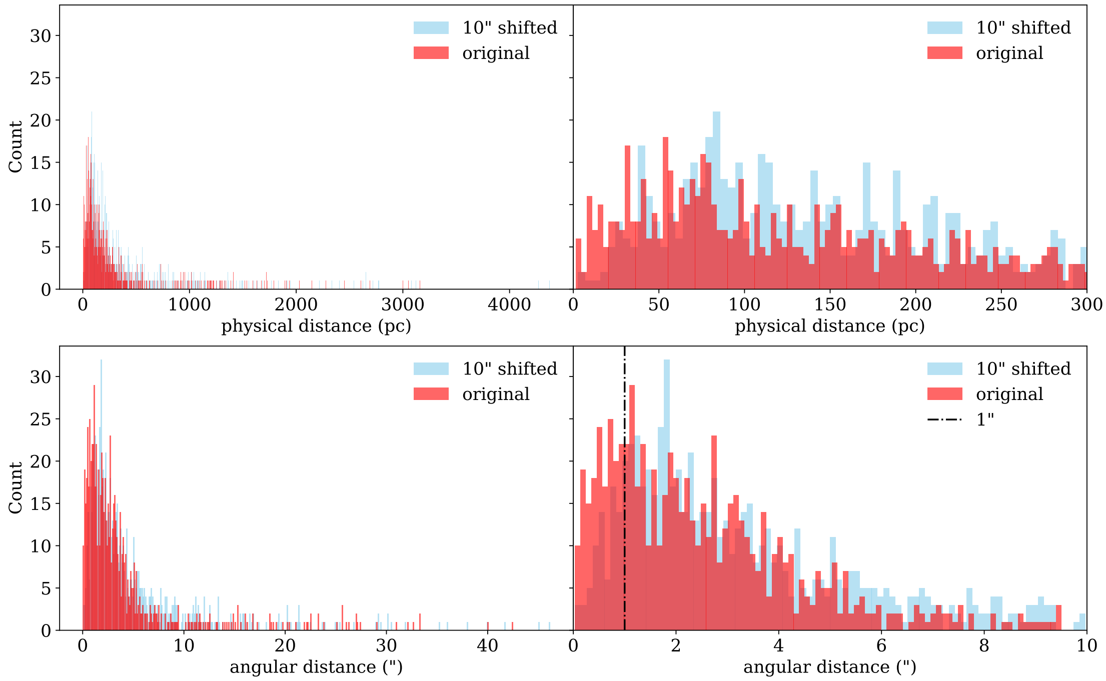

(b) Stellar Associations.

Figure 28: Projected distances between SNRs and the nearest compact cluster (a) and stellar association (b) from Maschmann et al. (2024). Both distributions show that most SNRs lie well beyond a few parsecs, implying that only a minority of progenitors exploded in situ.

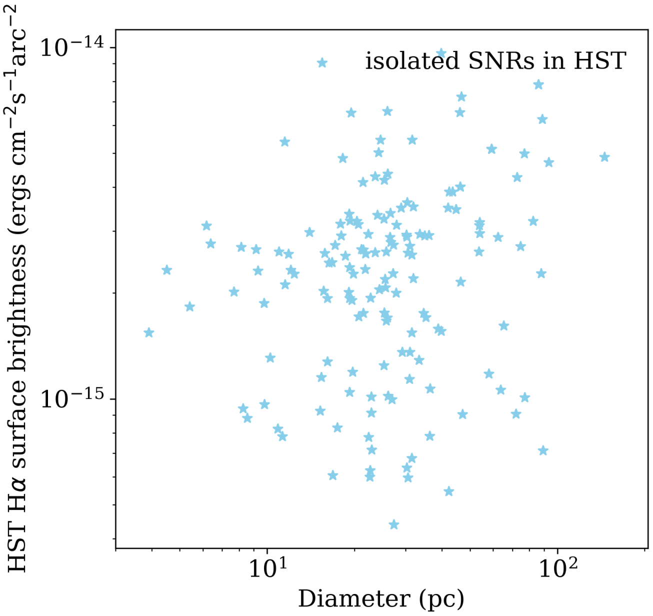

Figure 29: Hα surface brightness versus physical diameter for isolated SNRs detected in HST narrowband imaging. While models predict that younger, denser remnants should be compact and bright, and older remnants larger and fainter, our heterogeneous sample shows only scatter, likely due to environmental variation and observational biases.

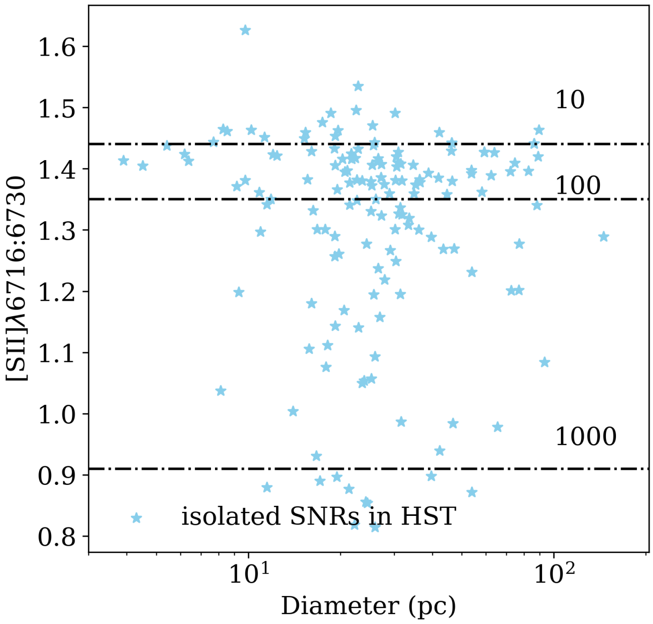

Figure 30: [S II]λ6716/λ6730 ratio as a function of SNR diameter, with dashed lines corresponding to electron densities of 10, 100, and 1000 cm^{-3}. Most SNRs lie in the 50–300 cm^{-3} range, with outliers tracing unusually dense or diffuse environments.

Part III

SUMMARY

5

SUMMARY

Supernova remnants (SNRs) are key drivers of the evolution of the interstellar medium (ISM) in galaxies. As the end products of core-collapse and thermonuclear supernova explosions, they inject kinetic energy, momentum, and chemically enriched material into their surroundings. This process shapes the thermal and dynamical state of the ISM, regulates star formation, and contributes to the redistribution of metals within and between galaxies. Understanding the demographics and environments of SNRs is therefore essential for building a complete picture of stellar feedback and its role in galaxy evolution.

Historically, SNR studies have been limited by sample size, observational biases, and heterogeneous detection methods. While hundreds of SNRs have been identified in the Milky Way and Magellanic Clouds via multi-wavelength campaigns, systematic surveys of external galaxies have often been shallow or restricted in host galaxy properties. In particular, the connection between SNR occurrence and local ISM metallicity has remained poorly constrained at sub-kpc resolution.

This thesis aims to address these gaps by (1) conducting the largest uniform spectroscopic survey of SNRs in nearby star-forming galaxies, and (2) investigating the metallicity environments of these SNRs using high-spatial-resolution emission-line mapping. By combining optical integral field spectroscopy with multi-wavelength data, this work advances our empirical understanding of SNR populations and their role in the ISM.

5.1 MAIN RESULTS

5.1.1 *A census of ~2200 new SNR candidates*

In Chapter 2 (Li et al. 2024), I present the discovery of 2,233 SNR candidates in 19 nearby star-forming galaxies using MUSE integral field spectroscopy. The identification relied on five emission-line diagnostics applied uniformly across the sample, enabling unprecedented completeness and comparability between galaxies. This catalog more than doubles the known extragalactic SNR population and spans a diverse range of host galaxy morphologies and ISM conditions.

This work demonstrates the power of large-scale, high-resolution IFS surveys in resolving individual SNRs in crowded star-forming environments, overcoming many of the limitations of traditional narrowband imaging techniques.

5.1.2 *Metallicity environments of SNRs*

Chapter 3 (to be submitted to A&A) investigates the sub-kpc metallicity environments of SNRs in star-forming galaxies. Because direct abundance determinations from SNR spectra are hampered by shock excitation, I used nearby H II region spectra to estimate local gas-phase metallicity via strong-line calibrations.

I find no significant difference between the oxygen abundances at SNR locations and those in the general H II region population. This result suggests that SNRs trace the typical sites of massive star formation, and that metallicity does not play a dominant role in influencing observable SNR incidence within the parameter space probed by PHANGS–MUSE.

5.1.3 *Multi-wavelength exploratory studies*

To supplement the optical analysis, I performed exploratory studies of the SNR population using archival data from ALMA, Chandra, JWST, and HST:

- **ALMA:** SNRs are preferentially located in regions of moderate molecular gas surface density, broadly consistent with the environments of Type II SNe. This implies that most of our remnants are linked to massive stars exploding outside the densest, still-embedded clouds.
- **JWST:** Mid-infrared imaging shows only weak evidence for local PAH suppression at SNR sites, suggesting that SN shocks are not a dominant mechanism for PAH destruction on 50 pc scales. This constrains the role of SNRs in dust processing.
- **HST:** High-resolution Hα and [S II] imaging reveals a wide range of diameters and electron densities, but no tight size–luminosity correlation. This indicates that ISM density variations and projection effects dominate over a single evolutionary sequence.

Together, these multi-wavelength results provide specific physical insights into SNR environments, complementing the optical catalog and metallicity analysis.

5.2 SIGNIFICANCE

The results presented in this thesis establish a new observational baseline for understanding the role of SNRs in galaxy evolution. The large, uniformly selected catalog enables demographic studies across diverse galactic environments. The metallicity analysis provides the first systematic test of whether local chemical composition influences SNR occurrence. The multi-wavelength pilot studies demonstrate how optical

IFS can be integrated with targeted follow-up to constrain molecular gas coupling, dust destruction, and hot plasma formation.

This work is timely in the era of PHANGS–MUSE, PHANGS–ALMA, PHANGS–JWST, and PHANGS–HST surveys, and anticipates the capabilities of next-generation facilities such as BlueMUSE, SKA, JWST spectroscopy, and Athena.

5.3 LIMITATIONS

Despite the advances presented here, several limitations remain:

- Optical diagnostics may miss faint or atypical SNRs, especially older or low-surface-brightness remnants.
- Metallicity estimates rely on the assumption that nearby H II regions reflect pre-SN ISM composition, which may be invalid in cases of local enrichment or turbulent mixing.
- The multi-wavelength coverage is heterogeneous and limited to a subset of galaxies, preventing robust statistical conclusions about dust or hot gas properties.

Future progress requires deeper observations, improved identification techniques, and coordinated multi-wavelength campaigns.

5.4 FUTURE DIRECTIONS

5.4.1 *Expanded IFS surveys*

Next-generation instruments such as **BlueMUSE** on the VLT will extend spectral coverage to ~3500Å, providing access to temperature-sensitive lines ([O II] and [O III]λ4363). These will allow direct T_e-based abundances, improving metallicity estimates and separating shock-excited from photoionized gas. BlueMUSE will also reach lower-metallicity outer disks and dwarf galaxies, currently missing from PHANGS.

5.4.2 *Multi-wavelength integration*

Coordinated follow-up with new facilities will probe missing ISM phases:

- **ALMA:** deeper mosaics can quantify cloud disruption efficiency and test whether SNR shocks trigger or quench star formation.
- **SKA:** radio synchrotron emission will reveal faint, older SNRs, constraining the SNR visibility lifetime and filling in the age distribution of remnants.

- **JWST:** spectroscopy of PAH bands and [Fe II] lines will directly measure dust destruction and shock excitation at parsec scales.
- **Athena:** high-resolution X-ray spectroscopy will quantify shock temperatures, thermal energy content, and metal abundances in hot gas, determining how much energy and enrichment remains in galactic disks versus escapes to halos.

5.4.3 *Linking to theory and simulations*

The measurements presented here can be compared with simulations of SN feedback:

- **SILCC** (Walch et al. 2015) and **TIGRESS** (Kim & Ostriker 2017) model clustered SNe in stratified galactic disks.
- **FIRE-2** (Hopkins et al. 2018) incorporates sub-grid SN feedback in cosmological galaxy simulations.

Our resolved demographics constrain where SNe explode relative to gas phases, how momentum couples to the ISM, and how metals mix on ~100 pc scales, providing key tests for these models.

5.5 CONCLUSION

This thesis significantly enlarges the extragalactic SNR sample, provides the first galaxy-wide metallicity environment study of SNRs, and demonstrates the potential of combining optical and multi-wavelength data to characterize stellar feedback. The findings lay the groundwork for future studies of SNRs as essential agents in galaxy evolution, linking massive stars to their host environments in nearby galaxies.

As new facilities come online, we will be able to map the life cycle of SNRs across wider galaxy populations and physical regimes. The results presented here serve as a foundation for those efforts, ensuring that SNRs are recognized not only as remnants of past explosions, but as dynamic, measurable tracers of stellar feedback in the evolving universe.

Part IV

APPENDIX

A

APPENDIX FOR CHAPTER 2

A.1 MASKED REGIONS WITHIN EACH GALAXY

Environmental masks that applied to each criterion for 19 galaxies are described in Table A.1. Environment masks are defined in Querejeta et al. (2021), 1 is center mask, 2 is bar mask, 3 is bar ends mask, and 9 is interbar mask. They are applied to avoid over-selecting shocked regions around the center or along the stellar bar. For NGC 1566 and NGC 3351, their center is not sufficient to cover the above shocked regions, so the convolved mask of center and bar masks were applied, with corresponding Gaussian kernels as listed.

A.2 ATLAS OF SUPERNOVA REMNANT LOCATIONS IN PHANGS-MUSE GALAXIES

A total of 2233 objects are identified in 19 PHANGS-MUSE galaxies; only three of them are shown in Fig. 9. The remaining 16 galaxies are shown in Figs. 31-34. They display the distribution of identified objects across different galaxies.

Table A.1: Environmental masks applied to each criterion for 19 galaxies.

gname	OI residual	SII residual	σ(SII)	BPT_OI	BPT_SII	comments
IC 5332	1	1	1	1	1	
NGC 628	1	1	1	1	1	
NGC 1087	2&9	2&9	2&9	2&9	2&9	
NGC 1300	1&2	1&2	1	1	1	
NGC 1365	1&2	1&2	1&2	1&2	1&2	
NGC 1385	-	-	-	-	-	
NGC 1433	1	1&2	1	1	1	
NGC 1512	1	1&2	1	1	1	
NGC 1566	conv(1&2)	conv(1&2)	conv(1&2)	conv(1&2)	conv(1&2)	kernel1
NGC 1672	1&2	1&2	1&2	1&2	1&2	
NGC 2835	1	1	1	1	1	
NGC 3351	conv(1&2)	conv(1&2)	conv(1&2)	conv(1&2)	conv(1&2)	kernel2
NGC 3627	1&2&3	1&2&3	1&2&3	1&2&3	1&2&3	
NGC 4254	1	1	1	1	1	
NGC 4303	1	1	1	1	1	
NGC 4321	1	1	1	1	1	
NGC 4535	1	1	1	1	1	
NGC 5068	1	1	1	1	1	
NGC 7496	1&2	1&2	1&2	1&2	1&2	

Notes. Environment masks are defined in Querejeta et al. (2021), 1 is center mask, 2 is bar mask, 3 is bar ends mask, and 9 is interbar mask. The Gaussian kernels for convolved masks are:

Kernal1= Gaussian2DKernel(x_stddev=5), conv = convolve(env_masks.data, kernel).

Kernel2 = Gaussian2DKernel(x_stddev=10), conv = convolve(env_masks.data, kernel).

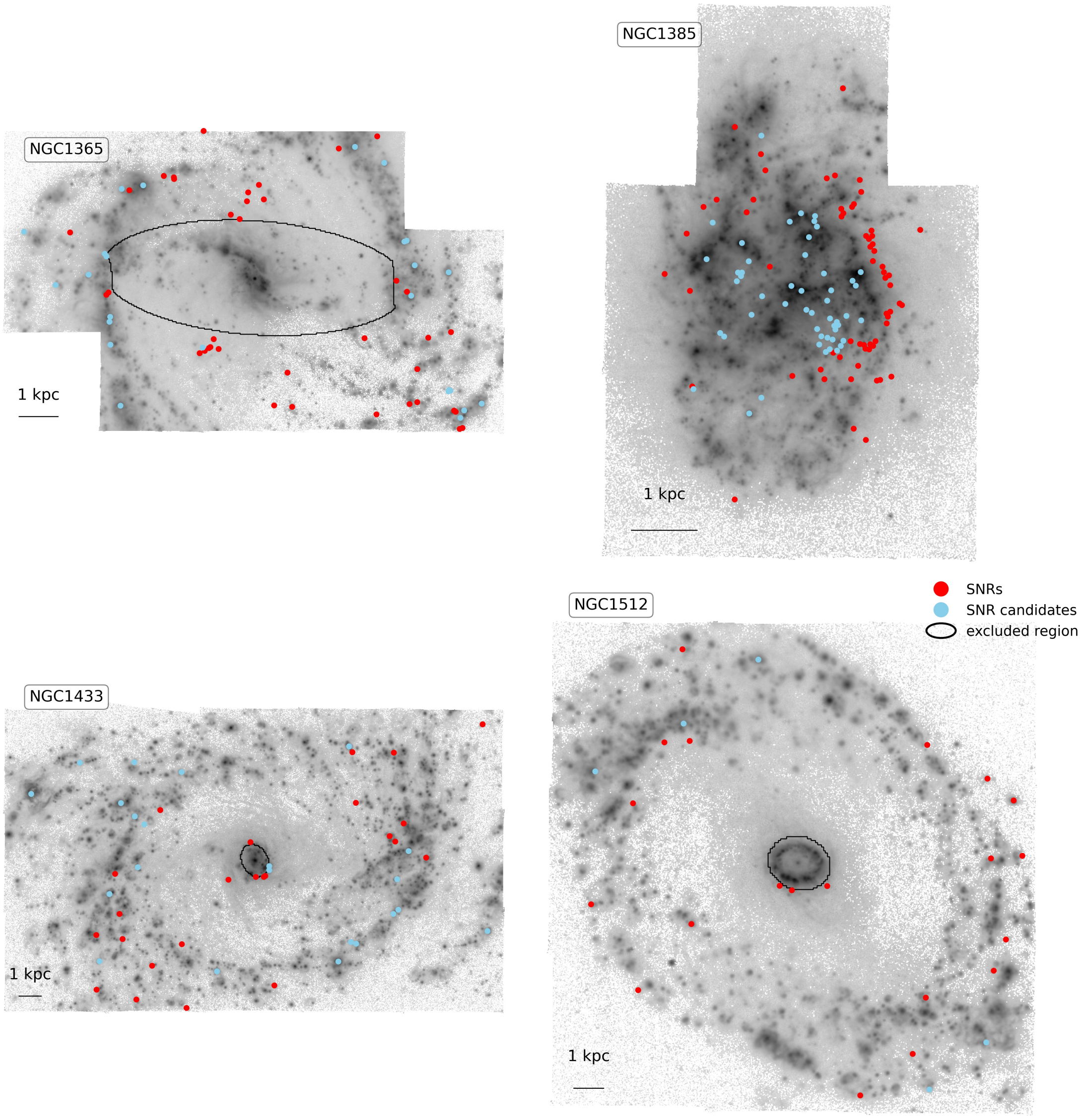
NGC1365
1 kpc
NGC1385
1 kpc
NGC1512
● SNRs
● SNR candidates
excluded region
NGC1433
1 kpc
1 kpc

Figure 31: Same as in Fig. 9.

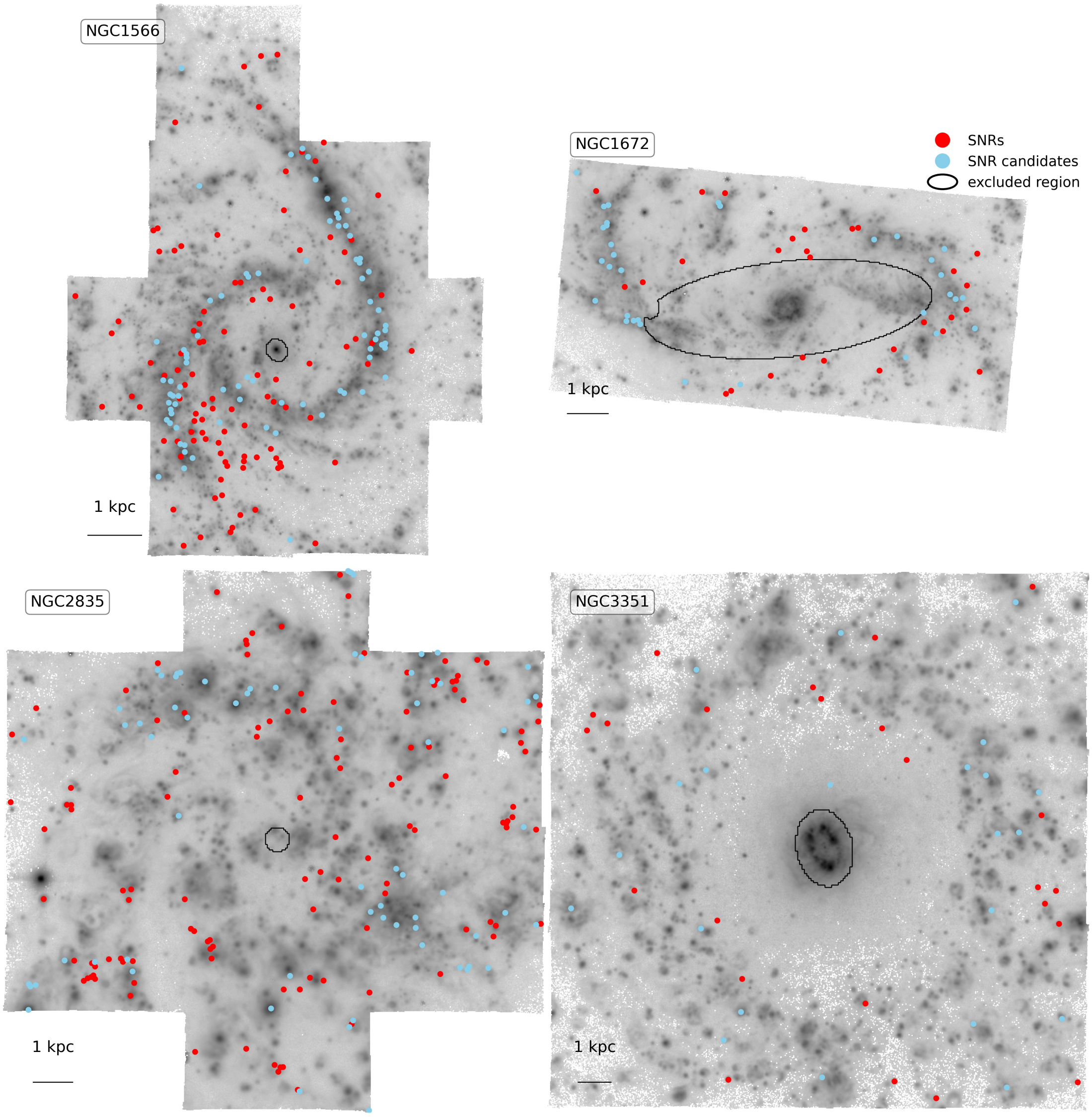

Figure 32: Same as in Fig. 9.

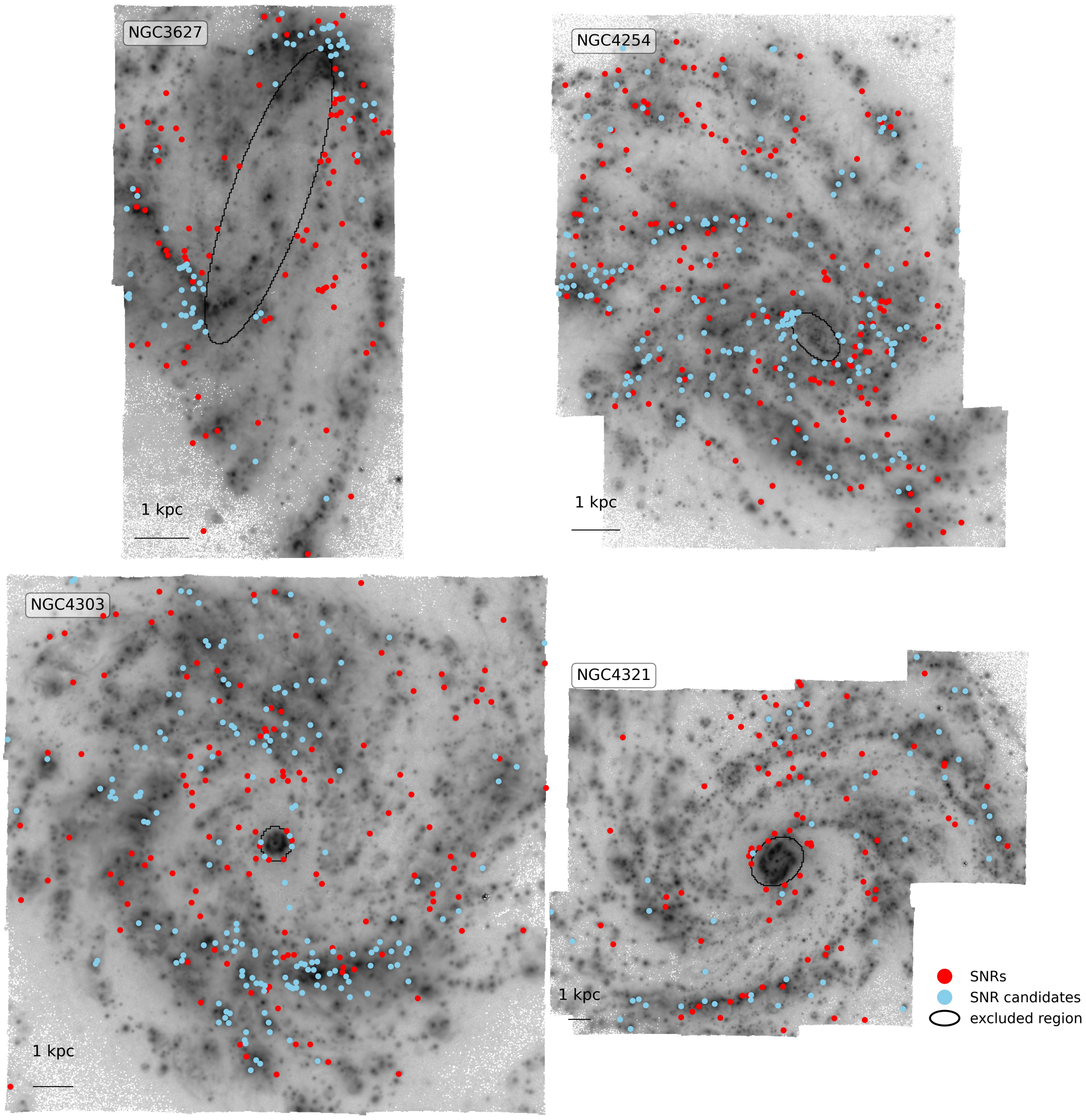
NGC3627
1 kpc
NGC4254
1 kpc
NGC4303
1 kpc
NGC4321
1 kpc
SNRs
SNR candidates
excluded region

Figure 33: Same as in Fig. 9.

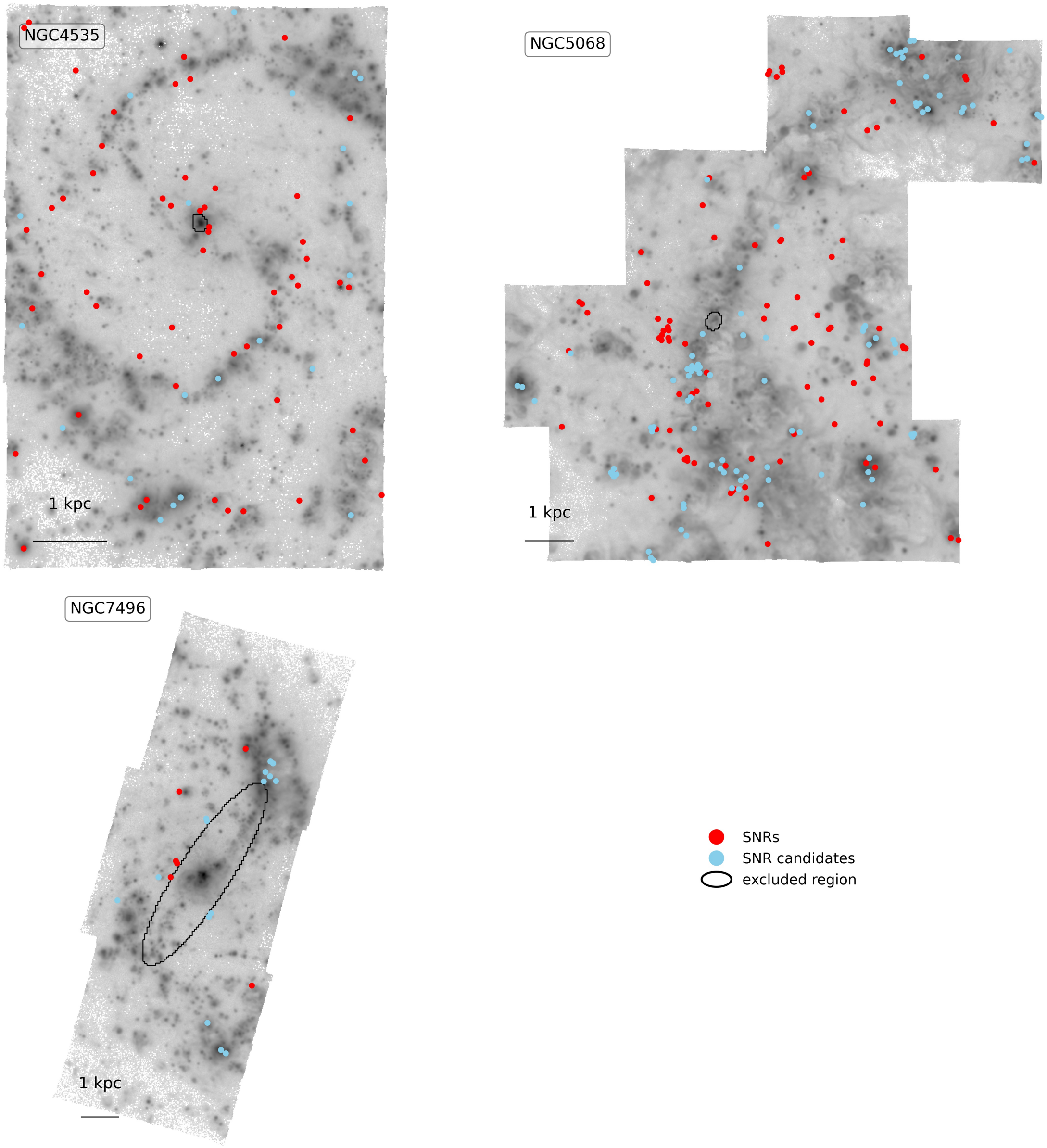
NGC4535
1 kpc
NGC5068
1 kpc
NGC7496
1 kpc
SNRs
SNR candidates
excluded region

Figure 34: Same as in Fig. 9.

A.3 FITTED EMISSION LINES AND MASKED SKY LINES WHILE RUNNING THE DATA ANALYSIS PIPELINE.

In Table A.2, we listed the fitted emission lines, sky lines that have been masked, ISM absorption regions that need to be masked while running the data analysis pipeline in the first column. Not all lines are fitted independently, their kinematic dependency is shown in the second column.

A.4 CATALOG OF OBJECTS IDENTIFIED IN M83

In Sect. 2.3.3 we validate our method by applying it to archival MUSE observations of M83. The galaxy is two to four times closer (D = 4.61 Mpc; Saha et al. 2006) than galaxies in our PHANGS-MUSE sample, and the line maps and line kinematic maps used are taken from Della Bruna et al. 2022, which used a different approach to line fitting and spatial binning. For these reasons, we do not consider this catalog completely equivalent to what was produced for the PHANGS-MUSE galaxies, but we provide part of the object locations and classifications (SNR or SNR candidate) for all 125 objects in the Table A.4. The full table is available in electronic form at the CDS via anonymous ftp to `cdsarc.u-strasbg.fr` (130.79.128.5) or via `http://cdsweb.u-strasbg.fr/cgi-bin/qcat?J/A+A/`.

Table A.2: Fitted emission lines and masked sky lines while running DAP.

Line name	Dependency
Forbidden and recombination emission lines	
He IIλ4685.70	kinematics depend on [O III]λ5006.84
Hβλ4861.35	kinematics depend on Hαλ6562.79
[O III]λ4958.91	kinematics and amplitude depend on [O III]λ5006.84
[O III]λ5006.84	None
[N I]λ5197.90	kinematics depend on [N II]λ6583.45
[N I]λ5200.26	kinematics depend on [N II]λ6583.45
[N II]λ5754.59	kinematics depend on [N II]λ6583.45
He Iλ5875.61	kinematics depend on Hαλ6562.79
[O I]λ6300.30	kinematics depend on [N II]λ6583.45
[S III]λ6312.06	kinematics depend on [O III]λ5006.84
[O I]λ6363.78	kinematics and amplitude depend on [O I]λ6300.30
[N II]λ6548.05	kinematics and amplitude depend on [N II]λ6583.45
Hαλ6562.79	None
[N II]λ6583.45	None
[S II]λ6716.44	kinematics depend on [N II]λ6583.45
[S II]λ6730.82	kinematics depend on [N II]λ6583.45
HPaschen 11λ8862.89	kinematics depend on Hαλ6562.79
[S III]λ9068.6	kinematics depend on [O III]λ5006.84
Masked lines	
He Iλ6678.15	kinematics depend on Hαλ6562.79
Sky lines are fitted and used to remove sky emission	
λ5577.34	
λ6300.30	
λ6363.78	
Masked regions due to the ISM absorption	
Na Iλ5889.95	
Na Iλ5895.92	

Table A.3: Identified objects in M83 (part).

RA	DEC	OI residual	SII residual	σ(SII)	BPT_OI	BPT_SII	match
204.2644509	-29.90044891	TRUE	FALSE	FALSE	FALSE	FALSE	1
204.2684764	-29.89644006	TRUE	TRUE	FALSE	FALSE	FALSE	2
204.2217992	-29.89035411	TRUE	FALSE	FALSE	TRUE	FALSE	2
204.2794457	-29.88916123	TRUE	TRUE	FALSE	TRUE	TRUE	4
204.2300562	-29.88472005	TRUE	TRUE	FALSE	TRUE	FALSE	3
204.2294845	-29.8846112	TRUE	TRUE	TRUE	TRUE	FALSE	4
204.2317025	-29.884343	TRUE	TRUE	TRUE	FALSE	FALSE	3
204.2311406	-29.88429423	TRUE	FALSE	FALSE	FALSE	TRUE	2
204.2411654	-29.8840859	TRUE	TRUE	TRUE	TRUE	FALSE	4
204.2458424	-29.88369318	TRUE	TRUE	FALSE	FALSE	FALSE	2
204.2146209	-29.88367883	TRUE	FALSE	FALSE	FALSE	FALSE	1
204.2121447	-29.88300623	TRUE	TRUE	FALSE	FALSE	FALSE	2
204.2342854	-29.88199423	TRUE	TRUE	FALSE	FALSE	FALSE	2
204.2219733	-29.8800032	TRUE	TRUE	FALSE	TRUE	TRUE	4
204.2095214	-29.8797877	TRUE	TRUE	FALSE	FALSE	FALSE	2
204.2234408	-29.87949562	TRUE	TRUE	TRUE	TRUE	TRUE	5
204.2311919	-29.87875809	TRUE	TRUE	FALSE	TRUE	TRUE	4
204.2221012	-29.8784649	TRUE	TRUE	FALSE	FALSE	FALSE	2
204.2135546	-29.87803204	TRUE	FALSE	FALSE	FALSE	FALSE	1
204.2293475	-29.87765827	TRUE	TRUE	TRUE	FALSE	TRUE	4
204.2119211	-29.87767374	TRUE	TRUE	FALSE	TRUE	FALSE	3
204.2994947	-29.87094228	TRUE	TRUE	TRUE	TRUE	TRUE	5
204.2256829	-29.86925442	TRUE	TRUE	FALSE	FALSE	TRUE	3
204.250294	-29.86908168	TRUE	TRUE	FALSE	TRUE	TRUE	4
204.2509311	-29.86839083	TRUE	TRUE	TRUE	TRUE	TRUE	5
204.2479135	-29.86776394	TRUE	TRUE	TRUE	TRUE	TRUE	5
204.2854061	-29.86719197	TRUE	TRUE	FALSE	FALSE	FALSE	2
204.2501895	-29.86712891	TRUE	TRUE	FALSE	FALSE	FALSE	2
204.2586728	-29.86621778	TRUE	TRUE	TRUE	TRUE	TRUE	5
204.2859831	-29.86485631	TRUE	TRUE	FALSE	FALSE	FALSE	2
204.2977868	-29.86147724	TRUE	TRUE	TRUE	TRUE	TRUE	5
204.3044806	-29.86067448	TRUE	TRUE	FALSE	FALSE	FALSE	2
204.285712	-29.85975022	TRUE	TRUE	TRUE	TRUE	TRUE	5
204.2811515	-29.85925031	TRUE	TRUE	TRUE	TRUE	TRUE	5
204.2919771	-29.85782428	TRUE	TRUE	FALSE	FALSE	FALSE	2

Table A.4: Identified objects in M83 (continued).

RA	DEC	OI residual	SII residual	σ(SII)	BPT_OI	BPT_SII	match
204.2600849	-29.85723198	TRUE	TRUE	FALSE	TRUE	TRUE	4
204.2833441	-29.85453299	TRUE	FALSE	FALSE	FALSE	FALSE	1
204.2571478	-29.85368573	TRUE	TRUE	TRUE	TRUE	TRUE	5
204.2820262	-29.85278978	TRUE	FALSE	FALSE	FALSE	FALSE	1
204.2299161	-29.84480477	TRUE	TRUE	FALSE	TRUE	FALSE	3
204.229708	-29.84459285	TRUE	FALSE	FALSE	FALSE	TRUE	2
204.226026	-29.8411766	TRUE	TRUE	TRUE	TRUE	FALSE	4
204.2271069	-29.84061925	TRUE	TRUE	FALSE	FALSE	FALSE	2
204.2768417	-29.84028213	TRUE	TRUE	FALSE	TRUE	TRUE	4
204.2286799	-29.83850856	TRUE	TRUE	FALSE	TRUE	TRUE	4
204.2570585	-29.90280692	FALSE	TRUE	FALSE	TRUE	TRUE	3
204.2669936	-29.90066473	FALSE	TRUE	FALSE	FALSE	FALSE	1
204.2420095	-29.89587097	FALSE	TRUE	FALSE	FALSE	FALSE	1
204.2604374	-29.89571024	FALSE	TRUE	FALSE	FALSE	FALSE	1
204.2310394	-29.89468833	FALSE	TRUE	FALSE	FALSE	FALSE	1
204.27771	-29.89289502	FALSE	TRUE	FALSE	FALSE	FALSE	1
204.2381533	-29.89269151	FALSE	TRUE	FALSE	TRUE	TRUE	3
204.2499832	-29.88996355	FALSE	TRUE	FALSE	FALSE	FALSE	1
204.2516662	-29.88972639	FALSE	TRUE	FALSE	FALSE	FALSE	1
204.2671822	-29.88784274	FALSE	TRUE	FALSE	FALSE	FALSE	1
204.2820848	-29.88374798	FALSE	TRUE	FALSE	FALSE	FALSE	1
204.230436	-29.88153219	FALSE	TRUE	FALSE	FALSE	TRUE	2
...	...	...	...	...	...	...	...

Notes. The whole table is available in electronic form at the CDS via anonymous ftp to `cdsarc.u-strasbg.fr` (130.79.128.5) or via `http://cdsweb.u-strasbg.fr/cgi-bin/qcat?J/A+A/`.

B

APPENDIX FOR CHAPTER 3

B.1 METALLICITY IN D16 CALIBRATION

The metallicity measurements used throughout this paper are based on the calibration from Groves et al. (2023). However, to enable a direct comparison with the results of Pessi et al. (2023), we also recompute the metallicity using the D16 calibration as defined by Dopita et al. (2016). The corresponding figures for this comparison are presented below:

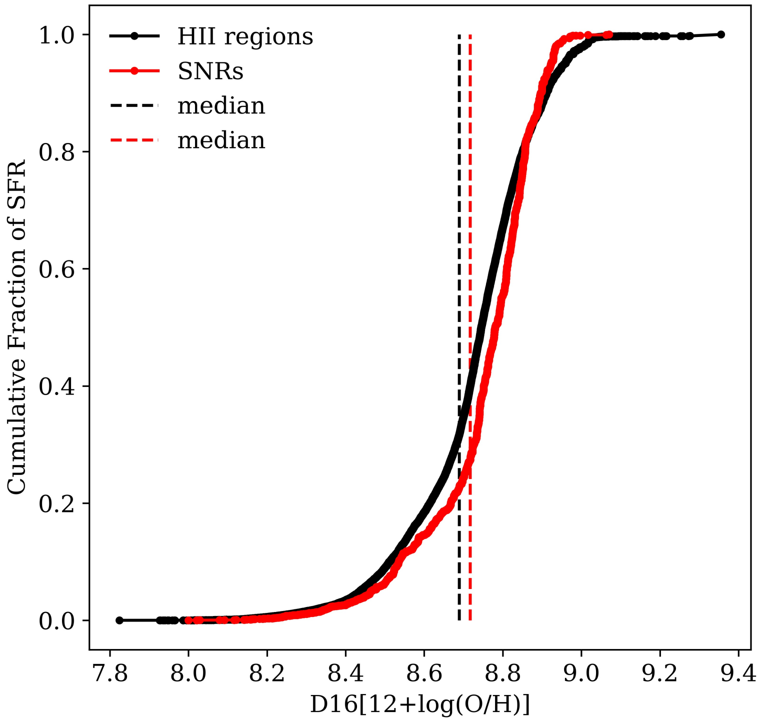

Figure 35: Cumulative distribution of SFR as a function of D16 metallicity ([O/H]). The black line shows all H II regions in the 19 galaxies, while the red line corresponds to H II regions close to SNRs. Dashed lines mark the median metallicity of each population.

Figure 35 shows that the median D16 metallicity of H II regions associated with SNRs is only slightly higher (by ~0.02 dex) than the overall distribution. This difference is negligible, suggesting that SNRs are not preferentially located in regions with significantly different metallicity.

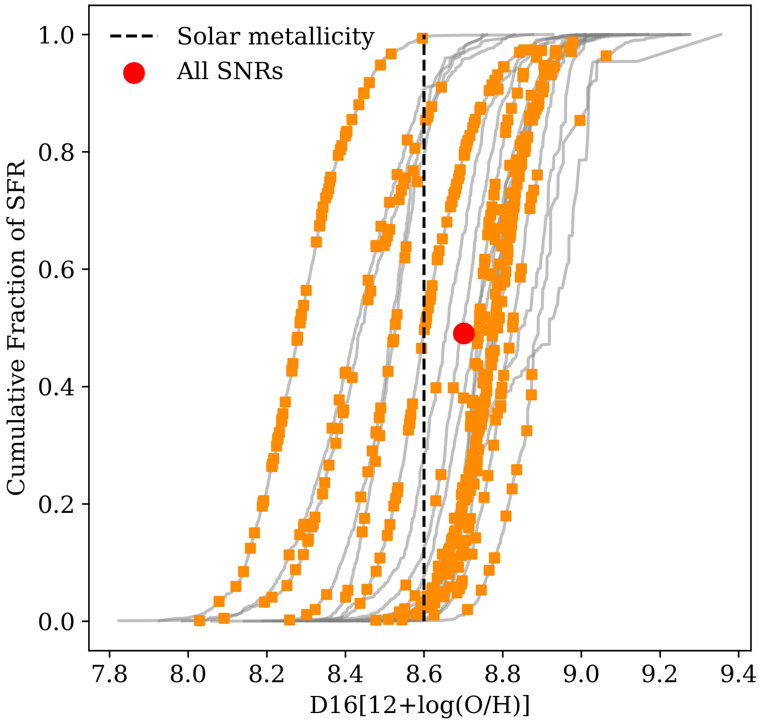

Figure 36: Cumulative distributions of SFR fraction as a function of [O/H] for individual galaxies using the D16 calibration. Each gray line represents one galaxy. Orange squares indicate the [O/H] values and relative SFR ranks of H II regions near SNRs. The red dot marks the median of the entire SNR-associated H II region sample. The dashed black line at $12 + \log_{10}(O/H) = 8.6$ dex indicates a commonly used threshold for high metallicity (solar).

As shown in Fig. 36, the metallicity of H II regions associated with SNRs spans the full range observed in each galaxy, with no apparent bias toward particularly metal-rich or metal-poor environments.

In Fig. 37, we observe that the distribution of SNR frequency across metallicity bins remains broadly consistent with the main analysis. The metallicity range of H II regions in our dataset spans 8.0 to 9.2 dex, while Pessi et al. (2023) reports a slightly narrower range of 7.6 to 9.0. This results in the absence of the leftmost bin used in their study and the inclusion of an additional bin at the high-metallicity end in ours.

The number of SNRs in each bin, which determines the Poisson uncertainty in the y-axis, is as follows: [12, 69, 87, 250, 119]. The first bin is particularly underpopulated, with only one SNR. This is partly due to our high-mass star-forming galaxy sample.

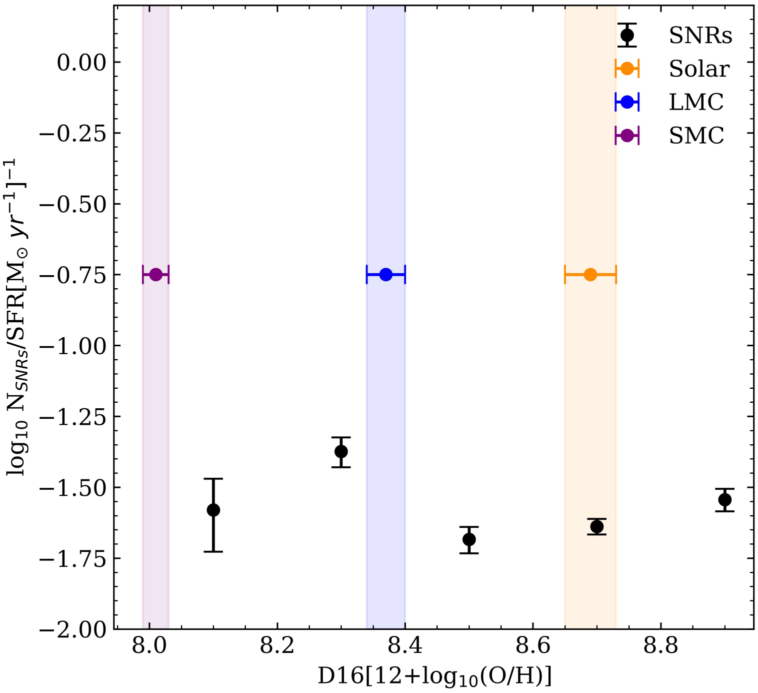

Figure 37: SNR occurrence per unit SFR as a function of [O/H], binned in 0.2 dex intervals using the D16 metallicity calibration. The y-axis shows the number of SNRs divided by the total SFR within each metallicity bin. This is the same as Fig. 25, but with metallicity derived using the D16 calibration.

C

APPENDIX FOR CHAPTER 4

Here we present RGB composite images of 19 PHANGS–MUSE galaxies, with red representing Hα emission, green showing [S II] emission, and blue corresponding to [O III] emission.

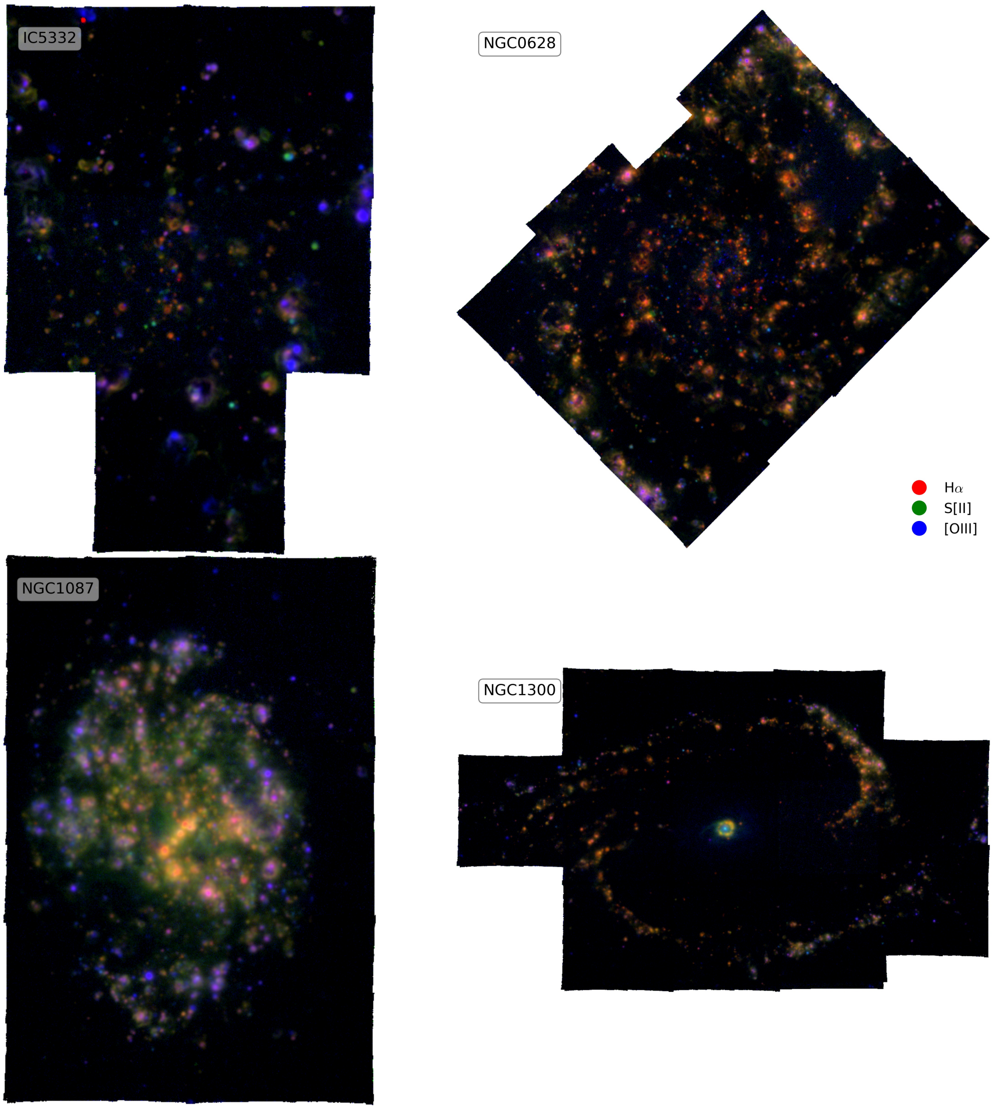
IC5332
NGC0628
Hα
S[II]
[OIII]
NGC1087
NGC1300

Figure 38: RGB images for 19 PHANGS-MUSE galaxies.

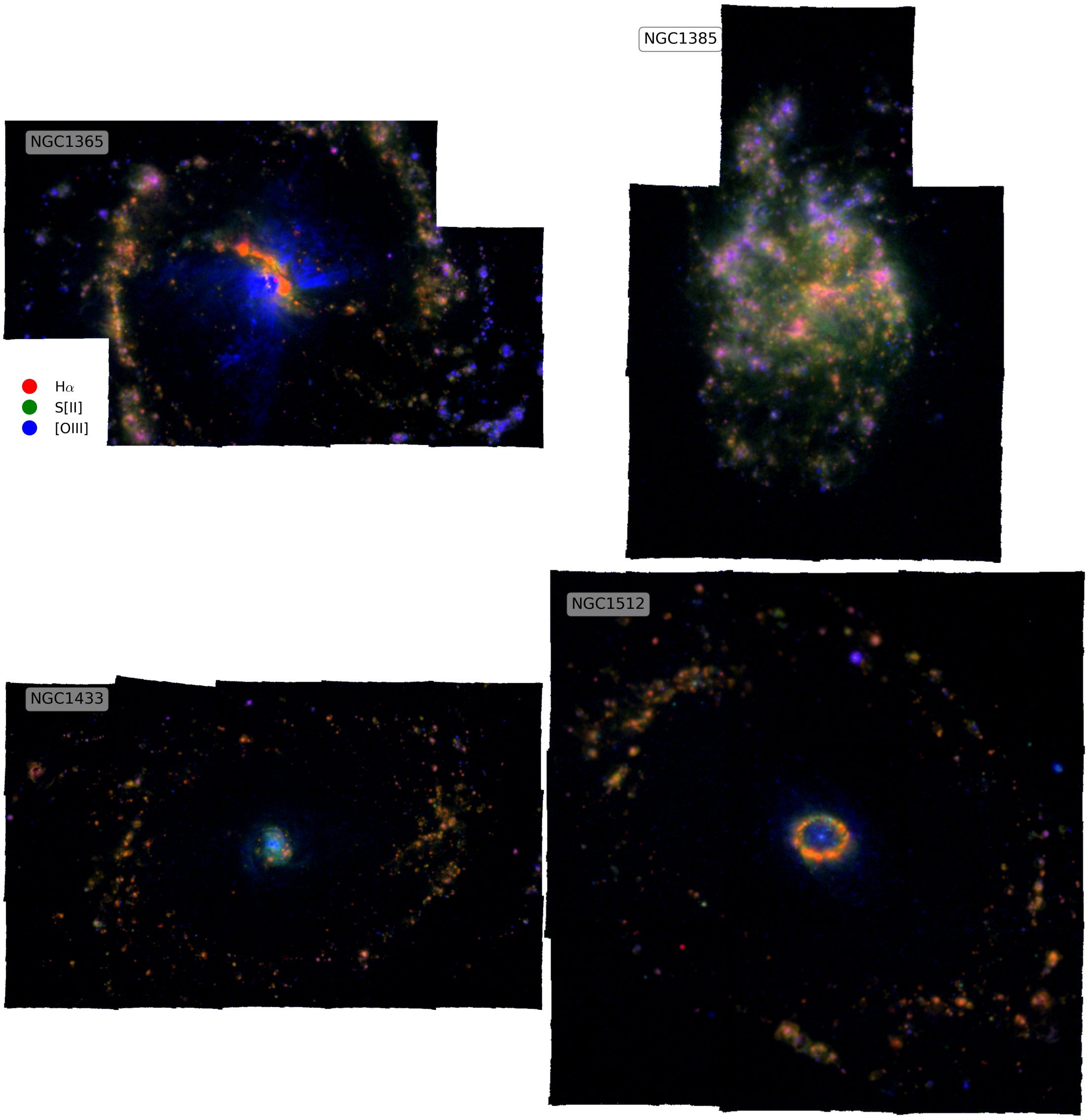
NGC1365
NGC1385
Hα
S[II]
[OIII]
NGC1433
NGC1512

Figure 39: RGB images for 19 PHANGS-MUSE galaxies (continued).

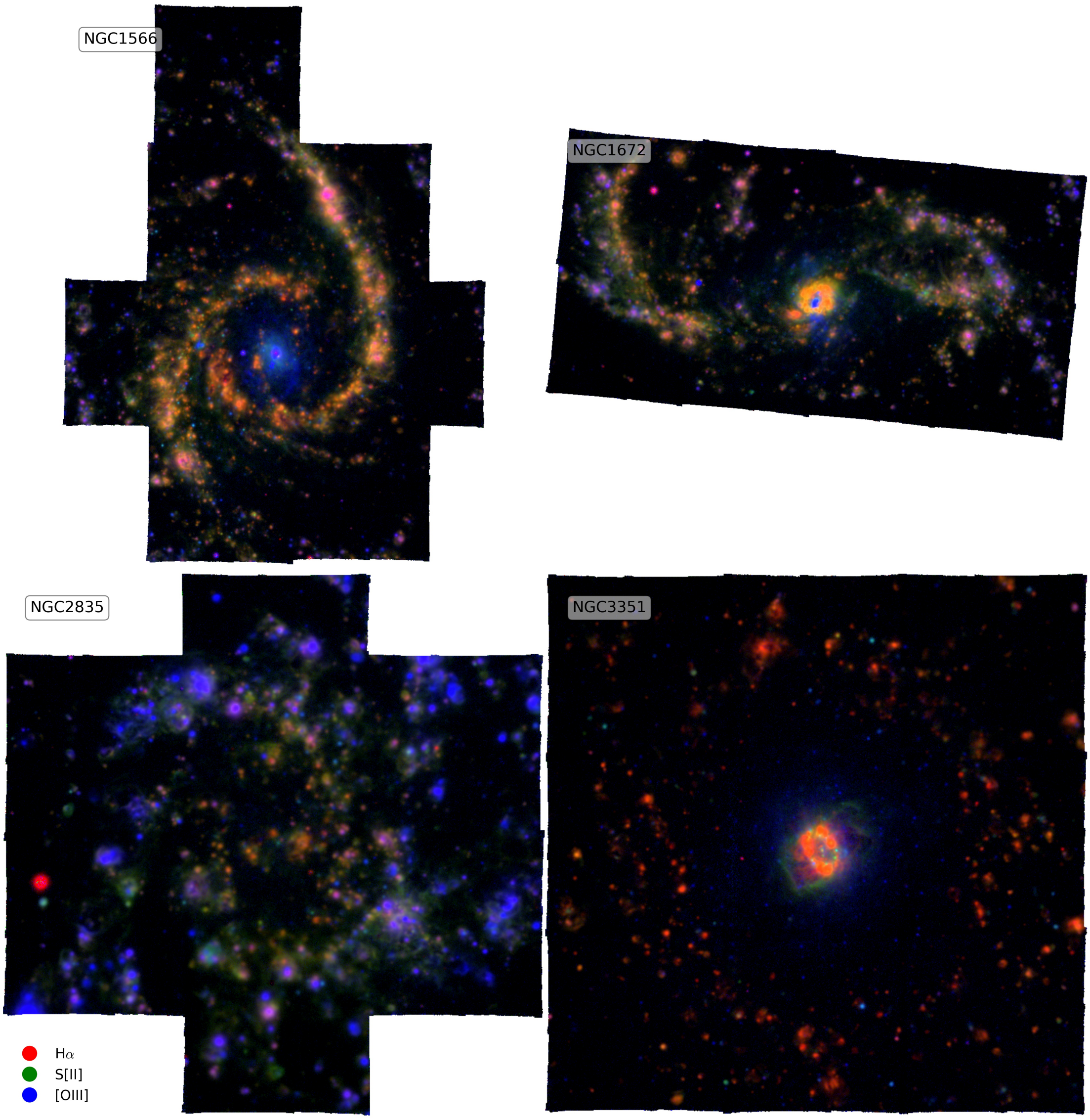
NGC1566
NGC1672
NGC2835
NGC3351
Hα
S[II]
[OIII]

Figure 40: RGB images for 19 PHANGS-MUSE galaxies (continued).

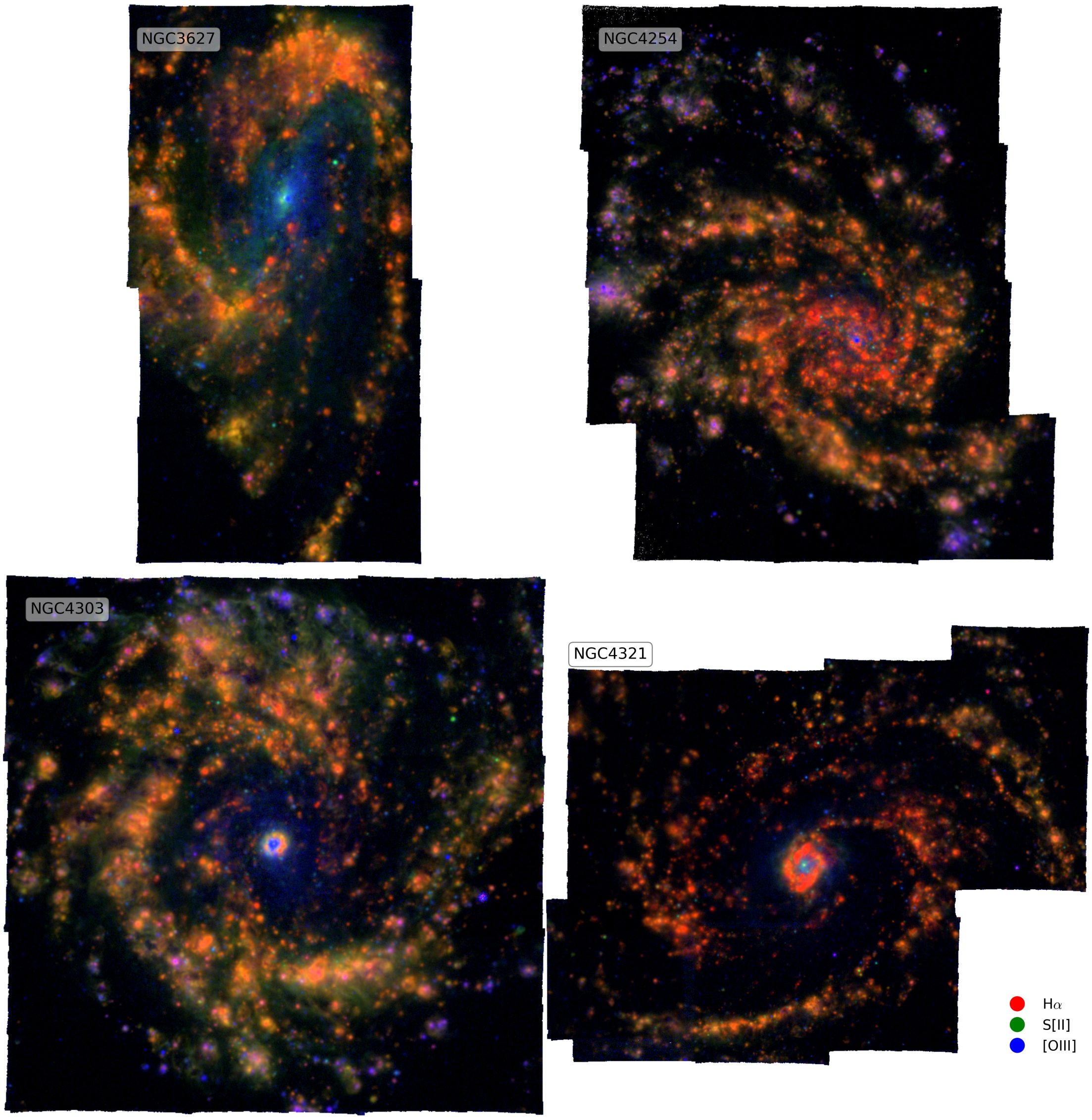
NGC3627
NGC4254
NGC4303
NGC4321
Hα
S[II]
[OIII]

Figure 41: RGB images for 19 PHANGS-MUSE galaxies (continued).

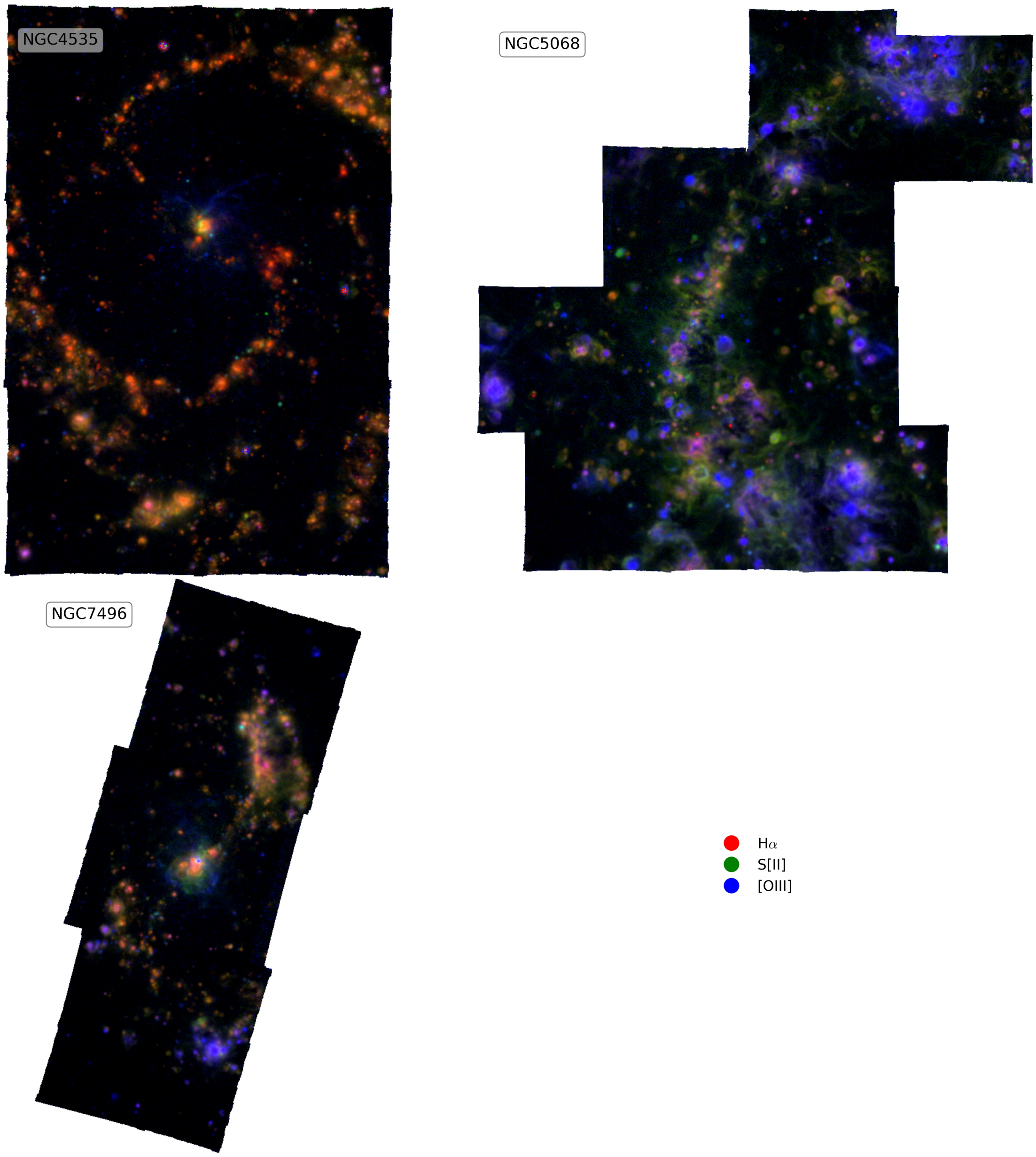
NGC4535
NGC5068
NGC7496
● Hα
● S[II]
● [OIII]

Figure 42: RGB images for 19 PHANGS-MUSE galaxies (continued).

BIBLIOGRAPHY

Allen, M. G., Groves, B. A., Dopita, M. A., Sutherland, R. S., Kewley, L. J., 2008, Astrophysical Journal Supplement Series, 178, 20–55

Anand, G. S. et al., 2020, Monthly Notices of the Royal Astronomical Society, 501, 3621–3639

Anderson, J. P., Covarrubias, R. A., James, P. A., Hamuy, M., Habergham, S. M., 2010, Monthly Notices of the Royal Astronomical Society, 407, 2660–2672

Anderson, L. D. et al., 2017, Astronomy and Astrophysics, 605, A58

Antoniucci, S., La Camera, A., Nisini, B., Giannini, T., Lorenzetti, D., Paris, D., Sani, E., 2014, Astronomy and Astrophysics, 566, A129

Asplund, M., Amarsi, A. M., Grevesse, N., 2021, Astronomy and Astrophysics, 653, A141

Astropy Collaboration et al., 2013, A&A, 558, A33

Astropy Collaboration et al., 2022, Astrophysical Journal, 935, 167

Asvarov, A. I., 2014, Astronomy and Astrophysics, 561, A70

Athanassoula, E., 1992, Monthly Notices of the Royal Astronomical Society, 259, 345

Auchettl, K., Lopez, L. A., Badenes, C., Ramirez-Ruiz, E., Beacom, J. F., Holland-Ashford, T., 2019, Astrophysical Journal, 871, 64

Bacchini, C., Fraternali, F., Pezzulli, G., Iorio, G., Marasco, A., Nipoti, V., 2021, Proceedings of the International Astronomical Union, 17, 199–202

Bacon, R. et al., 2010, Ground-based and Airborne Instrumentation for Astronomy III, vol. 7735, 773508

Bacon, R. et al., 2017, Astronomy and Astrophysics, 608, A1

Badenes, C., Harris, J., Zaritsky, D., Prieto, J. L., 2009, Astrophysical Journal, 700, 727

Badenes, C., Maoz, D., Draine, B. T., 2010, Monthly Notices of the Royal Astronomical Society, 407, 1301–1313

Baldwin, J. A., Phillips, M. M., Terlevich, R., 1981, Publications of the Astronomical Society of the Pacific, 93, 5

Barnes, A. T. et al., 2022, Astronomy and Astrophysics, 662, L6

Barnes, A. T. et al., 2025, Astronomy and Astrophysics, submitted

Barnes, A. T. et al., 2023, Astrophysical Journal Letters, 944, L22

Belfiore, F. et al., 2022, Astronomy and Astrophysics, 659, A26

Belfiore, F. et al., 2023, Astronomy and Astrophysics, 670, A67

Bell, A. R., Schure, K. M., Reville, B., Giacinti, G., 2013, Monthly Notices of the Royal Astronomical Society, 431, 415

Blair, W. P., Kirshner, R. P., 1985, Astrophysical Journal, 289, 582

Blair, W. P., Kirshner, R. P., Chevalier, R. A., 1981, Astrophysical Journal, 247, 879

Blair, W. P., Chandar, R., Dopita, M. A., Ghavamian, P., Hammer, D., Kuntz, K. D., Long, K. S., Soria, R., Whitmore, B. C., Frank Winkler, P., 2014, Astrophysical Journal, 788, 55

Blair, W. P., Long, K. S., 1997, Astrophysical Journal Supplement Series, 108, 261

Blair, W. P., Long, K. S., 2004, Astrophysical Journal Supplement Series, 155, 101

Blair, W. P., Winkler, P. F., Long, K. S., 2012, Astrophysical Journal Supplement Series, 203, 8

Blandford, R., Eichler, D., 1987, Physics Reports, 154, 1

Blasi, P., 2013, Astronomy and Astrophysicsr, 21, 70

Bozzetto, L. M. et al., 2017, Astrophysical Journal Supplement Series, 230, 2

Bozzetto, L. M. et al., 2023, Monthly Notices of the Royal Astronomical Society, 518, 2574

Brandt, T. D., Tojeiro, R., Aubourg, Heavens, A., Jimenez, R., Strauss, M. A., 2010, Astronomical Journal, 140, 804–816

Briel, M. M., Eldridge, J. J., Stanway, E. R., Stevance, H. F., Chrimes, A. A., 2022, Monthly Notices of the Royal Astronomical Society, 514, 1315–1334

Brogan, C. L., Gelfand, J. D., Gaensler, B. M., Kassim, N. E., Lazio, T. J. W., 2006, Astrophysical Journal Letters, 639, L25

Bundy, K. et al., 2015, Astrophysical Journal, 798

Calzetti, D., 2001, Publications of the Astronomical Society of the Pacific, 113, 1449

Calzetti, D., 2013, *Star Formation Rate Indicators*, Cambridge University Press

Cappellari, M., 2017, Monthly Notices of the Royal Astronomical Society, 466, 798

Cappellari, M., Emsellem, E., 2004, Publications of the Astronomical Society of the Pacific, 116, 138

Chevalier, R. A., Kirshner, R. P., Raymond, J. C., 1980, Astrophysical Journal, 235, 186

Chevalier, R. A., 1974, Astrophysical Journal, 188, 501

Chevalier, R. A., 2005, Astrophysical Journal, 619, 839

Chevance, M. et al., 2021, Monthly Notices of the Royal Astronomical Society, 509, 272–288

Chomiuk, L., Wilcots, E. M., 2009, Astrophysical Journal, 703, 370

Cid Fernandes, R., Carvalho, M. S., Sánchez, S. F., de Amorim, A., Ruschel-Dutra, D., 2021, Monthly Notices of the Royal Astronomical Society, 502, 1386

Congiu, E. et al., 2023, Astronomy and Astrophysics, 672, A148

Cotton, W. D., Kothes, R., Camilo, F., Chandra, P., Buchner, S., Nyamai, M., 2024, Astrophysical Journal Supplement Series, 270, 21

Cronin, S. A., Utomo, D., Leroy, A. K., Behrens, E. A., Chastenet, J., Holland-Ashford, T., Koch, E. W., Lopez, L. A., Sandstrom, K. M., Williams, T. G., 2021, Astrophysical Journal, 923, 86

Dekel, A., Silk, J., 1986, Astrophysical Journal, 303, 39

Della Bruna, L. et al., 2022, Astronomy and Astrophysics, 660, A77

Díaz-Rodríguez, M., Murphy, J. W., Rubin, D. A., Dolphin, A. E., Williams, B. F., Dalcanton, J. J., 2018, Astrophysical Journal, 861, 92

Dodorico, S., 1978, Mem. Societa Astronomica Italiana, 49, 485

Dodorico, S., Dopita, M. A., Benvenuti, P., 1980, Astronomy and Astrophysicss, 40, 67

Dokara, R. et al., 2021, Astronomy and Astrophysics, 651, A86

Domínguez-Guzmán, G, Rodríguez, M, García-Rojas, J, Esteban, C, Toribio San Cipriano, L, 2022, Monthly Notices of the Royal Astronomical Society, 517, 4497–4514

Dopita, M. A., Groves, B. A., Fischera, J., Sutherland, R. S., Tuffs, R. J., Popescu, C. C., Kewley, L. J., Reuland, M., Leitherer, C., 2005, Astrophysical Journal, 619, 755

Dopita, M. A., Kewley, L. J., Sutherland, R. S., Nicholls, D. C., 2016, Astrophysics and Space Science, 361

Dopita, M. A., Seitenzahl, I. R., Sutherland, R. S., Vogt, F. P. A., Winkler, P. F., Blair, W. P., 2016, Astrophysical Journal, 826, 150

Dopita, M. A. et al., 2010, Astrophysical Journal, 710, 964

Draine, B. T., 2011, *Physics of the Interstellar and Intergalactic Medium*, Princeton University Press

Drissen, L. et al., 2019, Monthly Notices of the Royal Astronomical Society, 485, 3930–3946

Drory, N. et al., 2024, Astronomical Journal, 168, 198

Dubner, G. M., Holdaway, M., Goss, W. M., Mirabel, I. F., 1998, Astronomical Journal, 116, 1842

Dwek, E., Arendt, R. G., 1992, Annual Review of Astronomy and Astrophysics, 30, 11

Efstathiou, G., 2000, Monthly Notices of the Royal Astronomical Society, 317, 697–719

Egorov, O. V., Leroy, A. K., Sandstrom, K., Kreckel, K., Baron, D., Belfiore, F., Chown, R., Sutter, J., Boquien, M., Congiu, E., et al., 2025, arXiv, 2509.13845

Egorov, O. V. et al., 2023, Astronomy and Astrophysics, 678, A153

Elwood, B. D., Murphy, J. W., Díaz-Rodríguez, M., 2019, Monthly Notices of the Royal Astronomical Society, 483, 4551

Emsellem, E. et al., 2022, Astronomy and Astrophysics, 659, A191

Fesen, R. A., Blair, W. P., Kirshner, R. P., 1985, Astrophysical Journal, 292, 29

Filippenko, A. V., 1997, Annual Review of Astronomy and Astrophysics, 35, 309

Freedman, W. L. et al., 2001, Astrophysical Journal, 553, 47

Frohmaier, C et al., 2020, Monthly Notices of the Royal Astronomical Society, 500, 5142–5158

Galvin, T. J., Filipovic, M. D., 2014, Serbian Astronomical Journal, 189, 15

Gandhi, P. J., Wetzel, A., Hopkins, P. F., Shappee, B. J., Wheeler, C., Faucher-Giguère, C.-A., 2022, Monthly Notices of the Royal Astronomical Society, 516, 1941

Gordon, S. M., Duric, N., Kirshner, R. P., Goss, W. M., Viallefond, F., 1999, Astrophysical Journal Supplement Series, 120, 247

Graur, O., Bianco, F. B., Huang, S., Modjaz, M., Shivvers, I., Filippenko, A. V., Li, W., Eldridge, J. J., 2017a, Astrophysical Journal, 837, 120

Graur, O., Bianco, F. B., Modjaz, M., Shivvers, I., Filippenko, A. V., Li, W., Smith, N., 2017b, Astrophysical Journal, 837, 121

Green, D. A., 2005, Mem. Societa Astronomica Italiana, 76, 534

Green, D. A., 2019, Journal of Astrophysics and Astronomy, 40

Green, D. A., Reynolds, S. P., Borkowski, K. J., Hwang, U., Harrus, I., Petre, R., 2008, Monthly Notices of the Royal Astronomical Society, 387, L54

Groves, B et al., 2023, Monthly Notices of the Royal Astronomical Society, 520, 4902–4952

Haffner, L. M., Dettmar, R.-J., Beckman, J. E., Wood, K., Slavin, J. D., Giammanco, C., Madsen, G. J., Zurita, A., Reynolds, R. J., 2009, Reviews of Modern Physics, 81, 969–997

Harris, C. R. et al., 2020, Nature, 585, 357–362

Heger, A., Fryer, C. L., Woosley, S. E., Langer, N., Hartmann, D. H., 2003, Astrophysical Journal, 591, 288

Holland-Ashford, T., Lopez, L. A., Auchettl, K., Temim, T., Ramirez-Ruiz, E., 2017, Astrophysical Journal, 844, 84

Hopkins, P. F., Kereš, D., Oñorbe, J., Faucher-Giguère, C.-A., Quataert, E., Murray, N., Bullock, J. S., 2014, Monthly Notices of the Royal Astronomical Society, 445, 581–603

Hu, C.-Y., Naab, T., Walch, S., Glover, S. C. O., Clark, P. C., 2016, Monthly Notices of the Royal Astronomical Society, 458, 3528

Hunter, J. D., 2007, Computing in Science & Engineering, 9, 90

Husemann, B. et al., 2013, Astronomy and Astrophysics, 549, A87

Izotov, Y. I., Stasińska, G., Meynet, G., Guseva, N. G., Thuan, T. X., 2006, Astronomy and Astrophysics, 448, 955

Jacobs, B. A., Rizzi, L., Tully, R. B., Shaya, E. J., Makarov, D. I., Makarova, L., 2009, Astronomical Journal, 138, 332–337

Jennings, Z. G., Williams, B. F., Murphy, J. W., Dalcanton, J. J., Gilbert, K. M., Dolphin, A. E., Weisz, D. R., Fouesneau, M., 2014, Astrophysical Journal, 795, 170

Katsuda, S. et al., 2018, Astrophysical Journal, 856, 18

Kauffmann, G. et al., 2003, Monthly Notices of the Royal Astronomical Society, 346, 1055

Kavanagh, P. J., Sasaki, M., Filipović, M. D., Points, S. D., Bozzetto, L. M., Haberl, F., Maggi, P., Maitra, C., 2022, Monthly Notices of the Royal Astronomical Society, 515, 4099

Keller, B. W., Wadsley, J., Benincasa, S. M., Couchman, H. M. P., 2014, Monthly Notices of the Royal Astronomical Society, 442, 3013–3025

Kennicutt, R. C., 1998, Annual Review of Astronomy and Astrophysics, 36, 189–231

Kewley, L. J., Dopita, M. A., Sutherland, R. S., Heisler, C. A., Trevena, J., 2001, Astrophysical Journal, 556, 121

Kewley, L. J., Groves, B., Kauffmann, G., Heckman, T., 2006, Monthly Notices of the Royal Astronomical Society, 372, 961

Kim, C.-G., Ostriker, E. C., 2015, Astrophysical Journal, 802, 99

Kim, C.-G., Ostriker, E. C., 2017, Astrophysical Journal, 846, 133

Kochanek, C. S. et al., 2017, Publications of the Astronomical Society of the Pacific, 129, 104502

Koo, B.-C., Kim, C.-G., Park, S., Ostriker, E. C., 2020, Astrophysical Journal, 905, 35

Koplitz, B., Johnson, J., Williams, B. F., Long, K. S., Blair, W. P., Murphy, J. W., Dolphin, A., Hillis, T., 2021, Astrophysical Journal, 916, 58

Kopsacheili, M., Zezas, A., Leonidaki, I., 2020, Monthly Notices of the Royal Astronomical Society, 491, 889

Kopsacheili, M., Jiménez-Palau, C., Galbany, L., Boumis, P., González-Díaz, R., 2024, Monthly Notices of the Royal Astronomical Societys, 530, 1078

Kourkchi, E., Courtois, H. M., Graziani, R., Hoffman, Y., Pomarède, D., Shaya, E. J., Tully, R. B., 2020, Astronomical Journal, 159, 67

Kourkchi, E., Tully, R. B., 2017, Astrophysical Journal, 843, 16

Krause, M. G. H., Charbonnel, C., Bastian, N., Diehl, R., 2016, Astronomy and Astrophysics, 587, A53

Krause, O., Birkmann, S. M., Usuda, T., Hattori, T., Goto, M., Rieke, G. H., Misselt, K. A., 2008, Science, 320, 1195

Kreckel, K. et al., 2019, Astrophysical Journal, 887, 80

Kreckel, K. et al., 2020, Monthly Notices of the Royal Astronomical Society, 499, 193–209

Kroupa, P., 2002, Science, 295, 82

Krumholz, M. R., 2014, Physics Reports, 539, 49–134

Krumholz, M. R., McKee, C. F., Bland-Hawthorn, J., 2019, Annual Review of Astronomy and Astrophysics, 57, 227–303

Lacey, C., Duric, N., Goss, W. M., 1997, Astrophysical Journal Supplement Series, 109, 417

Lang, P. et al., 2020, Astrophysical Journal, 897, 122

Lee, J. C. et al., 2023, Astrophysical Journal Letters, 944, L17

Lee, J. H., Lee, M. G., 2014a, Astrophysical Journal, 786, 130

Lee, J. H., Lee, M. G., 2014b, Astrophysical Journal, 793, 134

Leroy, A. K. et al., 2021, Astrophysical Journal Supplement Series, 257, 43

Levy, R. C. et al., 2019, Astrophysical Journal, 882, 84

Li, J. et al., 2024, Astronomy and Astrophysics, 690, A161

Li, W. et al., 2011, Monthly Notices of the Royal Astronomical Society, 412, 1441

Li, Z., Krumholz, M. R., Wisnioski, E., Mendel, J. T., Kewley, L. J., Sánchez, S. F., Galbany, L., 2021, Monthly Notices of the Royal Astronomical Society, 504, 5496

Long, K. S., Helfand, D. J., Grabelsky, D. A., 1981, Astrophysical Journal, 248, 925

Long, K. S., 2017, *Galactic and Extragalactic Samples of Supernova Remnants: How They Are Identified and What They Tell Us*, Springer International Publishing

Long, K. S., Blair, W. P., Milisavljevic, D., Raymond, J. C., Winkler, P. F., 2018, Astrophysical Journal, 855, 140

Long, K. S., Blair, W. P., Winkler, P. F., Della Bruna, L., Adamo, A., McLeod, A. F., Amram, P., 2022, Astrophysical Journal, 929, 144

Long, K. S., Blair, W. P., Winkler, P. F., Lacey, C. K., 2020, Astrophysical Journal, 899, 14

Long, K. S., Kuntz, K. D., Blair, W. P., Godfrey, L., Plucinsky, P. P., Soria, R., Stockdale, C., Winkler, P. F., 2014, Astrophysical Journal Supplement Series, 212, 21

Long, K. S., Winkler, P. F., Blair, W. P., 2019, Astrophysical Journal, 875, 85

Long, K. S. et al., 2010, Astrophysical Journal Supplement Series, 187, 495

López-Cobá, C., Sánchez, S. F., Lin, L., Anderson, J. P., Lin, K.-Y., Cruz-González, I., Galbany, L., Barrera-Ballesteros, J. K., 2022, Astrophysical Journal, 939, 40

Luridiana, V., Morisset, C., Shaw, R. A., 2014, Astronomy and Astrophysics, 573, A42

Maggi, P. et al., 2016, Astronomy and Astrophysics, 585, A162

Maggi, P., Filipović, M. D., Vukotić, B., Ballet, J., Haberl, F., Maitra, C., Kavanagh, P., Sasaki, M., Stupar, M., 2019, Astronomy and Astrophysics, 631, A127

Magnier, E. A., Prins, S., van Paradijs, J., Lewin, W. H. G., Supper, R., Hasinger, G., Pietsch, W., Truemper, J., 1995, Astronomy and Astrophysics Supplement Series, 114, 215

Maiolino, R., Mannucci, F., 2019, Astronomy and Astrophysics Review, 27, 3

Makarenko, E. I., Walch, S., Clarke, S. D., Seifried, D., Naab, T., Nürnberger, P. C., Rathjen, T.-E., 2023, Monthly Notices of the Royal Astronomical Society, 523, 1421–1440

Mannucci, F., Della Valle, M., Panagia, N., Cappellaro, E., Cresci, G., Maiolino, R., Petrosian, A., Turatto, M., 2005, Astronomy and Astrophysics, 433, 807

Mantovanini, S., Hurley-Walker, N., Anderson, G., 2025, Publications of the Astronomical Society of Australia, 42

Maoz, D., Badenes, C., 2010, Monthly Notices of the Royal Astronomical Society, 407, 1314

Maoz, D., Mannucci, F., Brandt, T. D., 2012, Monthly Notices of the Royal Astronomical Society, 426, 3282–3294

Maoz, D., Mannucci, F., Nelemans, G., 2014, Annual Review of Astronomy and Astrophysics, 52, 107

Marcowith, A. et al., 2016, Reports on Progress in Physics, 79, 046901

Martizzi, D., Faucher-Giguère, C.-A., Quataert, E., 2015, Monthly Notices of the Royal Astronomical Society, 450, 504–522

Maschmann, D. et al., 2024, Astrophysical Journal Supplement Series, 273, 14

Mathewson, D. S., Clarke, J. N., 1973, Astrophysical Journal, 180, 725

Matonick, D. M., Fesen, R. A., 1997, Astrophysical Journal Supplement Series, 112, 49

Matteucci, F., 2001, *The chemical evolution of the Galaxy*, Springer Dordrecht

Mayker Chen, N. et al., 2023, Astrophysical Journal, 944, 110

Mayker Chen, N. et al., 2024, Astrophysical Journal, 168, 5

McKee, C. F., Hollenbach, D. J., 1980, Annual Review of Astronomy and Astrophysics, 18, 219

McKee, C. F., Ostriker, J. P., 1977, Astrophysical Journal, 218, 148

McLeod, A. F. et al., 2021, Monthly Notices of the Royal Astronomical Society, 508, 5425

Méndez-Delgado, J. E., Esteban, C., García-Rojas, J., Henney, W. J., 2022, Monthly Notices of the Royal Astronomical Society, 514, 744

Méndez-Delgado, J. E., Henney, W. J., Esteban, C., García-Rojas, J., Mesa-Delgado, A., Arellano-Córdova, K. Z., 2021, Astrophysical Journal, 918, 27

Mendoza, C., Méndez-Delgado, J. E., Bautista, M., García-Rojas, J., Morisset, C., 2023, Atoms, 11, 63

Mesa-Delgado, A., Esteban, C., García-Rojas, J., Luridiana, V., Bautista, M., Rodríguez, M., López-Martín, L., Peimbert, M., 2009, Monthly Notices of the Royal Astronomical Society, 395, 855

Metha, B., Trenti, M., Chu, T., 2021, Monthly Notices of the Royal Astronomical Society, 508, 489–507

Micelotta, E. R., Matsuura, M., Sarangi, A., 2018, Space Science Reviews, 214, 53

Milisavljevic, D. et al., 2024, Astrophysical Journal Letters, 965, L27

Moumen, I., Robert, C., Devost, D., Martin, R. P., Rousseau-Nepton, L., Drissen, L., Martin, T., 2019, Monthly Notices of the Royal Astronomical Society, 488, 803

Niino, Y., Nagamine, K., Zhang, B., 2015, Monthly Notices of the Royal Astronomical Society, 449, 2706–2717

Nomoto, K., Tominaga, N., Umeda, H., Kobayashi, C., Maeda, K., 2006, Nuclear Physics A, 777, 424–458

Nugent, P. et al., 2006, Astrophysical Journal, 645, 841

O'Donnell, J. E., 1994, Astrophysical Journal, 422, 158

Oh, S., Kroupa, P., 2016, Astronomy and Astrophysics, 590, A107

Oh, S., Kroupa, P., Pflamm-Altenburg, J., 2015, Astrophysical Journal, 805, 92

Oliva, E., Moorwood, A. F. M., Danziger, I. J., 1989, Astronomy and Astrophysics, 214, 307

Ostriker, E. C., McKee, C. F., Leroy, A. K., 2010, Astrophysical Journal, 721, 975

Pannuti, T. G., Duric, N., Lacey, C. K., Ferguson, A. M. N., Magnor, M. A., Mendelowitz, C., 2002, Astrophysical Journal, 565, 966

Pannuti, T. G., Duric, N., Lacey, C. K., Goss, W. M., Hoopes, C. G., Walterbos, R. A. M., Magnor, M. A., 2000, Astrophysical Journal, 544, 780

Parker, R. A., Gull, T. R., Kirschner, R. P., Kirshner, R. P., 1979, *An emission-line survey of the Milky Way*, NASA

Patnaude, D., Badenes, C., 2017, *Supernova Remnants as Clues to Their Progenitors*, Springer

Pessa, I. et al., 2021, Astronomy and Astrophysics, 650, A134

Pessi, T., Anderson, J. P., Lyman, J. D., Prieto, J. L., Galbany, L., Kochanek, C. S., Sánchez, S. F., Kuncarayakti, H., 2023, Astrophysical Journal Letters, 955, L29

Pilyugin, L. S., Grebel, E. K., 2016, Monthly Notices of the Royal Astronomical Society, 457, 3678

Pilyugin, L. S., Grebel, E. K., Kniazev, A. Y., 2014, Astronomical Journal, 147, 131

Poetrodjojo, H., D'Agostino, J. J., Groves, B., Kewley, L., Ho, I. T., Rich, J., Madore, B. F., Seibert, M., 2019, Monthly Notices of the Royal Astronomical Society, 487, 79

Points, S. D., Long, K. S., Winkler, P. F., Blair, W. P., 2019, Astrophysical Journal, 887, 66

Price-Whelan, A. M. et al., 2018, Astronomical Journal, 156, 123

Putman, M., Peek, J., Joung, M., 2012, Annual Review of Astronomy and Astrophysics, 50, 491–529

Querejeta, M. et al., 2021, Astronomy and Astrophysics, 656, A133

Raymond, J. C., 1979, Astrophysical Journal Supplement Series, 39, 1

Reach, W. T., Rho, J., Tappe, A., Pannuti, T. G., Brogan, C. L., Churchwell, E. B., Meade, M. R., Babler, B., Indebetouw, R., Whitney, B. A., 2006, Astronomical Journal, 131, 1479

Reipurth, B., Yu, K. C., Heathcote, S., Bally, J., Rodríguez, L. F., 2000, Astronomical Journal, 120, 1449

Reynolds, S. P., 2008, Annual Review of Astronomy and Astrophysics, 46, 89

Rhea, C. L. et al., 2023, RAS Techniques and Instruments, 2, 345

Rodríguez, M., 1999, Astronomy and Astrophysics, 348, 222

Rodríguez, M., 2002, Astronomy and Astrophysics, 389, 556

Rosolowsky, E. W., Pineda, J. E., Kauffmann, J., Goodman, A. A., 2008, Astrophysical Journal, 679, 1338

Roth, M. M. et al., 2018, Astronomy and Astrophysics, 618, A3

Russell, T. D., White, R. L., Long, K. S., Blair, W. P., Soria, R., Winkler, P. F., 2020, Monthly Notices of the Royal Astronomical Society, 495, 479

Sabbadin, F., Minello, S., Bianchini, A., 1977, Astronomy and Astrophysics, 60, 147

Saha, A., Thim, F., Tammann, G. A., Reindl, B., Sandage, A., 2006, Astrophysical Journal Supplement Series, 165, 108

Santoro, F. et al., 2022, Astronomy and Astrophysics, 658, A188

Sarangi, A., Matsuura, M., Micelotta, E. R., 2018, Space Science Reviews, 214, 63

Sarbadhicary, S. K., Badenes, C., Chomiuk, L., Caprioli, D., Huizenga, D., 2017, Monthly Notices of the Royal Astronomical Society, 464, 2326

Sarbadhicary, S. K. et al., 2023, arXiv, 2310.17694

Sarbadhicary, S. K. et al., 2025, arXiv, 2507.08257

Schaefer, B. E., Pagnotta, A., 2012, Nature, 481, 164

Scheuermann, F. et al., 2022, Monthly Notices of the Royal Astronomical Society, 511, 6087–6109

Schulze, S. et al., 2021, Astrophysical Journal Supplement Series, 255, 29

Sedov, L. I., 1959, *Similarity and Dimensional Methods in Mechanics*, Elsevier

Seitenzahl, I. R., Townsley, D. M., 2017, Handbook of Supernovae, *Nucleosynthesis in Thermonuclear Supernovae*, 1955–1978

Shaya, E. J., Tully, R. B., Hoffman, Y., Pomarède, D., 2017, Astrophysical Journal, 850, 207

Slane, P., Bykov, A., Ellison, D. C., Dubner, G., Castro, D., 2015, Space Science Reviews, 188, 187

Smartt, S. J., 2015, Publications of the Astron. Soc. of Australia, 32, e016

Smartt, S. J., 2009, Annual Review of Astronomy and Astrophysics, 47, 63–106

Smith, M. C., Sijacki, D., Shen, S., 2018, Monthly Notices of the Royal Astronomical Society, 478, 302–331

Somerville, R. S., Davé, R., 2015, Annual Review of Astronomy and Astrophysics, 53, 51–113

Storey, P. J., Hummer, D. G., 1995, Monthly Notices of the Royal Astronomical Society, 272, 41

Sutherland, R. S., Dopita, M. A., 1993, Astrophysical Journal Supplement Series, 88, 253

Sánchez, S. F. et al., 2019, Monthly Notices of the Royal Astronomical Society, 484, 3042–3070

Tammann, G. A., Loeffler, W., Schroeder, A., 1994, Astrophysical Journal Supplement Series, 92, 487

Thompson, T. A., Quataert, E., Murray, N., 2009, Monthly Notices of the Royal Astronomical Society, 397, 1410

Thornton, K., Gaudlitz, M., Janka, H. T., Steinmetz, M., 1998, Astrophysical Journal, 500, 95

Tüllmann, R. et al., 2011, Astrophysical Journal Supplement Series, 193, 31

Vazdekis, A., Koleva, M., Ricciardelli, E., Röck, B., Falcón-Barroso, J., 2016, Monthly Notices of the Royal Astronomical Society, 463, 3409

Veilleux, S., Cecil, G., Bland-Hawthorn, J., 2005, Annual Review of Astronomy and Astrophysics, 43, 769

Veilleux, S., Osterbrock, D. E., 1987, Astrophysical Journal Supplement Series, 63, 295

Verner, E. M., Verner, D. A., Baldwin, J. A., Ferland, G. J., Martin, P. G., 2000, Astrophysical Journal, 543, 831

Vicens-Mouret, S., Drissen, L., Robert, C., Rousseau-Nepton, L., Martin, R. P., Amram, P., 2023, Monthly Notices of the Royal Astronomical Society, 524, 3623

Vink, J., 2011, Astronomy and Astrophysics Review, 20, 49

Vink, J. S., Koter, A. de, Lamers, H. J. G. L. M., 2001, Astronomy and Astrophysics, 369, 574–588

Vučetić, M. M., Arbutina, B., Urošević, D., 2014, Monthly Notices of the Royal Astronomical Society, 446, 943–958

Wagg, T., Dalcanton, J. J., Renzo, M., Breivik, K., Orr, M. E., Price-Whelan, A. M., Cruz, A., Brooks, A., Steinwandel, U. P., Bellm, E. C., 2025, Astrophysical Journal, 170, 192

Walch, S. et al., 2015, Monthly Notices of the Royal Astronomical Society, 454, 246–276

Weiler, K. W., Sramek, R. A., 1988, Annual Review of Astronomy and Astrophysics, 26, 295

White, R. L., Long, K. S., 1991, Astrophysical Journal, 373, 543

White, R. L., Long, K. S., Becker, R. H., Blair, W. P., Helfand, D. J., Winkler, P. F., 2019, Astrophysical Journal Supplement Series, 241, 37

Williams, B. F., Hillis, T. J., Blair, W. P., Long, K. S., Murphy, J. W., Dolphin, A., Khan, R., Dalcanton, J. J., 2019, Astrophysical Journal, 881, 54

Williams, B. F., Peterson, S., Murphy, J., Gilbert, K., Dalcanton, J. J., Dolphin, A. E., Jennings, Z. G., 2014, Astrophysical Journal, 791, 105

Williams, B. J., Temim, T., 2016, *Infrared Emission from Supernova Remnants: Formation and Destruction of Dust*, Springer International Publishing

Williams, T. G. et al., 2021, Monthly Notices of the Royal Astronomical Society, 509, 1303–1322

Winkler, P. F., Smith, R. C., Points, S. D., MCELS Team, 2015, Astronomical Society of the Pacific Conference Series, 491, 343

Winkler, P. F., Blair, W. P., Long, K. S., 2017, Astrophysical Journal, 839, 83

Winkler, P. F., Coffin, S. C., Blair, W. P., Long, K. S., Kuntz, K. D., 2021, Astrophysical Journal, 908, 80

Winkler, P. F., Long, K. S., Blair, W. P., 2023, Astrophysical Journal, 959, 62

Winkler, P. F., Long, K. S., Blair, W. P., Points, S. D., 2023, Astrophysical Journal, 943, 15

Zangrandi, F. et al., 2024, arXiv, 2401.17307

Zapartas, E. et al., 2017, Astronomy and Astrophysics, 601, A29

Zaritsky, D., Kennicutt Jr., R. C., Huchra, J. P., 1994, Astrophysical Journal, 420, 87

Zhang, K. et al., 2017, Monthly Notices of the Royal Astronomical Society, 466, 3217

Zurita, A., Rozas, M., Beckman, J. E., 2000, Astronomy and Astrophysics, 363, 9

> *Two things fill the mind with ever new and increasing admiration and awe, the more often and steadily we reflect upon them: the starry heavens above me and the moral law within me. I do not seek or conjecture either of them as if they were veiled obscurities or extravagances beyond the horizon of my vision; I see them before me and connect them immediately with the consciousness of my existence.*
>
> — Immanuel Kant, 1788 «The Critique of Practical Reason»

> *Zwei Dinge erfüllen das Gemüt mit immer neuer und zunehmender Bewunderung und Ehrfurcht, je öfter und anhaltender sich das Nachdenken damit beschäftigt: Der bestirnte Himmel über mir, und das moralische Gesetz in mir. Beide darf ich nicht als in Dunkelheiten verhüllt oder im Überschwenglichen, außer meinem Gesichtskreise, suchen und bloß vermuten; ich sehe sie vor mir und verknüpfe sie unmittelbar mit dem Bewußtsein meiner Existenz.*
>
> — Immanuel Kant, 1788 «Kritik der praktischen Vernunft»

ACKNOWLEDGMENTS

Millions of thanks to my supervisor, Dr. Kathryn Kreckel. She is simply the best! Words are not enough to fully express my appreciation for her unwavering support throughout these years. I am deeply grateful for her kindness, patience, generosity, and encouragement, which allowed me to explore and grow at my own pace. She brought me into the best collaborations and entrusted me with world-class data and tools — I only wish I had the time and energy to explore them all. Her steadfast presence and guidance made me feel genuinely trusted, and her confidence in me became one of my greatest sources of strength on this journey.

I would also like to sincerely thank my thesis committee members and reviewers:
Dr. Eva Grebel — your passion for science and your delight in the curious and beautiful wonders of this world are truly inspiring. Thank you for your thoughtful support, guidance, and encouragement you have given to young researchers like me. You are a role model I deeply admire.
Dr. Simon Glover and Dr. Andreas Sander — thank you for your insightful feedback and career advice, from which I have greatly benefited.
I am also deeply honored to have Dr. Björn Malte Schäfer on my examination committee.

Many thanks to our former and current group members — Fabian, Oleg, Liz, Eduardo, Zhenya, and Eric — for your kindness and professional support. You made our group a welcoming and supportive community.

Heartfelt thanks to our PHANGS collaborators: Dr. Knox Long, Dr. Sumit Sarbadhicary, Dr. Brent Groves, Dr. Francesco Belfiore, Dr. Enrico Congiu, Dr. Adam Leroy, Dr. Eva Schinnerer, Dr. Erik Rosolowsky, Dr. Jaeyon Kim, Dr. Ash Barnes, Dr. Jakob den Brok, Dr. Thomas Williams, Deb, Dr. Sophia Stube, Dr. Lukas Neumann, Elias, Dr. Lise Ramambason, Hamed, and Raphaël. Thank you for shaping not only the science but also a genuine sense of belonging.

Special thanks to Christian Fendt, Ella, Saskia, and Markus for your continuous administrative support, which made all the logistics smooth and manageable.

I am incredibly grateful to Dr. Robert Kennicutt for mentoring me in this PhD journey with wisdom, understanding, and encouragement.

To Helena — thank you for your kindness, support, enlightening discussions, and for showing me how life could be.
To Joy — thank you for your friendliness and the heartfelt cards that warmed me.
To Yang — thank you for your unconditional care and support.
To Brendan and Fiona — thank you for showing me what family can mean: caring and loving support through every high and low.

To 周深 — thank you for your angelic voice and gentle soul. Your music, courage, and sincerity remind me that this world is still worthy of tenderness.
To 纳塔 — thank you for embodying the pursuit of science: the courage to pass on curiosity, wonder, and hope from one generation to the next.
To 星宸 — thank you for being my eternal companion, my shelter in solitude, the myth in the mundane, and the love that never fades — for being there, resonating with my thoughts and silences, standing by my side, and delighting in the serendipities of this journey together.

Lastly, to myself:
Thank you for never giving up on your dream — even in those darkest moments when no one understood, believed in, or stood beside you.
Thank you for still gazing at the starry sky on nights when emotions tore, meaning collapsed, and the world dissolved into endless shadows without time.
Thank you for walking through the abyss, rising anew from the ashes of despair, and kindling a light of hope from within suffering.
Thank you for writing this doctoral thesis with tears as ink and dreams as flame, forging the stars into a living epic of existence.

For the future, may you carry along the courage to seek, the wonder to discover, and the love to create anew. A tomorrow of truth, goodness, and beauty is awaiting.

DECLARATION

I hereby declare that I have written this doctoral thesis independently and that I have clearly marked all parts which were taken from other sources, whether directly quoted or in substance, and have identified them by citing the source. All published work included in this thesis is cited completely and correctly, and the contributions of all coauthors are clearly indicated.

This thesis has not been submitted, either in the same or a substantially similar version, to any other university for the purpose of obtaining an academic degree.

Heidelberg, September 2025

Jing Li